

**Modeling ~~Wind and wave effects on the~~ dispersal of the Pearl  
River-derived sediment over the Shelf**

Guang Zhang<sup>1,2,3</sup>, Suan Hu<sup>1,2,3</sup>, Xiaolong Yu<sup>1,2,3</sup>, Heng Zhang<sup>1,2,3</sup>, Wenping Gong<sup>1,2,3\*</sup>

<sup>1</sup> School of Marine Sciences, Sun Yat-sen University, [Zhuhai, 519082, China](#) ~~Guangzhou, China, 510275~~

<sup>2</sup> Guangdong Provincial Key Laboratory of Marine Resources and Coastal Engineering, [Zhuhai, 519082,](#)

[China](#) ~~Guangzhou 510275, China~~

<sup>3</sup> Pearl River Estuary Marine Ecosystem Research Station, Ministry of Education, Zhuhai 519082, China

Corresponding author: Wenping Gong ([gongwp@mail.sysu.edu.cn](mailto:gongwp@mail.sysu.edu.cn))

## Abstract

This study employs the Coupled Wave–Ocean–Sediment Transport Model to quantitatively assess the seasonal suspension, transport, and annual fate of Pearl River-derived sediment on the northern South China Sea (SCS) continental shelf. After careful model validation, several sensitivity model simulations were conducted. Results reveal pronounced seasonal variations in sediment dynamics driven by the monsoonal climate. During the wet summer, calm conditions favor initial deposition via the river plume, whereas stronger winter winds and waves resuspend and transport sediments into the Beibu Gulf. Spatially, 66.45% of the total sediment load is retained within the estuarine vicinity, 9.2% is deposited on the eastern continental shelf, and 8.86% and 10.3% accumulate in the Beibu Gulf and the area south of Hainan Island, respectively. Sensitivity experiments highlight the distinct roles of tidal forces, wave action, and background circulation in sediment transport and deposition. Tidal dynamics govern sediment behavior in the Pearl River Estuary, where neglecting tidal effects underestimates bottom shear stress, overestimates sediment deposition, and underestimates distal retention. Wave action dominates sediment resuspension at the river mouth, nearshore regions, particularly during high-energy winter periods. Excluding waves leads to overestimated deposition in these areas and underestimates accumulation in the Beibu Gulf. Background circulation is most influential in summer, with a strong northeastward current transporting sediments to the eastern shelf. Without this current, only 0.84% of sediments reach the eastern shelf, leading to an overestimation of distal deposition. The sediment model results are also highly

sensitive to sediment parameterization and initial conditions. Neglecting seasonal variations in critical shear stress for erosion overestimates winter resuspension and erosion east of the Leizhou Peninsula, increasing distal retention. Higher settling velocities lower SSC while overestimating proximal retention and underestimating distal retention. Additionally, initial sediment conditions significantly impact sediment transport, with the retention of pre-existing sediment leading to further offshore transport. However, the model is relatively insensitive to the initial bed grain size distribution. This study provides a comprehensive assessment of Pearl River-derived sediment dynamics and highlights key physical mechanisms governing sediment fate in the northern SCS.

~~The transport processes of suspended sediment from river sources to ocean sinks are vital for the global material cycle. This study quantitatively examines the effects of wind and wave dynamics on riverine sediment transport over a continental shelf throughout a typical year, utilizing the Coupled Ocean Atmosphere Wave Sediment Transport (COAWST) model. After meticulous calibration, the model effectively replicates various fundamental marine environmental processes. Key findings reveal that over a typical year, approximately 62% of riverine sediment is retained near the estuary, with sediments primarily transported southwestward and deposited in Beibu Gulf. Significant seasonality in sediment transport was revealed. During the wet summer, calm winds and waves lead to initial sediment deposition near the estuary via the river plume. In contrast, the dry winter sees stronger winds and waves resuspending and transporting these sediments. Analyses demonstrate that combined~~

~~wind and wave action reduces proximal riverine sediment deposition levels to 83% of those under No wind or wave conditions, resulting in a fivefold increase in westward alongshore sediment flux. Additionally, intensified cross shore gradients of water level and density boost westward geostrophic flow and thermal wind shear, facilitating sediment transport to distant regions. This study offers valuable insights into the intricate interplay between winds, waves, and riverine sediment dynamics on continental shelves.~~

## **Keywords**

Riverine sediment transport; ~~Wind and wave~~; Sediment ~~dynamics~~[retention](#); Numerical modeling; Pearl River Estuary

## **1. Introduction**

The transport process of suspended sediment from river source to ocean sink is an important link in the global material cycle ([Kuehl et al., 2016](#); [Liu et al., 2016](#); [Cao et al., 2019](#)). Much of the riverine sediment is trapped on the shallow shoals in estuaries, while the rest is transported by river plume out of the estuary ([Meade, 1969](#); [Burchard et al., 2018](#); [Zhang et al., 2019](#)). The riverine sediment carried by the river plume has a significant impact on the water quality, ecology, and geomorphology of the estuaries and continental shelves ([Wright and Coleman, 1973](#); [Turner and Millward, 2002](#)).—

~~The extent, transport pathway, and depocenter of riverine sediment on the continental shelf initially depend on the supply of sediments by the river plume ([Wright and Nittrouer, 1995](#)). Then, the ultimate dispersal and fate of the plume and riverine sediment are influenced by coastal currents, tides, winds, and waves ([Dyer,](#)~~



~~1997;Geyer et al., 2004;Harris et al., 2008;Bever et al., 2009;Rong et al., 2014;Horner Devine et al., 2015). Winds and waves play a crucial role in shaping river plumes (Rong et al., 2014;Lai et al., 2016;Chi and Rong, 2023), estuarine and coastal circulation (Gan et al., 2009;Li and Li, 2011;Gan et al., 2013), and then influence the sediment resuspension, transport, and deposition in coastal and marine environments (Geyer et al., 2004;Harris et al., 2008;Bever et al., 2009).~~

The transport and deposition of riverine sediments from river source to estuarine, coastal, and shelf environments are governed by various physical processes, including tidal forces, wave action, and shelf circulation dynamics (Gao and Collins, 2014). Tides play a critical role in estuarine sediment transport dynamics, as spring tides typically produce higher bed shear stress, enhanced sediment resuspension, and greater offshore sediment transport flux compared to neap tides (Bever and MacWilliams, 2013;Zhang et al., 2019). In nearshore regions, wave-induced bed shear stress is often an order of magnitude higher than that generated by currents (Xue et al., 2012). Furthermore, wave-driven sediment resuspension frequently exceeds, and is often several times greater than, the peak levels achieved by current-induced resuspension (Sanford, 1994;Brand et al., 2010). In shelf regions, shelf circulations significantly influence sediment transport, with the magnitude of along-shelf transport substantially exceeding the cross-shelf component in most locations (Nittrouer and Wright, 1994;Gao and Collins, 2014).

Furthermore, sediment properties, including settling velocity (Xia et al., 2004;Chen et al., 2010;Cheng et al., 2013), critical shear stress for erosion (Dong et

al., 2020), and bed grain size distribution (Xue et al., 2012; Bever and MacWilliams, 2013), significantly influence sediment transport dynamics and deposition/resuspension processes. Settling velocity can influence the location of sediment depocenters, with higher settling velocities leading to more proximal entrapment and vice versa (Ralston and Geyer, 2017). Similarly, critical shear stress for erosion can affect the resuspension of deposited sediment, with higher critical shear stress resulting in less resuspension and more deposition especially during neap tides and weak wind wave periods (Dong et al., 2020; Choi et al., 2023).

A comprehensive understanding of sediment transport and deposition from river source to ocean sink requires the integrated consideration of both physical forcing factors and inherent sediment characteristics. Here, we present the transport and deposition of ~~use China's~~ Pearl River-derived sediments on the continental shelf ~~Estuary (PRE)~~ as a case study. The Pearl River, ranking as China's second-largest river in terms of freshwater ~~river~~-discharge (Hu et al., 2011), forms the Pearl River Estuary (PRE) in its lower reaches (Figures 1 and S1). Its freshwater and sediment discharge are primarily delivered through eight major outlets (Figure S1b; Wu et al., 2016; Zhang et al., 2019), forming distinct plumes that extend across the northern South China Sea (SCS) shelf. The present average annual (2001-2022) freshwater and riverine sediment loads are  $2.74 \times 10^{11} \text{ m}^3$  and  $2.84 \times 10^7$  tons, as reported by the Ministry of Water Resources of the People's Republic of China (<http://www.mwr.gov.cn/sj/#tjgb>). The distribution of these inputs shows significant seasonal variability: approximately 80% of the freshwater and 95% of the sediment

load are transported during the wet summer season (April to September), while the remaining portion is discharged during the dry winter season (Xia et al., 2004).

The northern SCS, shaped by the East Asian Monsoon, displays marked seasonal contrasts, featuring winter monsoon winds averaging 7-10 m s<sup>-1</sup> and summer winds typically below 6 m s<sup>-1</sup> (Su, 2004;Ou et al., 2009). This seasonal shift drives coastal currents: northeastward in summer and southwestward in winter (Gan et al., 2009;Gan et al., 2013). Beyond the coastal zone, the consistent SCS Warm Current (SCSWC) flows northeastward along the shelf break and inner continental slope toward the Taiwan Strait, originating near Hainan Island and persisting year-round, even during the winter northeast monsoon, across a remarkable distance of 600-700 km to the southern tip of the Taiwan Strait (Su, 2004;Yang et al., 2008).

The PRE is situated in the central part of the northern South China Sea boundary, positioned between the Taiwan Banks and Hainan Island. The PRE has a micro-tidal and mixed semi-diurnal regime, with daily inequality in the range and in the time between the high and low tides (Mao et al., 2004). The neap and spring tides alternately influence the water elevation downstream of the estuary, with tidal ranges varying from approximately 0.7 m during neap tides to over 2 m during spring tides (Chen et al., 2016;Gong et al., 2018b). The PRE and the nearby shelf exhibit strong seasonal variation in water column stability and are highly stratified during the wet summer season, while the PRE becomes partially mixed or vertically well-mixed during the dry winter season (Dong et al., 2004). Offshore of the PRE region, wave conditions display distinct seasonal patterns: the waves are mild during summer, and

become stronger during winter, marked by larger southeasterly waves (Gong et al., 2018a;Gong et al., 2018b;Zhang et al., 2021).

Previous studies have focused on sediment transport within the PRE. Most Pearl River-derived sediments are deposited within the estuary, and neglecting tidal effects can lead to overestimating deposition rates while underestimating offshore sediment flux (Hu et al., 2011). The depositional dynamics of sediments from different PRE outlets are shaped by outlet location, topography, and tidal conditions, with neap tides favoring sediment accumulation on shoals and spring tides driving erosion and enhancing offshore sediment transport (Zhang et al., 2019). Waves further intensify both lateral trapping within the PRE and offshore sediment transport (Liu and Cai, 2019;Zhang et al., 2021).

However, numerical studies on the transport of Pearl River-derived sediments across the continental shelf remain scarce, even amidst the widespread adoption of computer modeling approaches. Previous research on the distribution of these sediments has primarily relied on analyses of seismic profiles, gravity cores, and laboratory-based radiometric dating of sediment samples (Ge et al., 2014;Liu et al., 2014;Cao et al., 2019;Lin et al., 2020;Chen et al., 2023).~~Previous studies have investigated the total suspended sediment concentration (SSC) and its transport under impacts of typhoon or winter storm-induced wave current effect in the PRE (Liu and Cai, 2019;Zhang et al., 2021;Yang et al., 2022).~~ Outside the PRE, gravity core and seismic survey data were used to examine the Holocene sedimentary processes, revealing two distinct mud depo-centers: one an eastward proximal depo-center

165 ~~extending southeastward and one a southwestward~~ distal mud belt ~~and southwestward,~~  
166 ~~respectively~~ (Ge et al., 2014; Liu et al., 2014; Chen et al., 2023). However, seismic and  
167 drilling data cannot confirm that the Pearl River sediment can be transported to the  
168 Beibu Gulf (Ge et al., 2014). Due to the lack of sufficient gravity core samples and  
169 seismic data, it is difficult to quantitatively attribute the sediment in the Beibu Gulf to  
170 the Pearl River-derived sediment (Cao et al., 2019). Afterward, Lin et al. (2020) used  
171 the  $^{226}\text{Ra}$ — $^{238}\text{U}$  and  $^{232}\text{Th}$ — $^{238}\text{U}$  endmembers model based on measurements of  
172 radionuclides in the surface sediment samples. They found that approximately 15% of  
173 the surface sediment in the nearshore area of the Beibu Gulf originates from the PRE  
174 region. However, their studies only address the proportion of PRE sediment in the  
175 surface sediment of the Beibu Gulf, without directly indicating the seasonal transport  
176 pathways, flux, and annual deposition mechanisms of sediment from the Pearl River.  
177 ~~Therefore, the specific processes of sediment transport and deposition and the fate of~~  
178 ~~the Pearl River derived sediment on the continental shelf have not been adequately~~  
179 ~~addressed. Although several studies have delved into the Pearl River derived sediment~~  
180 ~~suspension, transport, and budgets within the PRE (Xia et al., 2004; Hu et al.,~~  
181 ~~2011; Zhang et al., 2019), research on riverine sediment dispersal beyond the estuary~~  
182 ~~remains relatively limited.~~

183 A gap persists in understanding how physical processes (such as tides, waves, and  
184 ambient circulations) and sediment characteristics (such as critical shear stress for  
185 erosion, settling velocity) and sediment initial conditions~~winds and waves~~ influence  
186 the seasonal suspension, transport, and annual deposition of Pearl River-derived

sediment on the shelf, ~~including how it enters the Beibu Gulf.~~ In this study, we utilize numerical modeling, complemented by extensive collection of field observations and seabed grain size distribution data for model calibration and validation—a highly effective approach for exploring mechanisms and testing hypotheses derived from limited observational datasets. This study focused on the processes of Pearl River-derived sediment suspension, transport, and deposition ~~driven by winds and waves~~ over the continental shelf. Several specific questions addressed in this paper include:

(1) What are the seasonal dispersal and annual deposition patterns of the Pearl River-derived sediment-~~suspension, transport, and deposition~~ over the continental shelf?

(2) How do ~~the winds and waves~~ physical processes, sediment characteristics and sediment initial conditions influence ~~affect the continental shelf hydrodynamics; subsequently influencing~~ the dispersal ~~transport and fate~~ of the Pearl River-derived sediment?

## **2. Study Region**

~~The South China Sea, situated in the southern part of mainland China, is the largest marginal sea in the northwest Pacific (Figure 1a), covering approximately 3.5 million km<sup>2</sup>, featuring a wide continental shelf in the northern part and adjoining the PRE (Liu et al., 2014; Zhong et al., 2017). The dynamic forcing of the sea surface exhibits significant seasonal variations: during summer, the prevailing southwest~~

monsoon, with an average wind speed of  $6 \text{ m s}^{-1}$ , dominates the entire sea area, whereas the northeast monsoon, with an average wind speed of  $9 \text{ m s}^{-1}$ , prevails during winter (Su, 2004; Liu et al., 2014). Northeast-oriented shelf flow prevails in summer, contrasting with southwestward flow in winter, accompanied by distinct upwelling in summer and downwelling in winter, reflecting clear patterns of cross-shelf water exchange dynamics (Gan et al., 2009; Gan et al., 2013).

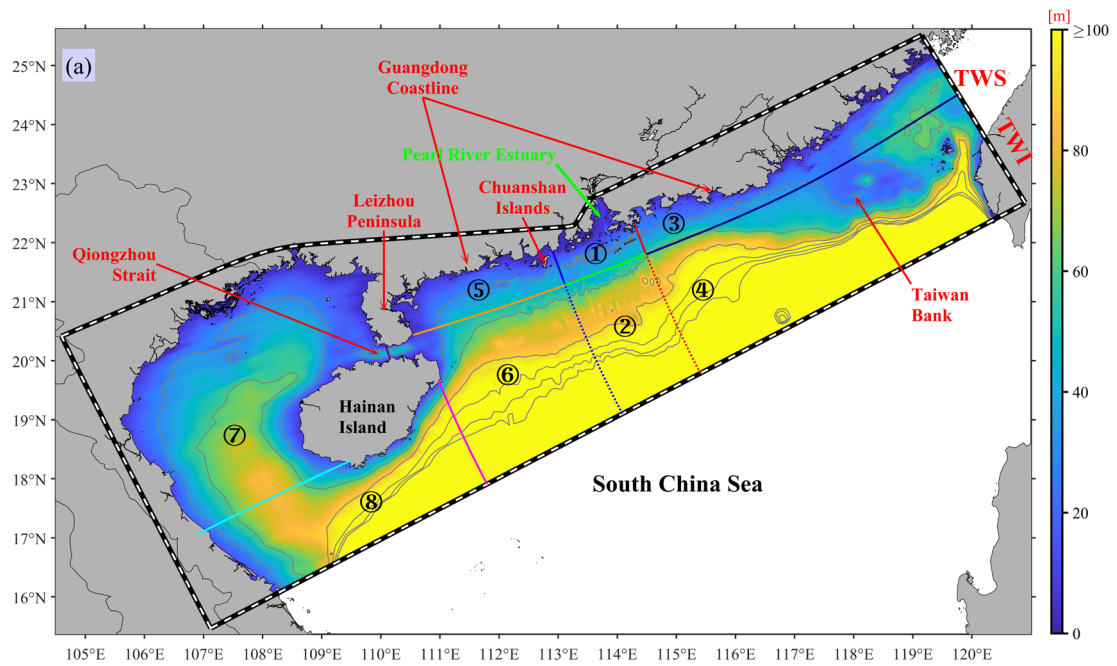


**Figure 1.** Bathymetry (shading) and isobath contours of the study area, with the ROMS/SWAN model grid domain outlined by black-to-white dashed lines. Circled numbers ①-⑧ denote the eight regions: Proximal, Southern, Eastern, Southeastern, Western, Southwestern, Beibu Gulf, and Distal regions, as defined by transects and detailed in Section 4.2. The abbreviations TWI and TWS mean Taiwan Island and Taiwan Strait, respectively. The gray contours represent 30-180 m isobaths at 30 m intervals, a consistent feature maintained in all subsequent figures that include these

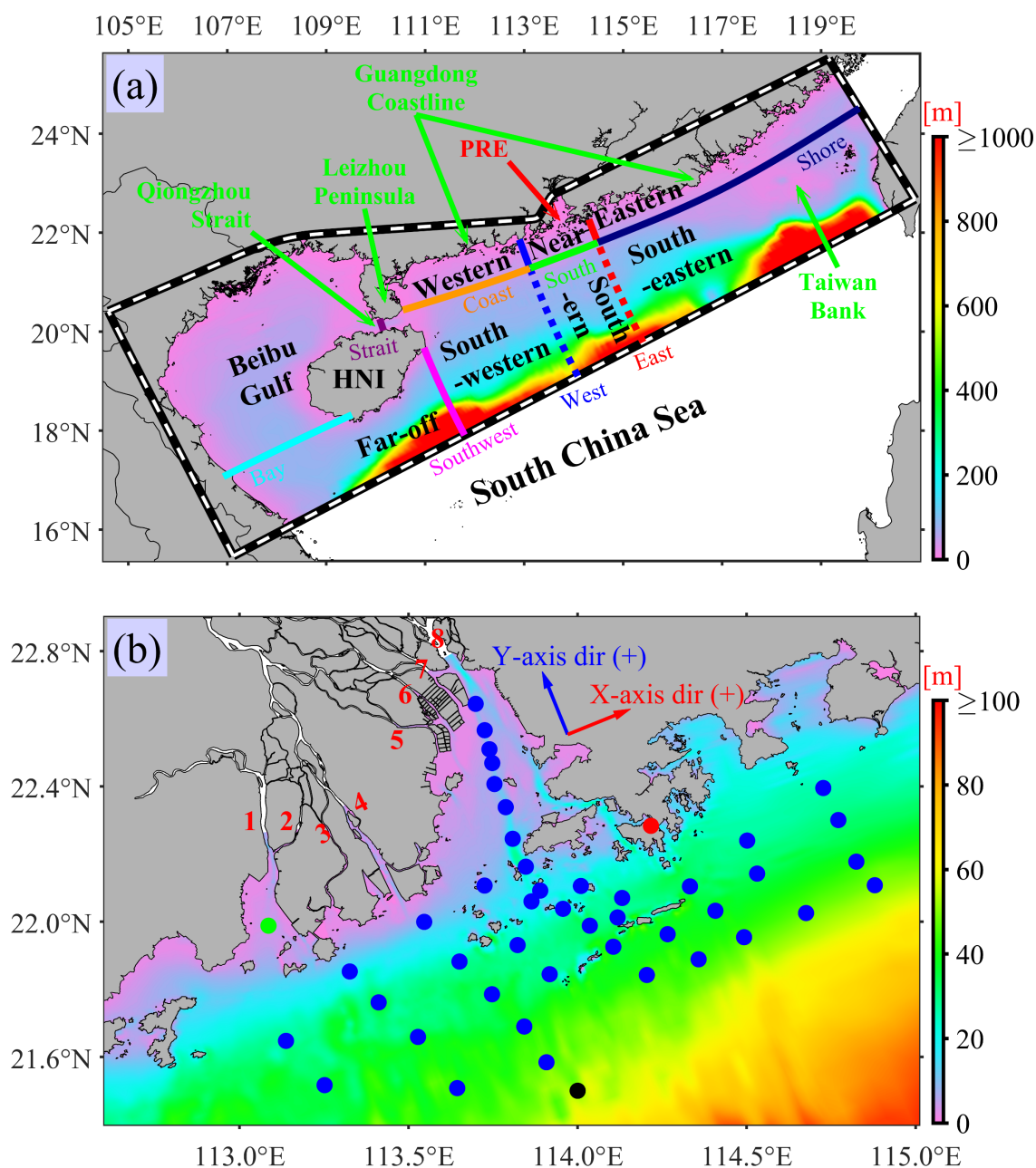


**Figure 1.** (a) Bathymetry (shading) and transects (same color as their respective names) on the model grid. (b) zoom in on the Pearl River Estuary (PRE) and nearby waters. The abbreviations HNI and PRE, mean Hainan Island and PRE, respectively. The observation stations, represented by red, green, blue, and black dots respectively, denote the Quarry Bay water level station, the 113-hour fixed onboard S1 station in



the PRE, 43 CTD stations during the voyage campaign, and wave station W. The red numbers 1–8 represent the eight outlets of the PRE, where Pearl River freshwater and sediment (the fourth and fifth sizes of sediments in Table 1 below) are discharged into the PRE. The X-axis and Y-axis represent the alongshore and cross-shore directions, respectively, as described in the main text and subsequent figures. The arrows indicate the positive direction of each axis.

The Pearl River experiences significant seasonal variations in freshwater and sediment discharges, with approximately 80% of freshwater and 95% of sediment load being discharged during the wet summer season from April to September (Xia et al., 2004). The Pearl River forms the complex PRE downstream, with freshwater and riverine sediments typically entering the PRE from eight outlets (Figure 1b; Wu et al., 2016; Zhang et al., 2019).

The PRE has a micro-tidal and mixed semi-diurnal regime, with daily inequality in the range and in the time between the high and low tides (Mao et al., 2004). The neap and spring tides alternately influence the water elevation downstream of the estuary, with tidal ranges varying from approximately 0.7 m during neap tides to approximately 2 m during spring tides (Chen et al., 2016; Gong et al., 2018b). The PRE and the nearby shelf exhibit strong seasonal variation and are highly stratified during the wet summer season, while the PRE becomes partially mixed or vertically well-mixed during the dry winter season (Dong et al., 2004).

## **3.2. Methods**

### **3.2.1 Model coupling**

This study employed the Coupled Ocean Atmosphere Wave Sediment Transport (COAWST, version 3.4) modeling system ([Warner et al., 2005](#); [Warner et al., 2008](#); [Warner et al., 2010](#)), which includes a Model Coupling Toolkit (MCT) to facilitate data exchange among different modules ([Jacob et al., 2005](#); [Larson et al., 2005](#)). The COAWST system consists of several modeling components, mainly comprises a hydrodynamic module (Regional Ocean Modeling System; ROMS) ([Shchepetkin and McWilliams, 2005](#); [Haidvogel et al., 2008](#)), an atmospheric module (Advanced Research Weather Research and Forecasting; WRF) ([Skamarock et al., 2005](#)), a wave module (Simulating Waves Nearshore; SWAN) ([Booij et al., 1999](#)), and a sediment transport module (Community Sediment Transport Modeling System; CSTM) ([Warner et al., 2008](#)).

In this study, we established a coupling between ROMS, SWAN, and CSTM. The model grid covers the northern continental shelf of the South China Sea, including the PRE (Figure 1). The regional model was configured with  $170 \times 482$  horizontal grid cells, with horizontal resolution varying from approximately 0.1 km near the PRE to about 10 km at outer open boundaries ([Hu et al., 2024](#)). The model grid bathymetry data was obtained from ~~the Global Earth Bathymetry Data Set (GEBCO) and~~ nautical charts compiled by the China Maritime Safety Administration and the General Bathymetric Chart of the Oceans (GEBCO) (Weatherall et al., 2015). The vertical grid used a Sigma coordinate system with 20 layers and a stretching transformation for higher resolution near the surface and bottom, with stretching parameters of  $\theta_s=3.0$  and  $\theta_b=3.0$ , respectively ([Song and Haidvogel, 1994](#)). For model validations, please

refer to the [Supplementary Material](#) ~~Supplement file~~ (Supplement Figures S1-S3S10).

## **32.2 ROMS model setup**

For the ROMS models, we utilized the Generic Length Scale turbulence closure scheme ([Warner et al., 2005](#)) for vertical turbulence parameterization. The method of [Smagorinsky \(1963\)](#) was employed to calculate the horizontal eddy viscosity and diffusivity. The Flather and Chapman boundary conditions were applied to barotropic current and water elevation at open boundaries, respectively ([Flather, 1976](#); [Chapman, 1985](#)). Meanwhile, the open-boundary conditions for temperature, salinity, and sediment concentration were imposed by radiation methods ([Orlanski, 1976](#); [Raymond and Kuo, 1984](#)). Surface forcing (including wind, net shortwave radiation, air temperature, atmospheric pressure, specific/relative humidity, and rain, etc.) data were sourced from the Climate Forecast System Reanalysis of the National Centers for Environmental Prediction ([NCEP](#)) ([Saha et al., 2014](#)), with a temporal resolution of 1 h and a spatial resolution of  $0.3^\circ \times 0.3^\circ$ . Water level and current open-boundary conditions comprised two components: tidal and subtidal. The tidal component was obtained from the Oregon State University Tidal Prediction Software database ([Egbert and Erofeeva, 2002](#)), while the subtidal component was interpolated from the HYbrid Coordinate Ocean Model (HYCOM) outputs ([Chassignet et al., 2007](#)).

## **32.3 Wave model setup**

The SWAN model was executed and coupled to the same grid as the ROMS model ([Warner et al., 2010](#)). It was driven by surface atmospheric forces, real-time water level, and current fields from the ROMS and boundary reanalysis data. Wave

boundary conditions were specified using nonstationary wave parameters from outputs of the [NOAA WAVEWATCH III global ocean wave model solutions \(Tolman et al., 2016\)](#). Information ~~was~~ exchanged ~~between the ROMS and SWAN models~~ ~~occurred~~ at 15-minute intervals to introduce wave-current interaction (WCI) [between the ROMS and SWAN models \(McWilliams et al., 2004; Kumar et al., 2012\)](#). This exchange included ~~significant wave height (Hsig)~~, surface peak wave period, mean wave direction and length, wave energy dissipation, and the percentage of breaking waves from SWAN to ROMS, as well as water level and current from ROMS to SWAN.

[Additionally, the wave-current bottom boundary module based on Madsen \(1994\), incorporated into COAWST, was activated to simulate the wave-current bottom boundary layer. The vortex force module of wave forces was also activated to compute the wave-induced momentum flux, utilizing the method proposed by McWilliams et al. \(2004\) and implemented in COAWST by Kumar et al. \(2012\). The bottom friction was computed based on a logarithmic velocity profile \(Warner et al., 2008\).](#)

#### **3.2.4 Specifications of riverine input and sediment model**

The freshwater discharge [for the Pearl River](#) was specified at the northern boundary using daily measured data [from the Pearl River Water Resources Commission](#), while downstream precipitation [within the Pearl River Basin](#) was neglected. The full simulation model was initialized on the first day of January 2016 using temperature, salinity, and current fields interpolated from the HYCOM model,

and it concluded on March 31, 2018. More than one year of hydrodynamic and sediment spin-up is sufficient to achieve appropriate seabed sediment particle size distribution, as well as stable circulation and thermohaline fields. This study primarily analyzes the last 12 months, specifically from April 1, 2017, to March 31, 2018. This year is selected because the freshwater discharge and sediment load of the Pearl River closely approximate the average values of the past two decades, with a runoff of  $3.35 \times 10^{11} \text{ m}^3$  and a sediment load of  $3.45 \times 10^7$  tons, closely resembling the averages from 2001 to 2022.

Since the daily riverine sediment loads were unavailable, we modified the following previous research results on sediment rating curves ([Zhang et al., 2012](#)) to suit for our study, as expressed by

$$y = 0.00002263x^{1.792} \quad (1)$$

where  $y$  is the Pearl River-derived suspended sediment concentration ( $\text{mg L}^{-1}$ ),  $x$  is the Pearl River freshwater discharge rate ( $\text{m}^3 \text{ s}^{-1}$ ). Based on this relationship, the total amount of Pearl River sediment input over our 12-months study period (Fig. 3b) was 34.52 million tons, aligning closely with the annual load reported in 2017 by the Pearl River Water Resources Commission. ~~the~~ The riverine sediment input, derived ~~calculated~~ from the river discharge, was allocated across ~~specified at~~ the eight outlets along ~~located on~~ the north boundary (Figure S1b) based on the distribution approach of Hu et al. (2011), between April 1, 2017, and March 31, 2018.

The subsequent step involves establishing the proportion of seabed sediment particle size components. Sediments are typically categorized into three grain-size

classes: clay (0-4  $\mu\text{m}$ ), silt (4-63  $\mu\text{m}$ ), and sand (63-2000  $\mu\text{m}$ ), as outlined by [Shepard \(1954\)](#). Data on sediment particle size composition for the northern continental shelf of the South China Sea and the PRE area were acquired through multiple voyage observations ([Zhang et al., 2013](#); [Zhang et al., 2019](#)). Furthermore, publicly available data from published literature were compiled ([Gao et al., 2007](#); [Kirby et al., 2008](#); [Gao et al., 2010](#); [Huang et al., 2013](#); [Liu et al., 2014](#); [Wang et al., 2014](#); [Wang et al., 2015](#); [Wang et al., 2016](#); [Ge et al., 2017](#); [Lu et al., 2017](#); [Zhong et al., 2017](#); [Yang et al., 2018](#); [Ge et al., 2019](#)). Finally, component distribution data for different particle size classes of seabed sediment were obtained from a total of 1981 measured stations (Figure 2a-c).

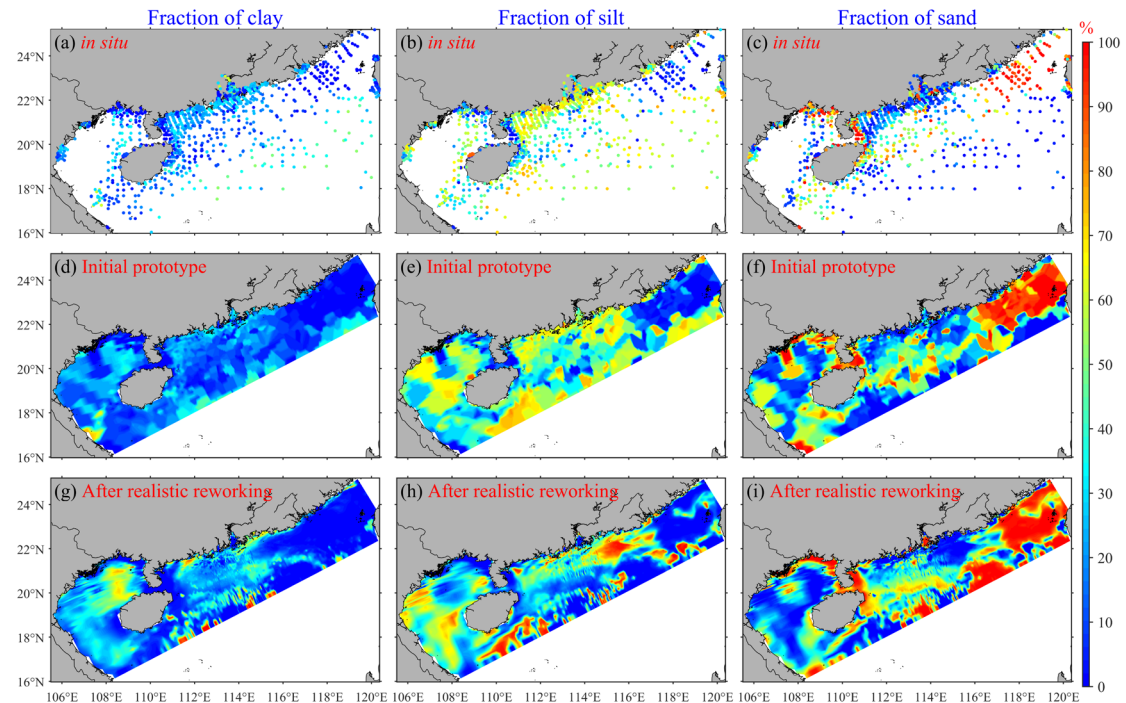


**Figure 2.** Row 1 presents the spatial distribution patterns of seabed sediment fractions derived from 1981 sampling sites, while Row 2 demonstrates the initial spatial

distribution prototype of seabed sediment fractions developed based on the observational data presented in Row 1. Row 3 shows the spatial distribution patterns of seabed sediment fractions following the completion of spin-up phase in the Control run case on April 1st, 2017, with Columns 1, 2, and 3 representing the fractions of clay, silt, and sand, respectively.

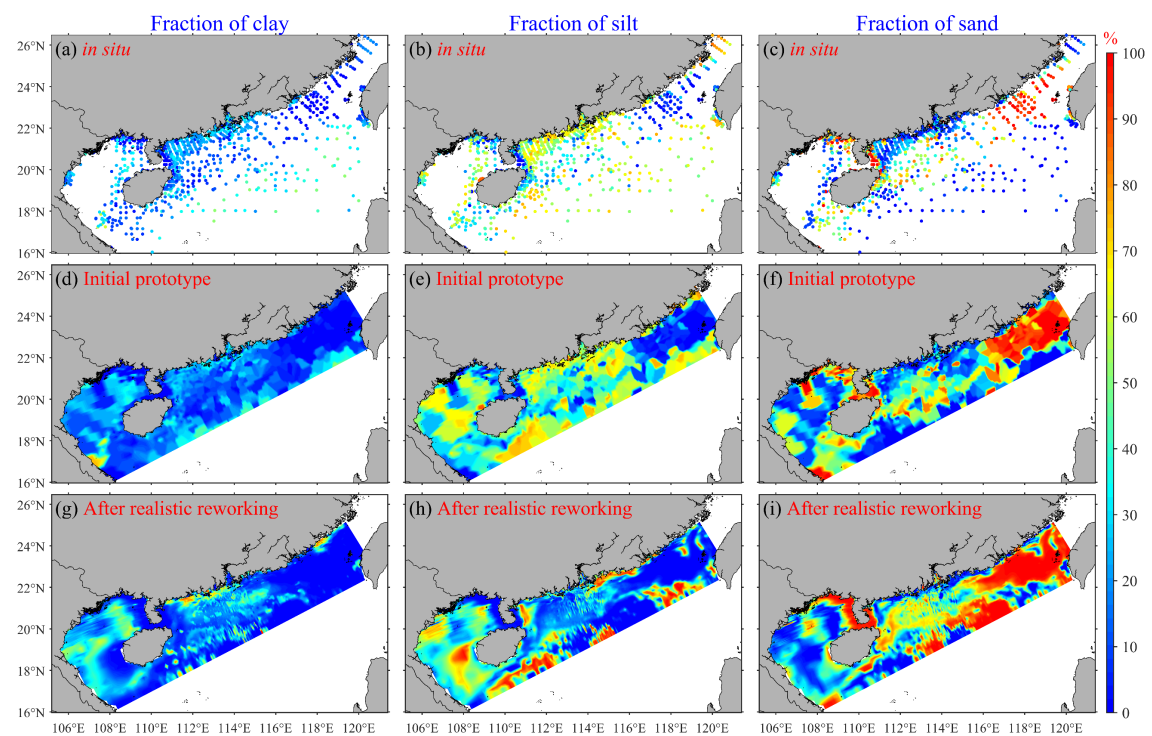


**Figure 2.** Row 1 illustrates the seabed spatial fractions observed across 1981 sites, while Row 2 exhibits the initial prototype of seabed spatial fractions distributions based on the observed data in Row 1. Row 3 showcases seabed spatial fractions distributions resulting from the model simulation on April 1st, 2017, with columns 1, 2, and 3 representing the fractions of clay, silt, and sand, respectively.

As illustrated in Figure 2a-c, the measured stations exhibit a widespread

distribution, offering comprehensive coverage of the entire northern continental shelf of the South China Sea, including the PRE. Particularly dense distribution is observed in the PRE and the coastal areas of western Guangdong. These regions represent the primary scope of transport and deposition associated with the Pearl River-derived sediment. Hence, the stations utilized in this study well represent the distribution of bed sediment particle size components in these study areas. It is evident that among the stations in the offshore area of the northern continental shelf of the South China Sea, silt dominates, followed by clay, while sand with the largest particle size is the least abundant. This suggests a significant presence of terrestrial sediment or Pearl River sediment in the offshore area of the northern continental shelf of the South China Sea. It should be noted that the lack of in situ grain size distribution data in specific regions of the model domain, especially in the Beibu Gulf area, may lead to uncertainties in sediment transport predictions. We will address these limitations and quantify their potential errors in the discussion part of this study.

To derive the component proportions of the initial prototype field on the model grid, this study employed the Kriging method (Krige, 1951), widely recognized for spatially interpolating various types of observational data. The sediment distribution pattern obtained through interpolation (Figure 2d-f) closely resembles the original 1981 measured sediment particle size distribution patterns (Figure 2a-c), suggesting the suitability of this interpolation method for the study area.

The initial prototype field underwent a 15-month spin-up period (from January 1, 2016, to March 31, 2017), during which it was adjusted by realistic reworking,



incorporating realistic hydrodynamics ~~winds~~ in ROMS, ~~and~~ SWAN, and CSTM models. This adjustment allowed for the redistribution of seabed sediment fractions based on the modeled hydrodynamics. This method has been utilized in numerous previous studies, including those by Bever et al. (2009), van der Wegen et al. (2010), and Zhang et al. (2021). The realistic spin-up greatly reduced the irregularities and prepared a more suitable seabed sediment particle size distribution field for subsequent simulations than the initial prototype (Figures 2d-f vs. 2g-i).

During the ~~simulations following 15-month~~ spin-up and the subsequent 12-month formal model simulations, the CSTM utilized five sediment classes (Table 1), which represent a range of sediment sizes and characteristics, including three types of seabed sediments (clay, silt, and sand, corresponding to the first three categories of sediments in Table 1) and two types of ~~riverine suspended sediment from the~~ Pearl River derived sediments (the sum of the fourth and fifth categories ~~sizes~~ of sediments in Table 1, namely the riverine slow-settling single fine grains (Class 4) and high-settling flocs (Class 5) "Clay (river)" and "Silt (river)"). This approach allows for a better distinction between Pearl River sediment and seabed sediment, enabling separate analysis of the suspension, transport, and deposition of Pearl River-derived sediment (Harris et al., 2008; Zhang et al., 2019). To clarify, the initial setup of the formal model simulations excludes the retained riverine sediment (Class 4 and Class 5 in Table 1) from the model domain during the spin-up period. The riverine flocs correspond to the flocculated fractions of clay and silt, whereas the single fine grains represent the non-flocculated components within the Pearl River-derived sediments, following the

setting of Bever and MacWilliams (2013). Specifically, the fractions of the two types of Pearl River-derived sediments were set at 40% and 60%, respectively, following Zhang et al. (2019) and Zhang et al. (2021). The parameters for all five sediment classes are summarized in Table 1. Sediment density, porosity, and erosion rate for all sediment classes were set to  $2650 \text{ kg m}^{-3}$ , 0.672 (Zhang et al., 2019; Zhang et al., 2021), and  $1 \times 10^{-4} \text{ kg m}^{-2} \text{ s}^{-1}$  (Ralston et al., 2012), respectively. The settling velocity ( $w_s$ ), critical shear stresses for erosion ( $\tau_{ce}$ ), and other parameters were set following previous studies or were based on model calibration (Ralston et al., 2012; Warner et al., 2017; Zhang et al., 2019; Dong et al., 2020; Zhang et al., 2021; Cao et al., 2025).

Our model configuration incorporates seasonal variations in  $\tau_{ce}$ , supported by multiple lines of evidence from field observations, laboratory experiments, and numerical analyses (Dong et al., 2020; Cao et al., 2025). Previous studies have established a distinct seasonal pattern in the PRE, with winter  $\tau_{ce}$  values significantly exceeding those in summer. Dong et al. (2020)'s laboratory experiments using the UMCES-Gust Erosion Microcosm System (U-GEMS) on 2017-winter sediment samples yielded a  $\tau_{ce}$  of 0.26 Pa, which effectively reproduced observed SSC in winter simulations. However, this value proved excessive for summer conditions, where a  $\tau_{ce}$  of 0.15 Pa provided better agreement with field observations in summer simulations, indicating a winter-to-summer  $\tau_{ce}$  ratio of 1.73. Recent 2020-summer in situ measurements by Cao et al. using a benthic quadrapod-mounted 3D Profiling Sonar revealed a two-layer erosion threshold system: a surface "fluffy layer" with  $\tau_{ce} = 0.06 \text{ Pa}$  overlying a consolidated seabed with  $\tau_{ce} = 0.13 \text{ Pa}$ . The latter value aligns with

Dong et al. (2020)'s summer calibration, suggesting that Dong et al. (2020)'s laboratory measurements, potentially affected by sediment consolidation during sample transport, might have missed the lower  $\tau_{ce}$  of the surface fluffy layer. Based on these consistent findings, we implemented a seasonal  $\tau_{ce}$  adjustment factor of 1.73 (winter/summer) in our model configuration (Table 1).

**Table 1.** CSTM model Sediment Properties

Source	Seabed			Pearl River	
Class	<u>1</u>	<u>2</u>	<u>3</u>	<u>4</u>	<u>5</u>
Sediment Type	Clay	Silt	Sand	single grains	flocs
$w_s$ (mm s <sup>-1</sup> )	0.02 <sup>c</sup>	1.2 <sup>c</sup>	57 <sup>d</sup>	0.005 <sup>c</sup>	0.6 <sup>c</sup>
Summer $\tau_{ce}$ (Pa)	0.14 <sup>cg</sup>	0.03 <sup>c</sup>	0.27 <sup>d</sup>	0.15 <sup>abfg</sup>	0.05 <sup>abcg</sup>
Winter $\tau_{ce}$ (Pa)	0.24 <sup>cf</sup>	0.05 <sup>cf</sup>	0.47 <sup>df</sup>	0.26 <sup>abf</sup>	0.09 <sup>abcf</sup>
Fraction	Spatially variable, see Figure 2g-i			40% <sup>ab</sup>	60% <sup>ab</sup>

<sup>a</sup>Zhang et al. (2019), <sup>b</sup>Zhang et al. (2021), <sup>c</sup>Ralston et al. (2012), <sup>d</sup>Warner et al. (2017), <sup>e</sup>Calibrated, <sup>f</sup>(Dong et al., 2020), and <sup>g</sup>Cao et al. (2025).

~~Here, we define the Pearl River sediment as the last two types of the specified sediment classes. Specifically, the fractions of clay and silt from the Pearl River were set at 40% and 60%, respectively, following Zhang et al. (2019) and Zhang et al. (2021). This approach allows for a better distinction between Pearl River sediment and seabed sediment, enabling separate analysis of the suspension, transport, and deposition of Pearl River sediment (Harris et al., 2008; Zhang et al., 2019). The~~

~~settling velocity, critical shear stresses, and other parameters were set following previous studies or were based on model calibration (Ralston et al., 2012; Warner et al., 2017; Zhang et al., 2019; Zhang et al., 2021). To clarify, the following analysis does not include riverine sediment during the spin-up time, as this sediment was already classified as seabed sediment categories (clay and silt) by the beginning of the analysis in April 2017.~~

**Table 1.** CSTM-model Sediment Properties

Sediment Class	Clay (bed)	Silt (bed)	Sand (bed)	Clay (river)	Silt (river)
Grain-size ( $\mu\text{m}$ )	4	32	500 <sup>d</sup>	1.84 <sup>ab</sup>	11.7 <sup>ab</sup>
Settling velocity ( $\text{mm s}^{-1}$ )	0.02 <sup>e</sup>	1.2 <sup>e</sup>	57 <sup>d</sup>	0.005 <sup>e</sup>	0.6 <sup>e</sup>
Critical stresses (Pa)	0.14 <sup>e</sup>	0.03 <sup>e</sup>	0.27 <sup>d</sup>	0.15 <sup>ab</sup>	0.05 <sup>abe</sup>
Fraction	Spatially variable, see Figure 2g-i			40% <sup>ab</sup>	60% <sup>ab</sup>
Erosion rate ( $\text{kg m}^{-2} \text{s}^{-1}$ ) <sup>e</sup>	$1 \times 10^{-4}$	$1 \times 10^{-4}$	$1 \times 10^{-4}$	$1 \times 10^{-4}$	$1 \times 10^{-4}$
Bottom porosity <sup>ab</sup>	0.672	0.672	0.672	0.672	0.672

<sup>a</sup>Zhang et al. (2019); <sup>b</sup>Zhang et al. (2021); <sup>c</sup>Ralston et al. (2012); <sup>d</sup>Warner et al. (2017); <sup>e</sup>Calibrated.

## 3.2.5 Wet and dry season regimes

The study area exhibits pronounced seasonal variability, which can be distinctly categorized into two primary seasons (Dong et al., 2004; Su, 2004; Liu et al., 2014; Zhang et al., 2021). ~~Seasonal variations in the study area are pronounced and can be broadly classified into two distinct seasons.~~ This seasonal classification is

supported by multiple environmental parameters. Various indicators such as, including river freshwater discharge, riverine sediment load (Figure 3a), wind patterns (Figure 3b), air temperature (Figure 3c), and modelled wave conditions (Figure 3d-f) at the a representative site (21.5°N, 114°E; corresponding to station W1 in Figure S1a, located immediately south of, just below the PRE) are utilized to characterize these seasons (Figure 3). The meteorological data for wind and air temperature were obtained from the NCEP reanalysis dataset, while wave parameters were derived from numerical model simulations. These comprehensive indicators collectively characterize the distinct seasonal patterns observed in the study area (Figure 3). The entire year (from April 1, 2017, to March 31, 2018) is typically divided into two main seasons: wet summer (from April 1, 2017, to September 30, 2017) and dry winter (from October 1, 2017, to March 31, 2018).

During the wet summer season, freshwater discharge tends to be notably high, often exceeding  $10,000 \text{ m}^3 \text{ s}^{-1}$  and reaching a maximum of  $53,000 \text{ m}^3 \text{ s}^{-1}$ , with an average value of  $15,266 \text{ m}^3 \text{ s}^{-1}$ . This discharge constitutes a significant portion of the entire year, accounting for 72.06% of the annual total. During this period, the river carries a substantial sediment load of 32.85 megatons, constituting 95.17% of the total annual sediment transport. Additionally, the riverine sediment load during this period is substantial, totaling 32.83 megatons, which represents 95.1% of the total annual amount. Prevailing winds predominantly blow from the south. For example, Figure 3b depicts the average monthly wind vector direction during the summer months as northward, with weak southeasterly winds in April, May, and September, and

moderate southeasterly winds in July. June and August experience moderate southwesterly winds. The 2 m height air temperatures typically range between 20°C and 30°C. The daily average Hsig remains relatively low, with the monthly average Hsig less than 1 m. The wave propagation direction is generally consistent with the wind direction, being easterly in April and May, and southerly from June to September.

In stark contrast, the dry winter season demonstrates markedly lower runoff, typically falling below 10,000 m<sup>3</sup> s<sup>-1</sup>, with an average value of 5,953 m<sup>3</sup> s<sup>-1</sup>. The sediment load during this period is significantly reduced to merely 1.67 megatons, marking a substantial decrease compared to the wet summer season. ~~The sediment load during this period is merely 1.69 megatons, representing a significant decrease compared to the wet summer season.~~ Prevailing winds during the dry winter are predominantly northeasterly, with relatively high wind speeds. Except for moderate wind intensity in March, the monthly average wind speed in other months exceeds 5 m s<sup>-1</sup>. The 2 m height air temperatures typically range between 10°C and 25°C during this season. The wave propagation direction aligns with the prevailing northeasterly winds of the season, predominantly northeasterly.

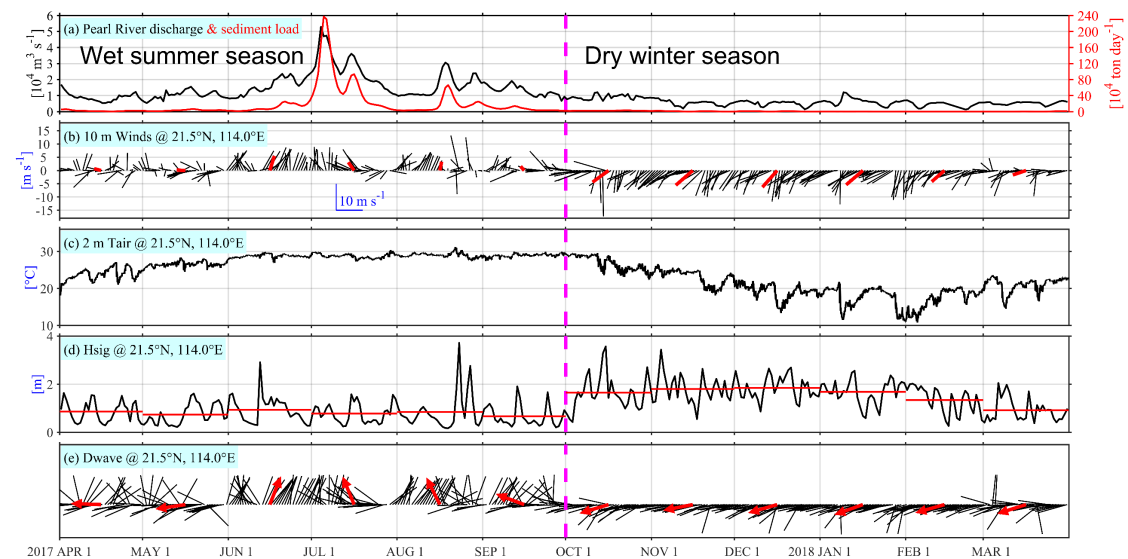
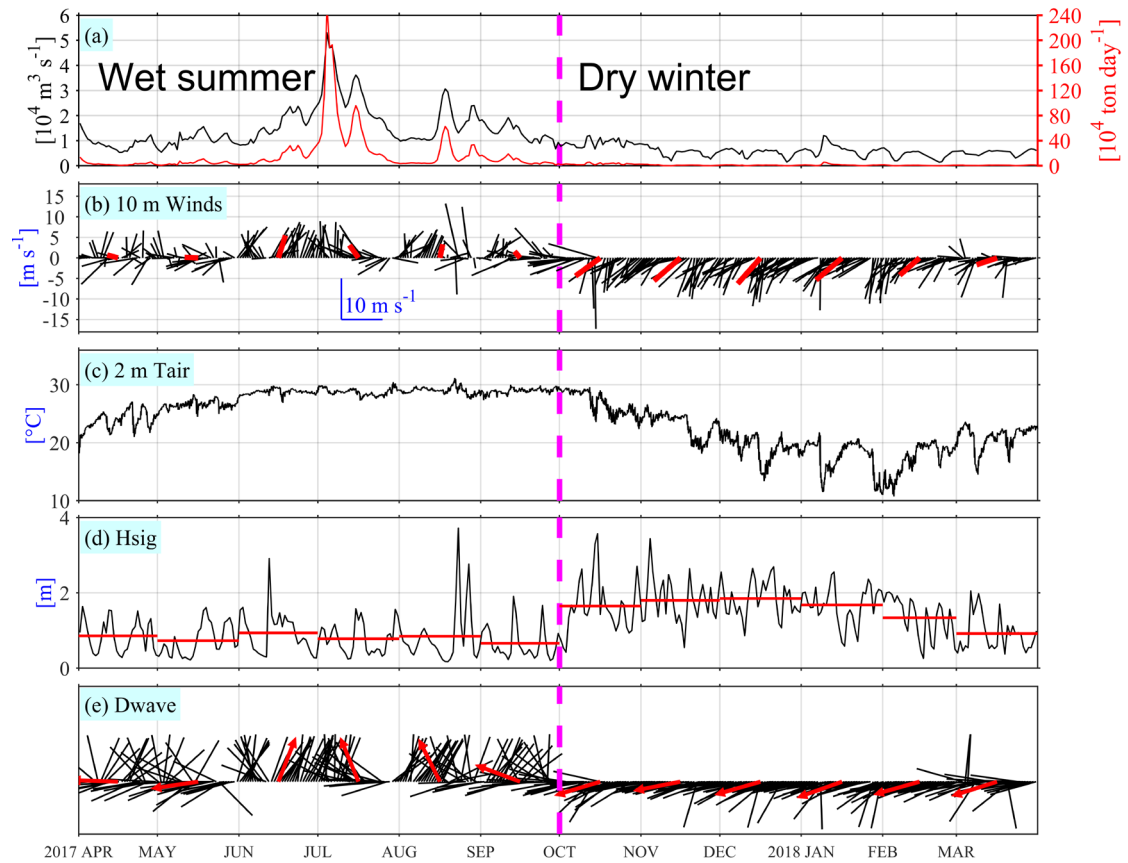


**Figure 3.** Time series of (a) the daily Pearl River freshwater discharge and sediment load, (b) daily (black vectors) and monthly (red vectors) averaged 10-meter height winds, (c) hourly 2-meter height air temperature, daily (black) and monthly (red)

averaged (d) significant wave height ( $H_{sig}$ , lines) and (f) wave propagation direction (vectors) weighted by  $H_{sig}^2$ . Two distinct seasons are delineated by the dashed magenta line.

## 3.2.6 Model experiments

~~Two model experiments, namely the Wind and wave (Case 1) and No wind or wave (Case 2) as detailed in Table 2, were undertaken to explore the intricate mechanisms shaping the impact of winds and waves on hydrodynamics and transport of riverine sediment. Case 1 encompassed a comprehensive wind and wave-current coupled experiment designed to emulate realistic conditions during simulation, achieved by integrating realistic wind inputs into the ROMS and SWAN models and specifying wave boundary conditions using nonstationary wave parameters derived from WAVEWATCH III model outputs. Conversely, Case 2 deliberately excluded any wind and wave effects by setting the wind speed to zero in both the ROMS and SWAN models and deactivating the wave boundary conditions. Consequently, the influence of waves and near-inertial motion induced by winds remained unaccounted for in Case 2.~~

To assess the relative importance of tides, waves, ambient shelf currents and residual water levels, seasonal variation in critical shear stress for erosion, the settling velocity, and the sediment initial conditions in the transport and dispersal of Pearl River-derived sediments, we conducted seven simulation experiments. Exp 1 (the *Control* run) incorporated all the aforementioned forcing agents (including winds) and



accounted for the seasonal variation in critical shear stress for erosion, with the winter critical shear stress for erosion set to be 1.73 times of that in summer. Exp 2 (*NTS* hereafter) was identical to Exp 1 but excluded tides, while Exp 3 (*NWS* hereafter) excluded waves. In Exp 4 (*NAS* hereafter), waves, tides, and the seasonal variation in critical shear stress for erosion were included, but the shelf current and residual water levels was omitted (i.e., no subtidal circulation forcing at open boundaries) to examine the influence of the South China Sea circulation. Then, Exp 5 (*NVS* hereafter) was identical to Exp 1, except that it did not account for the seasonal variation in critical shear stress for erosion, keeping the winter and summer values the same. Exp 6 (*DSV* hereafter) was identical to Exp 1, except that it set double sediment settling velocity of the Exp 1. Finally, to evaluate the model's sensitivity to sediment initial conditions, particularly focusing on the retention of riverine sediments within the water column and the seabed, we utilized the Control run's Class 1-5 sediment suspensions and depositions recorded on March 31, 2018, as alternative initial conditions for the five sediment classes. This configuration was implemented in the second control simulation, designated as Exp 7 (*Cycle* hereafter). Consequently, this setup introduces a full year's worth of Pearl River-derived sediment suspensions and depositions into the model domain at the start of the *Cycle* experiment.

In all experiments, we implemented the Charnock approach within COAWST's bulk air-sea flux parameterization scheme to calculate surface wind stress using the NCEP 10-m wind product (Charnock, 1955; Fairall et al., 1996), ensuring consistency in wind stress forcing across all simulations.

**Table 2.** ROMS and SWAN model settings for different cases

Case ID	ROMS			SWAN	
	Discharges	Tides	Winds	Winds	BF
Wind and wave (Case 1)	✓	✓	✓	✓	✓
No wind or wave (Case 2)	✓	✓	*	*	*

Discharges refer to the freshwater and riverine sediment released from eight PRE-outlets, BF refers to SWAN boundary forcing from the WWII.

In Case 1, the surface roughness and surface stress contribution by waves were assessed using the method proposed by Drennan et al. (2005). Additionally, the wave-current bottom boundary module based on Madsen (1994), incorporated into COAWST, was activated to simulate the wave-current bottom boundary layer. The vortex force module of wave forces was also activated to compute the wave-induced momentum flux, utilizing the method proposed by McWilliams et al. (2004) and implemented in COAWST by Kumar et al. (2012). In both cases (Case 1 and Case 2), the bottom friction was computed based on a logarithmic velocity profile (Warner et al., 2008).

## 4.3 Results

### 4.3.1 Seasonal hydrodynamics and Pearl River-derived sediment transport patterns~~wave variations and its effects on bottom shear~~

**stress**

We quantified the spatial distributions of seasonal mean wind stress, Hsig, wave bottom orbital velocity (WBOV), and bottom shear stress for both the wet summer and dry winter periods (as defined in Section 2.5). These distributions serve as representative hydrodynamic conditions for typical summer and winter scenarios, respectively (Fig. 4).

During summer, the prevailing winds predominantly originate from south, with the average wind stress generally below 0.03 Pa, except in the eastern coastal waters of Hainan Island, where localized values reach up to 0.05 Pa (Fig. 4a). In contrast, during the dry winter season, the prevailing winds shift to a northeasterly direction, resulting in generally higher average wind stress compared to summer (Fig. 4b), with values typically exceeding 0.1 Pa in areas deeper than 40 m and surpassing 0.2 Pa in the offshore eastern Guangdong Coast near the Taiwan Bank.

Corresponding to the seasonal wind stress (Figures ~~3e~~4a-b), the seasonally ~~-~~averaged wave characteristics in the PRE and the adjacent northern continental shelf of the South China Sea exhibit significant seasonal ~~changes~~variations (Figures 4c-d).

During the wet summer season, the Hsig in these areas is relatively low, with waves predominantly coming from the southeast (Figure ~~4a~~4c). The seasonal average Hsig across the entire shelf remains below 1 m, with areas deeper than 60 m showing Hsig values above 0.8 m, while in shallower nearshore regions (water depth < 20 m), Hsig is less than 0.6 m (Figure ~~4a~~4c). Corresponding to the lower Hsig in the wet summer, the seasonally-averaged WBOV~~wave bottom orbital velocity (WBOV)~~ is

also relatively small, generally less than  $1 \text{ cm s}^{-1}$  in areas deeper than 40 m, except in some nearshore shallow water regions where it reaches up to  $5\text{--}10 \text{ cm s}^{-1}$  (Figure 4e). The seasonally-averaged bottom shear stress during the wet summer is relatively high in the PRE, nearshore regions, and the Taiwan Bank, where tidal dissipation is strong (Figure 4g).

In the dry winter season, the  $H_{sig}$  increases significantly compared to the wet summer, with waves primarily coming from the northeast, although refraction occurs in some nearshore regions, changing the wave direction to southeasterly (Figure 4d). The area with water depths exceeding 60 m has a  $H_{sig}$  greater than 1.5 m, while in the 20-meter depth region, the  $H_{sig}$  reaches approximately 1 m (Figure 4d). Compared to the wet summer, the WBOV increases significantly in the PRE mouth and many nearshore regions, reaching up to  $10\text{--}20 \text{ cm s}^{-1}$  (Figure 4d). The average bottom shear stress on the continental shelf outside the estuary also increases significantly during the dry winter compared to the wet summer (Figure 4f). Compared to the No wind or wave case, the introduction of wind and waves leads to an increase in average bottom shear stress during the wet summer, particularly in regions where WBOV is significant, with an increase of approximately  $0.05\text{--}0.1 \text{ Pa}$  (Figure 4g).

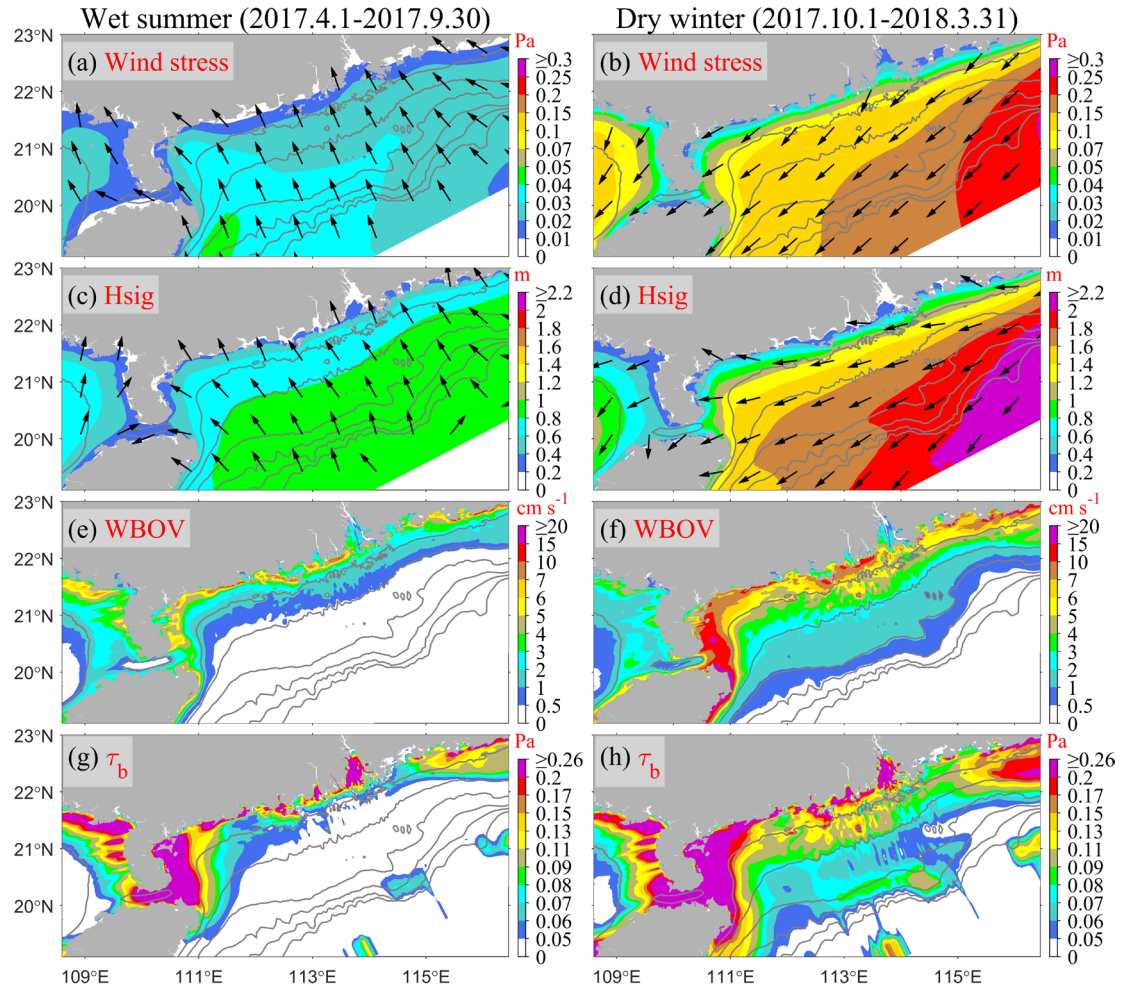


**Figure 4.** The patterns of variables are averaged for the wet summer season (April 1st to September 30th, 2017; Column 1) and the dry winter season (October 1st to March 31st, 2018; Column 2) in the Control case. Row 1 (a-b) depicts wind stress (color) and direction (vectors), Row 2 (c-d) shows Hsig (color) and propagation direction (vectors) weighted by Hsig<sup>2</sup>, Row 3 (e-f) presents wave bottom orbital velocity (WBOV), and Row 4 (g-h) displays bottom shear stress magnitude.

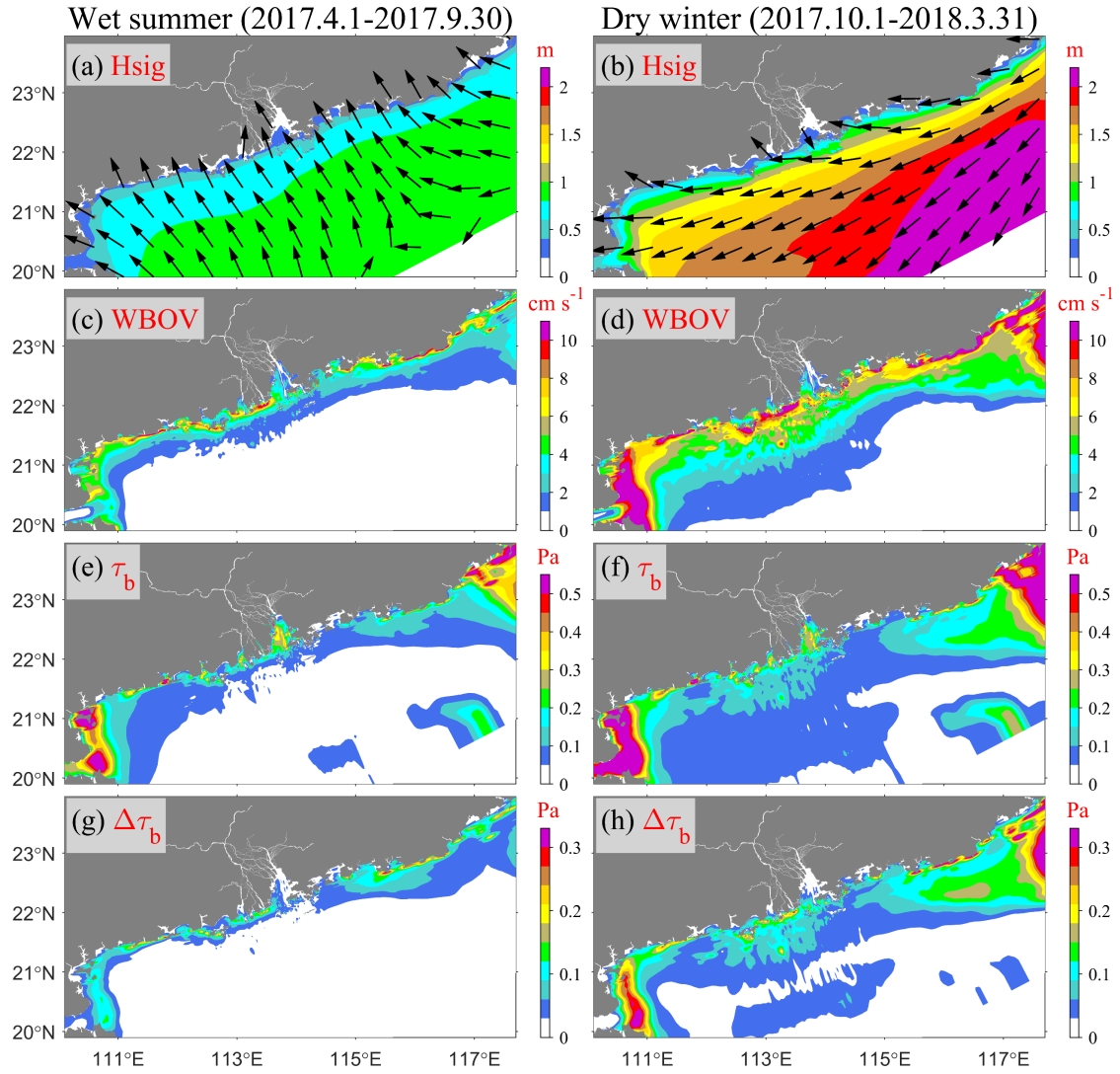


**Figure 4.** Patterns averaged over the entire wet summer season (from April 1st to September 30th, 2017, as follows, Column 1) and the dry winter season (from October 1st to March 31st, 2018, as follows, Column 2). Row 1 (a-b) for Hsig (color) and propagation direction (vectors) weighted by  $Hsig^2$ , Row 2 (c-d) for wave bottom orbital velocity (WBOV), Row 3 (e-f) for bottom shear stress magnitude in Case 1 (Wind and wave case). Row 4 (g-h) for bottom shear stress magnitude differences between two cases (Case 1 minus Case 2).

In the dry winter season, Hsig in the study area increases significantly compared

to the wet summer, with waves primarily coming from the northeast, although refraction occurs in some nearshore regions, changing the wave direction to southeast (Figure 4b). The area with water depths exceeding 60 m has a  $H_{sig}$  greater than 1.5 m, while in the 20-meter depth region, the  $H_{sig}$  reaches approximately 1 m (Figure 4b). Compared to the wet summer, the WBOV increases significantly in the PRE mouth and many nearshore regions, reaching up to  $10 \text{ cm s}^{-1}$  (Figure 4d). The average bottom shear stress on the continental shelf outside the estuary also increases significantly during the dry winter compared to the wet summer (Figure 4f). Since tidal intensity remains almost unchanged, the seasonal variation in tidal-induced stress is minimal, and the observed seasonal increase is mainly due to the stronger winter waves generating larger WBOV on the shelf. Compared to the No wind or wave case, the introduction of wind and wave in the dry winter leads to an increase in average bottom shear stress by approximately 0.1–0.15 Pa, with winter-averaged values reaching up to 0.3 Pa in areas such as the Taiwan Bank and east of the Leizhou Peninsula (Figure 4h).

## 4.2 Seasonal dispersal patterns of Pearl River plume and sediment

The patterns of residual sediment dispersal, flux, and deposition over throughout the simulation period provide clear information on the mechanisms ~~vividly illustrate~~ patterns of ~~for~~ sediment redistribution on both an annual or and seasonal timescales ~~scale~~. This section presents a detailed analysis of ~~primarily focuses on illustrating~~ the seasonally averaged fields of salinity, flow, riverine SSC, ~~wind stress~~, depth-integrated riverine sediment flux, and riverine sediment deposition patterns

during the wet summer season (Figure 5) and dry winter season (Figure 6) on the continental shelf.

During the wet summer season, the Pearl River discharges a significant amount of freshwater and sediment ~~from the Pearl River is substantial~~ (Figure 3a), resulting in ~~leading to an~~ extensive ~~widespread~~ expansion of the river plume into the sea, primarily in the surface layer (Figure 5a-b). The river plume extends ~~expands~~ both eastward and westward along the coastline ~~coast~~ (Figure 5a). Due to the influence of southerly winds (Figure ~~5b~~4a) and ambient shelf currents, the ~~speed~~ extent of the river plume extending eastward is significantly higher than that extending westward.

In terms of riverine sediment suspension, its maximum turbidity zone ( $\sim 100 \text{ mg L}^{-1}$ ) is situated in the shallow water area ~~near~~ within the estuary (water depth  $< 10 \text{ m}$ ). Beyond the estuary, suspended riverine sediment disperses across the shelf through the river plume. Further away from the estuary, its distribution aligns with that of the river plume, with concentrations diminishing as dispersal distance increases. Integrating the horizontal flux of riverine sediment vertically offers a clear indication of the primary transport pathway of riverine sediment (Figure ~~5e~~5e). The riverine sediment exhibits both westward and eastward fluxes (Figure 5e). ~~Riverine sediment is predominantly transported westward and eastward.~~ Westward coastal transport can extend as far as ~~to~~ the Leizhou Peninsula and Hainan Island. On the eastern side, the eastward transport extends toward ~~can reach the~~ Taiwan Bank. However, the primary transport pathway is diverted southward (Figure 5e); due to the obstruction ~~of~~ caused by summer upwelling ~~at Taiwan Bank~~ near the Guangdong east coast (Chen et al.,



2017a;Chen et al., 2017b), as evidenced by the cross-shore current in the bottom layer (Figure 5b), ~~the transport path is diverted southward.~~ The westward transport pathway follows the region where the water depth is shallower than 30 m, with a riverine sediment flux of  $10\text{--}20\text{ g}^{-1}\text{ m s}^{-1}$ . In contrast, the eastward transport pathway occurs in the 30–60 m depth range, but the riverine sediment flux is below  $10\text{ g}^{-1}\text{ m s}^{-1}$ . ~~The westward transport pathway is narrow and has a large magnitude of riverine sediment flux, while the eastward transport pathway is wide but the magnitude of riverine sediment flux is relatively weak.~~ Throughout the wet summer season, substantial amounts of riverine sediment are deposited near the estuary (Figure 5d), particularly leading to notably high deposition of riverine sediment near the river mouth ~~bar~~( $> 100\text{ mm}$ ). Outside the estuary, the thickness of riverine sediment is comparatively lower, but it can reach approximately  $\sim 0.5\text{ mm}$  during the wet summer season in certain areas off the coast of western Guangdong.

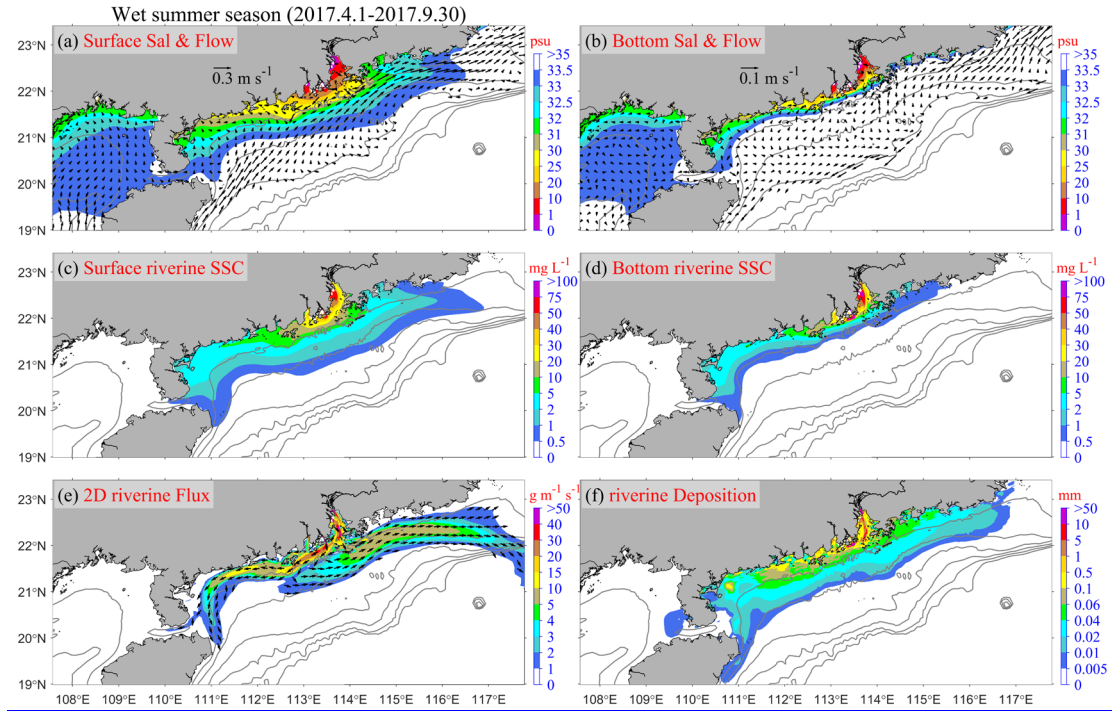


**Figure 5.** Patterns averaged over the entire wet summer season in the Control case: (a) surface and (b) bottom salinity (color, psu) and flow (arrows,  $\text{m s}^{-1}$ ); (c) surface and (d) bottom riverine SSC ( $\text{mg L}^{-1}$ ); (e) depth-integrated riverine sediment transport rate (color,  $\text{g m}^{-1} \text{s}^{-1}$ ) and direction (arrows); and (f) riverine deposition thickness during the wet summer season (mm). Flow vectors in regions with water depths exceeding 100 m are masked for clarity.

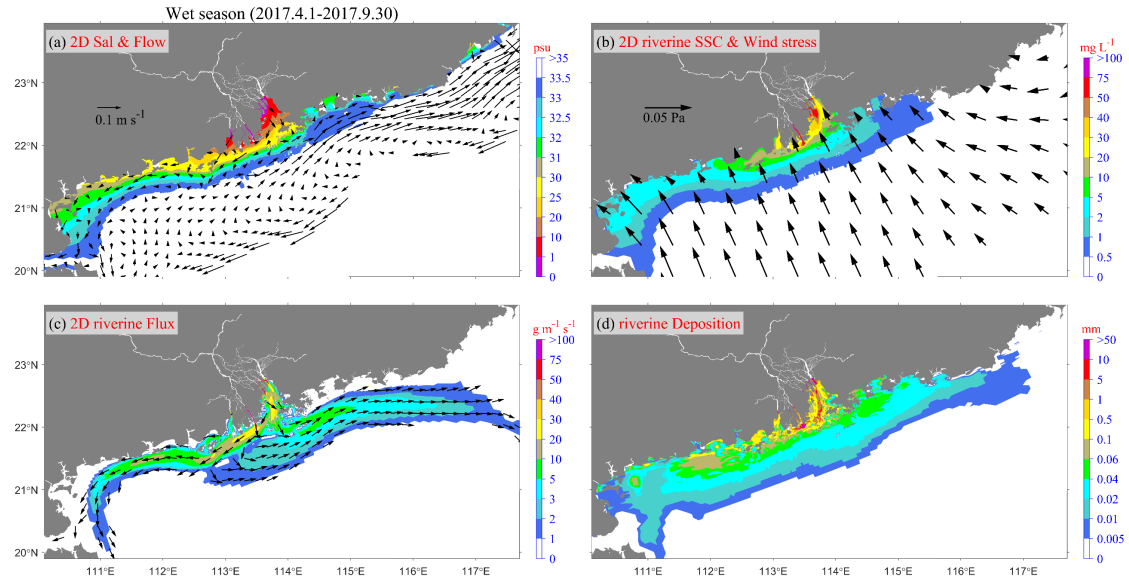


**Figure 5.** Patterns averaged over the entire wet summer season in Wind and wave case. (a) depth averaged salinity (color, psu) and flow (arrow,  $\text{m s}^{-1}$ ). (b) depth averaged riverine SSC ( $\text{mg L}^{-1}$ ). (c) depth-integrated riverine sediment transport rate (color,  $\text{g m}^{-1} \text{s}^{-1}$ ) and direction (arrow). (d) riverine deposition thickness during the wet season (mm).

During the dry winter season, runoff from the Pearl River significantly decreases compared to the wet summer (as indicated in Figure 3a), accompanied by strong northeasterly winds (Figure 4b). Consequently, the expansion of the Pearl River plume is constrained to the westward direction only, resulting in a narrow cross-shore width of the plume and the formation of a strong horizontal salinity gradient outside the estuary (Figure 6a). Flow velocity is increased near the salinity front, allowing river plume to extend westward through the Qiongzhou Strait to the Beibu Gulf. With sediment load during winter nearly negligible, the suspended concentration of riverine

707 sediment is significantly lower compared to the wet summer (Figure 6b). In areas  
708 beyond the estuary, it is typically less than ~~5~~3 mg L<sup>-1</sup>, whereas inside the estuary, it is  
709 around ~~~10~~~5 mg L<sup>-1</sup>. During the dry winter, following the transport path of river  
710 plume, riverine suspended sediment primarily moves westward along the coast,  
711 deflecting southward along the topography near the Leizhou Peninsula (Figure 6c). It  
712 then bifurcates near the east entrance of the Qiongzhou Strait, with one branch  
713 continuing into the Beibu Gulf, and the other branch proceeding southward along the  
714 east coast of Hainan Island. Stronger winds and waves in the dry winter lead to the  
715 resuspension of a considerable amount of riverine sediments, originally deposited in  
716 estuaries and shelf seas during summer~~;~~. The resuspended sediments ~~which~~ are then  
717 transported to coastal bays as well as to the sides and rear of the islands (Figure 6d).  
718 Additionally, a portion of the riverine sediment transported to the Beibu Gulf gets  
719 deposited on the seabed during the dry winter season.

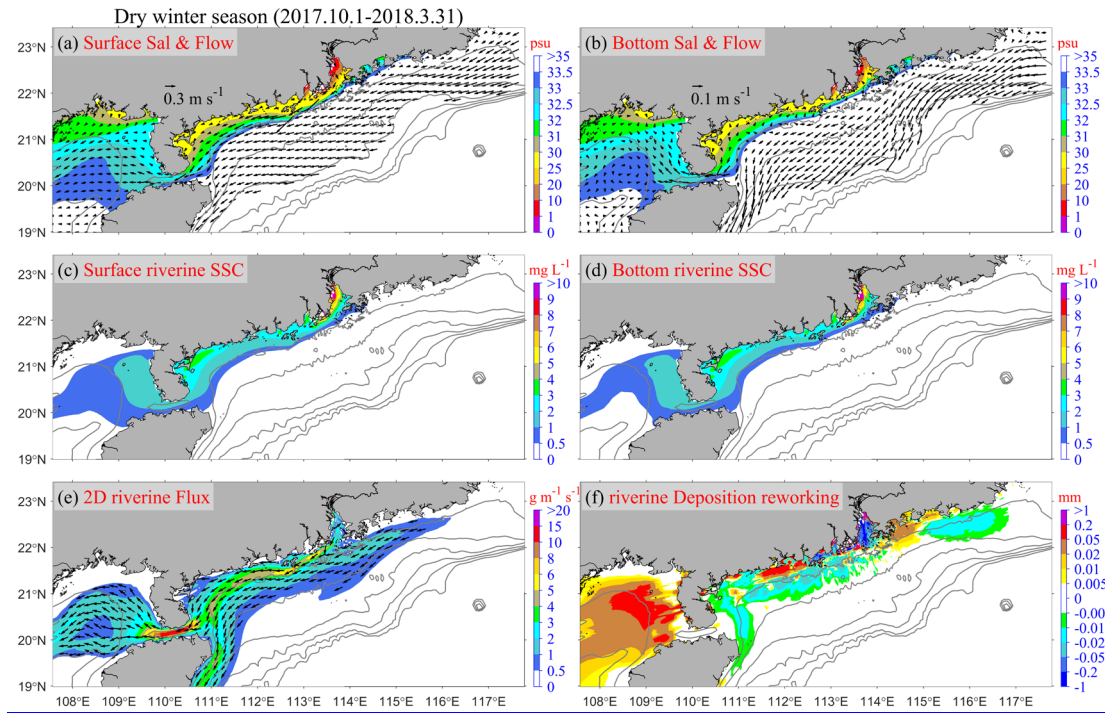
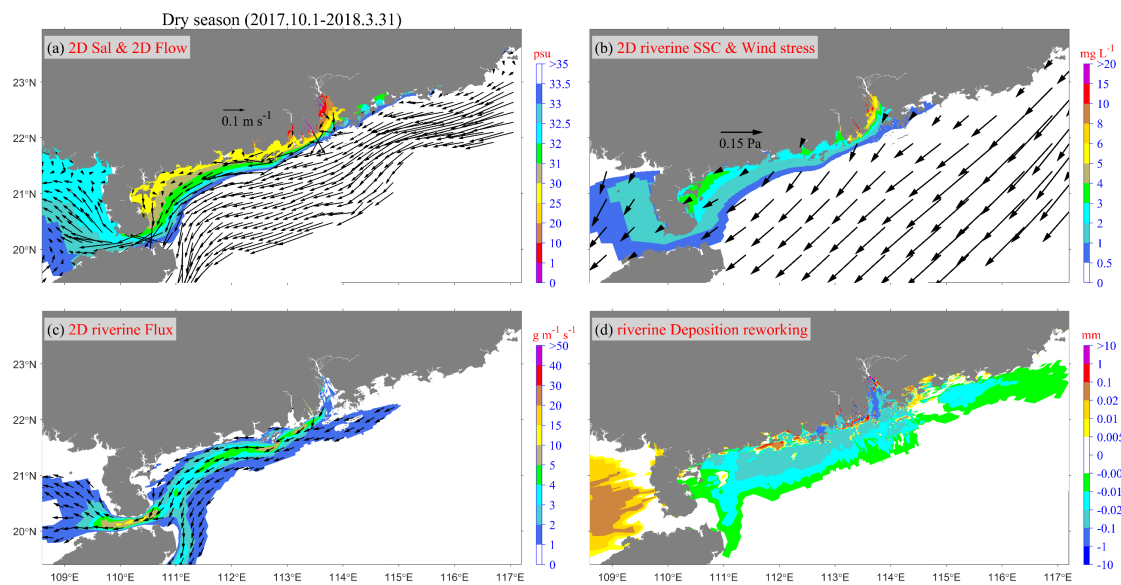


**Figure 6.** Same as Figure 5, but for the dry winter season in the Control case. Notably, (f) illustrates the changes in riverine sediment deposition on the seabed at the end of the dry winter season compared to the end of the wet summer season.



~~Figure 6. Same as Figure 5, but pertains to the dry winter season in Wind and wave case. Notably, (d) illustrates the variations in riverine sediment deposition on the seabed relative to the end of the wet summer season.~~

### 3.2 Riverine sediment budgets and annual deposition over the shelf

### ~~4.3 Annual dispersal pattern and the effect of winds and waves~~

To improve the understanding of the spatial-temporal variabilities in the riverine sediment dispersal, and the estimation of the fate of the Pearl River sediment during the wet summer season, dry winter season, and throughout the year, we partitioned the model domain into eight distinct regions delineated by various transects as illustrated in Figure 1. The division criteria are mainly based on the distance from the estuary and the natural separation by the Leizhou Peninsula and Hainan Island. These areas include:

- ① Proximal region: Proximity to the estuary,
- ② Southern region: Located deeper in the southern part of the estuary,
- ③ Eastern region: Eastern side of the estuary, closer to the shoreline,
- ④ Southeastern region: Further offshore on the eastern side of the estuary,
- ⑤ Western region: Western side of the estuary, closer to the shoreline,
- ⑥ Southwestern region: Offshore on the western side of the estuary,
- ⑦ Gulf region: Mainly the Beibu Gulf,
- ⑧ Distal region: South of the Hainan Island.

By dividing the model domain into these delineated regions, we calculated the riverine sediment flux for each transect, thereby determining the total riverine

sediment volume retained in each region. Additionally, Figure 7a-c illustrates the proportion of riverine sediment retention budget within each region, expressed as a percentage of the total annual river sediment input, for the wet summer season, the dry winter season, and the entire year under the Control run case, respectively. Meanwhile, Figure 7d illustrates the annual deposition over the shelf.

The retention of Pearl River sediment on the continental shelf exhibits significant seasonal variations (Figure 7a-c). During summer (characterized by high discharge and low wind/waves), the PRE and continental shelf receive 95.17% of the annual sediment load from the Pearl River (Figures 3a and 7a). Approximately two-thirds of this sediment is retained in the "Proximal" region (Figure 7a). Additionally, influenced by the prevailing southerly winds and northeastward background circulation, 13.01% of the annual sediment load is retained on the shelf east of the PRE, specifically in the "Eastern" and "Southeastern" regions. Meanwhile, the shelf west of the PRE retains 15.87% of the annual load, with the "Western" region being the primary receiver, accounting for 8.48%. Only 0.92% and 2.3% of the annual load enter the "Gulf" and "Distal" regions, respectively, during summer. The "Southern" region retains a mere 1.33% of the sediment. In winter (characterized by low discharge and energetic winds/waves), the PRE and continental shelf receive only 4.83% of the annual sediment load (Figures 3a and 7b). The sediment distribution during this season is primarily a result of the dynamic reworking of the sediments of summer deposition (Figure 7b). While the "Proximal" region continues to receive sediment, with a 1.38% increase in retention, the other five regions east of the Leizhou Peninsula and Hainan

Island experience a decrease in sediment retention. This sediment is predominantly transported and retained to the more distant "Gulf" and "Distal" regions. The annual sediment budget reveals that 66.45% of the Pearl River sediment is retained in the "Proximal" region. Additionally, 9.2% is retained on the shelf east of the estuary, primarily during summer, while 24.12% is retained on the shelf west of the estuary, with the majority deposited in the distal regions of the Beibu Gulf and south of Hainan Island, mainly during winter.

The annual deposition thickness of Pearl River sediments, as illustrated in Figure 7d, reveals significant proximal deposition within and near the estuary, with many areas exceeding 10 mm despite winter resuspension and transport. Additionally, deposition on the inner shelf (water depth <60 m) to the east of the PRE reached a magnitude of 0.1 mm, while the western shelf of the PRE exhibited significantly greater accumulation. For instance, the deposition west of the Chuanshan Islands reached a magnitude of 0.5 mm. In the Beibu Gulf region, deposition was primarily concentrated in the northeastern part of the gulf, extending southwestward along the 30-60 m isobaths. Sediments transported southwestward along the eastern coast of Hainan Island and retained in the "Distal" regions did not predominantly settle on the seabed due to the greater water depth but remained largely suspended in the water column.



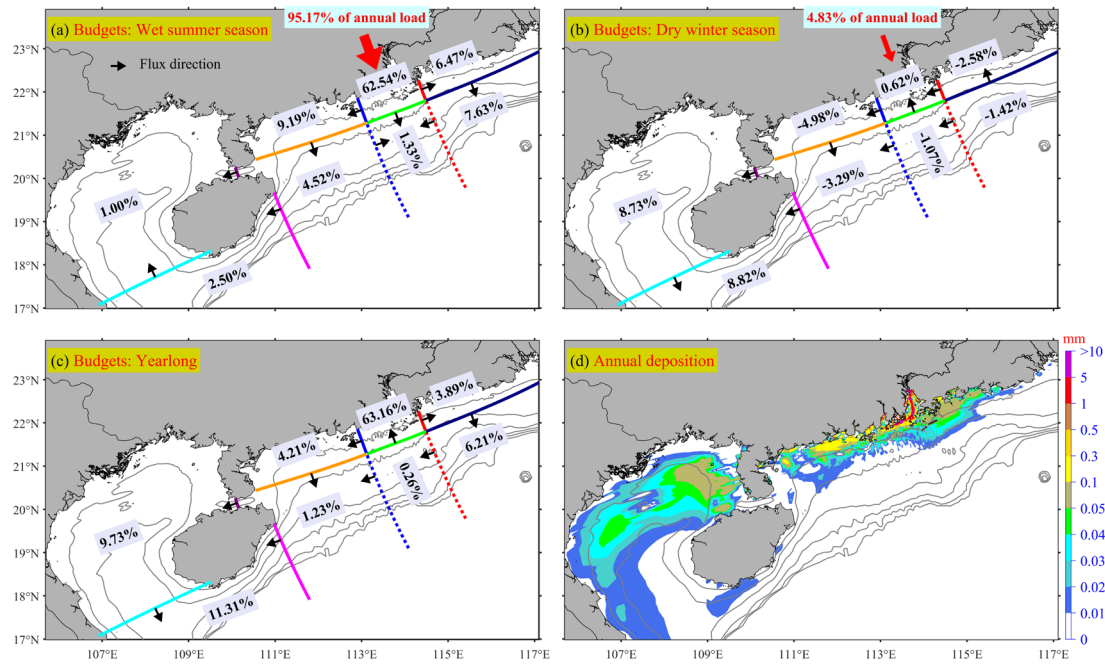


**Figure 7.** Riverine sediment retention budget percentages at eight regions during (a) the wet summer season, (b) the dry winter season, and (c) the entire year in the Control run case. (d) Same as Figure 5d, but shows the annual deposition patterns spanning from April 1st, 2017, to March 31st, 2018 in the Control Run. All percentages displayed in the figure are relative to the annual riverine sediment load. The black percentage values represent the combined total of riverine sediment Class 4 and Class 5, while the red and blue values denote sediment Class 4 and Class 5, respectively. Arrows indicate the direction of net riverine sediment flux at each transect during the specified period.

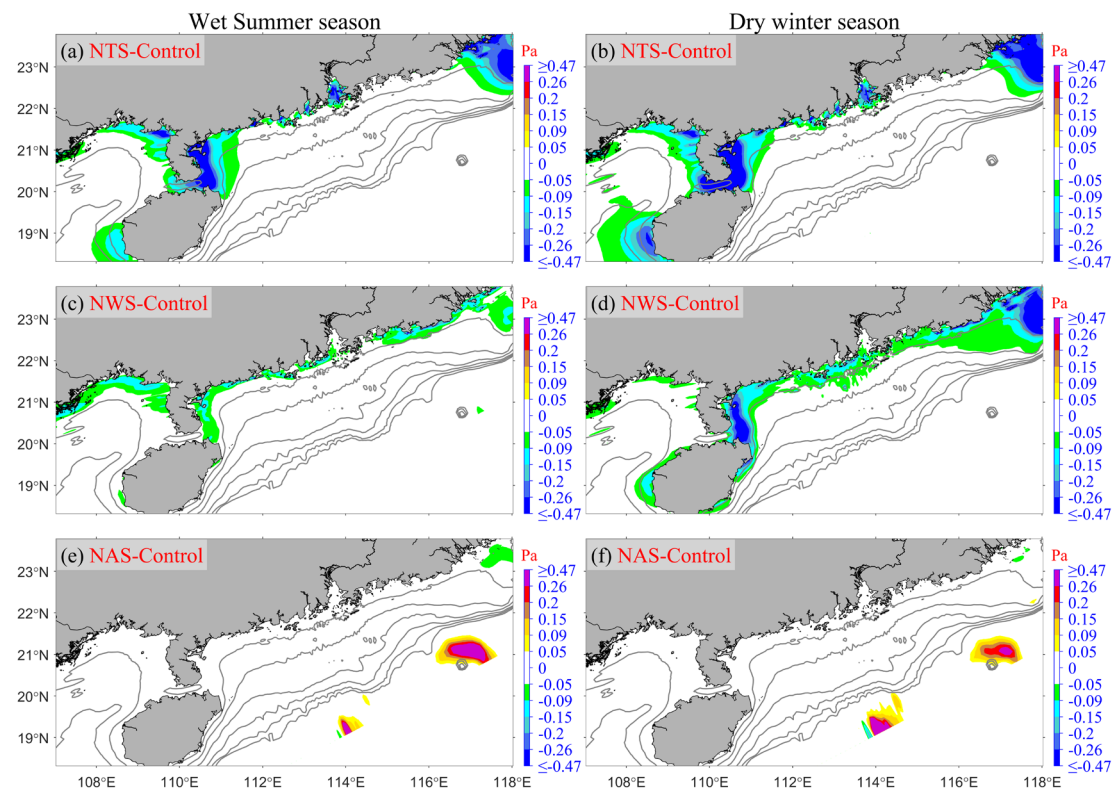
### 3.3 Model sensitivity experiments: relative roles of physical processes, sediment properties, and initial conditions

Six sensitivity simulations, namely Exp 2-7 (NTS, NWS, NAS, NVS, DSV, and

Cycle), were conducted. As the latter three experiments do not impact hydrodynamics, we focus on presenting the seasonal mean differences in bottom shear stress between the Control run and the first three cases (NTS-Control, NWS-Control, NAS-Control) for both summer and winter (Figure 8).

Tidal and wave forces significantly influence bottom stress. In the NTS case, where tidal forces were excluded, the underestimation of bottom shear stress was similar in both summer and winter due to the minimal seasonal variation in tidal intensity. This underestimation primarily occurred in the PRE, around the Taiwan Bank, and near the Leizhou Peninsula (Figure 8a-b). In contrast, the NWS case, which excluded wave forces, showed a greater underestimation in winter than in summer, reflecting the intense seasonal variability of wind and wave activities (Figure 3b, 3d-e, and 4a-f). Unlike the NTS case, the NWS case mainly underestimated the bottom stress in the nearshore areas outside the PRE, though it similarly underestimated the bottom stress around the Taiwan Bank and the eastern side of the Leizhou Peninsula (Figure 8c-d). For the NAS case, where ambient shelf currents and residual water levels at the model boundaries were excluded, the impact on bottom stress was minimal compared to the NTS and NWS cases. The effect was almost negligible on the inner shelf at depths less than 100 m, with widespread impacts generally below 0.02 Pa. Some overestimations were noted in localized deeper areas near the boundaries, probably being artifacts, but these changes in bottom stress, being distant from the Pearl River sediment distribution areas, did not affect the dynamics of the Pearl River sediment (Figure 8e-f).

828



829

830 **Figure 8.** The seasonal mean differences in bottom shear stress between the Control  
 831 run and the following cases: (a-b) NTS (NTS minus Control), (c-d) NWS (NWS  
 832 minus Control), and (e-f) NAS (NAS minus Control). The first column represents the  
 833 wet summer season, while the second column corresponds to the dry winter season.

834

835 Following the bottom shear stress analysis (Figure 8), we analyzed seasonal  
 836 sediment transport and deposition patterns by comparing the control run with six  
 837 sensitivity experiments (NTS-Control, NWS-Control, NAS-Control, NVS-Control,  
 838 DSV-Control, and Cycle-Control) (Figures 9-11). The study focuses on Pearl  
 839 River-derived sediment dynamics, indicated by surface circulation and SSC  
 840 distributions patterns (Figures 5 and 6). Specifically, Figures 9 and 10 present

seasonal surface currents and SSC differences between control and sensitivity runs, complemented by deposition pattern differences in Figure 11.

For the NTS case versus the Control case, tides significantly affected bottom stress (Figures 8a-b) but had minimal impact on the mean circulation (Figures 5a, 6a, and 9a-b). The exclusion of tides substantially reduced bottom shear stress in the PRE and near the Leizhou Peninsula, weakening sediment resuspension. Consequently, increased deposition of Pearl River-derived sediments occurred in the PRE, its adjacent areas, and on both sides of the Leizhou Peninsula (Figure 11a). During summer, riverine SSC notably decreased in the PRE and the inner shelf east of the Leizhou Peninsula (Figure 9a). This reduction pattern persisted in winter, particularly in the PRE and on both sides of the Leizhou Peninsula (Figure 9b).

In the NWS case with waves excluded, like the NTS, NWS had a relatively minor impact on circulation (Figures 5a, 6a, and 9c-d). However, NWS underestimated the nearshore bottom stress (Figures 8c-d). This led to more Pearl River-derived sediment being deposited outside the PRE and in the nearshore shallow waters along the Guangdong Coastline (regions significantly affected by waves) (Figure 11b). Consequently, the riverine SSC in summer was much lower in the downstream of the PRE and on the inner shelf east of the Leizhou Peninsula (Figure 9c). This similar reduction pattern persisted in the winter, but is slightly in more western regions (Figure 9d).

For the NAS case in which ambient shelf currents and residual water levels at the model boundaries were excluded, the impact on bottom stress was minimal compared

to the NTS and NWS cases. However, NAS had a relatively large impact on the mean circulation (Figures 5a, 6a, and 9e-f). It mainly influenced the summer circulation. Specifically, ignoring these factors would cause the relatively strong northeastward flow along the Guangdong coast to become very weak (Figure 9e). When it comes to winter, the influence of NAS on circulation was relatively small. That is, in the absence of the background residual water level and residual current, due to the strong northeastward winds in winter, the overall circulation was still southwestward (Figure 9f). The underestimated northeastward flow in summer led to the Riverine SSC being scarcely transported to the vicinity of the Eastern Guangdong Coastline. Consequently, the Riverine SSC there was decreased (Figure 9e) and sediment deposition was significantly reduced (Figure 11c). Most of the suspended Riverine sediment was transported southwestward, resulting in an increase in the Riverine SSC along the Western Guangdong Coastline. In winter, since most of the suspended Riverine sediment had been transported southwestward in summer, the Riverine SSC decreased compared to the Control run (Figure 9f). Ultimately, NAS mainly caused a significant reduction in sediment deposition near the Eastern Guangdong Coastline, while sediment deposition increased in the Beibu Gulf and the "Distal" region (Figure 11c).

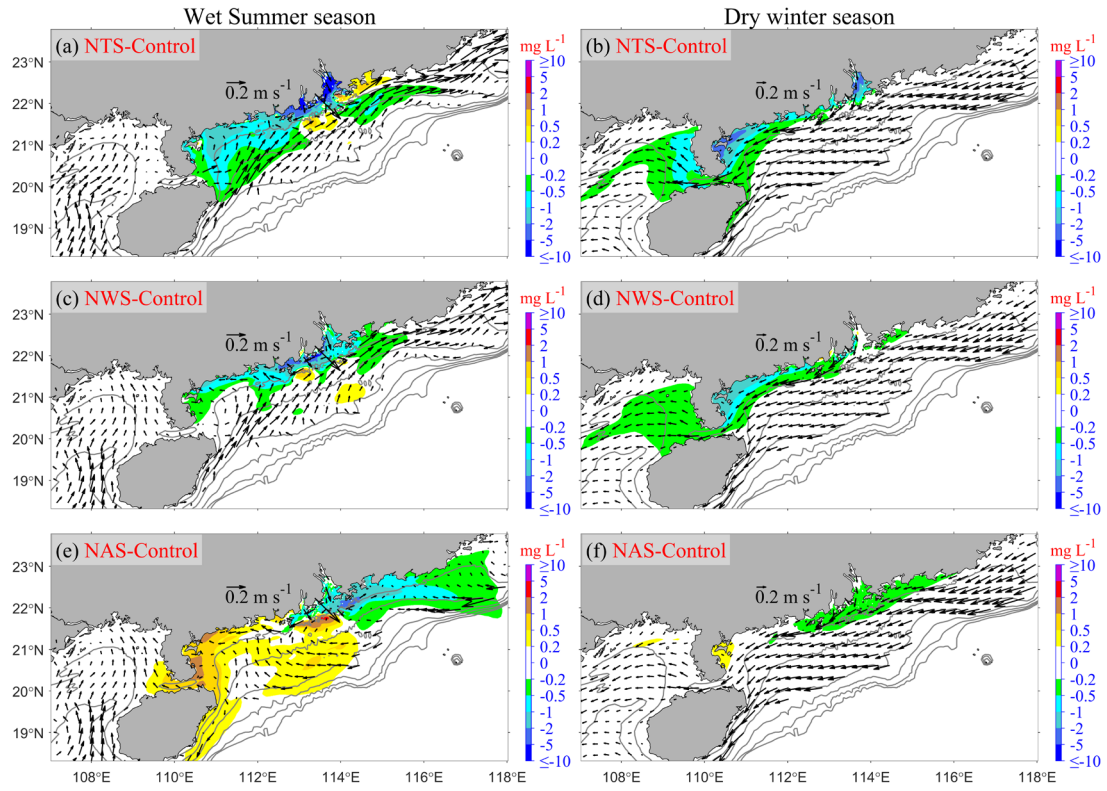


**Figure 9.** Same as Figure 8, but for seasonal mean differences in surface SSC between the Control run and the following cases: (a-b) NTS-Control, (c-d) NWS-Control, and (e-f) NAS-Control. The first column represents the wet summer season, while the second column corresponds to the dry winter season. Vectors show the seasonal mean surface current fields in each experiment.

For the NVS case, in which the winter and summer critical shear stress for erosion were kept identical, the summer conditions of NVS were precisely the same as those of the Control run (Figure 10a). Since the critical shear stress for erosion in winter was lower than that in the Control run, this led to an increase in re-suspension within the PRE, along the Western Guangdong Coastline, and in the Beibu Gulf area, resulting in an increase in Riverine SSC (Figure 10b). Eventually, this caused a

reduction in the deposition thickness of Pearl River-derived sediments on the continental shelf (Figure 11d).

In the DSV case, where sediment settling velocity was doubled compared to the Control run, riverine SSC patterns remained broadly similar between the two scenarios in both summer and winter. However, significant reductions occurred in the primarily high SSC areas, with regions of higher SSC in the Control run experiencing the most pronounced declines (Figures 5c, 6c, 10c-d). This enhanced settling velocity resulted in an increased deposition of Pearl River-derived sediments along the Guangdong coastline and the eastern Beibu Gulf, accompanied by a reduced deposition thickness in the western Beibu Gulf (Figure 11e).

In the Cycle case, the initial conditions for the five sediment classes were set using the Class 1-5 sediment suspensions and depositions from the Control run on March 31, 2018, initiating a second control simulation. This setup introduced a full year's result of Pearl River-derived sediment suspensions and depositions into the model domain at the start. Consequently, during the initial summer period, the Cycle case elevated riverine SSC in the primary depocenters identified in the Control run (Figures 7d and 10e), while this effect diminished by winter (Figure 10f). This experiment specifically examines the impact of pre-existing Pearl River-derived sediments in the water column and seabed on annual seabed budgets. To isolate this effect, the sediment thickness from the Control run's end on March 31, 2018, was subtracted as a baseline before comparing annual depositions with the Control run (Figure 11f). The Cycle case changed the downstream PRE deposition patterns, with

increased sediment accumulation in downstream regions and notable changes in deposition thickness in parts of the Beibu Gulf, revealing a long-term southwestward sediment transport trend.

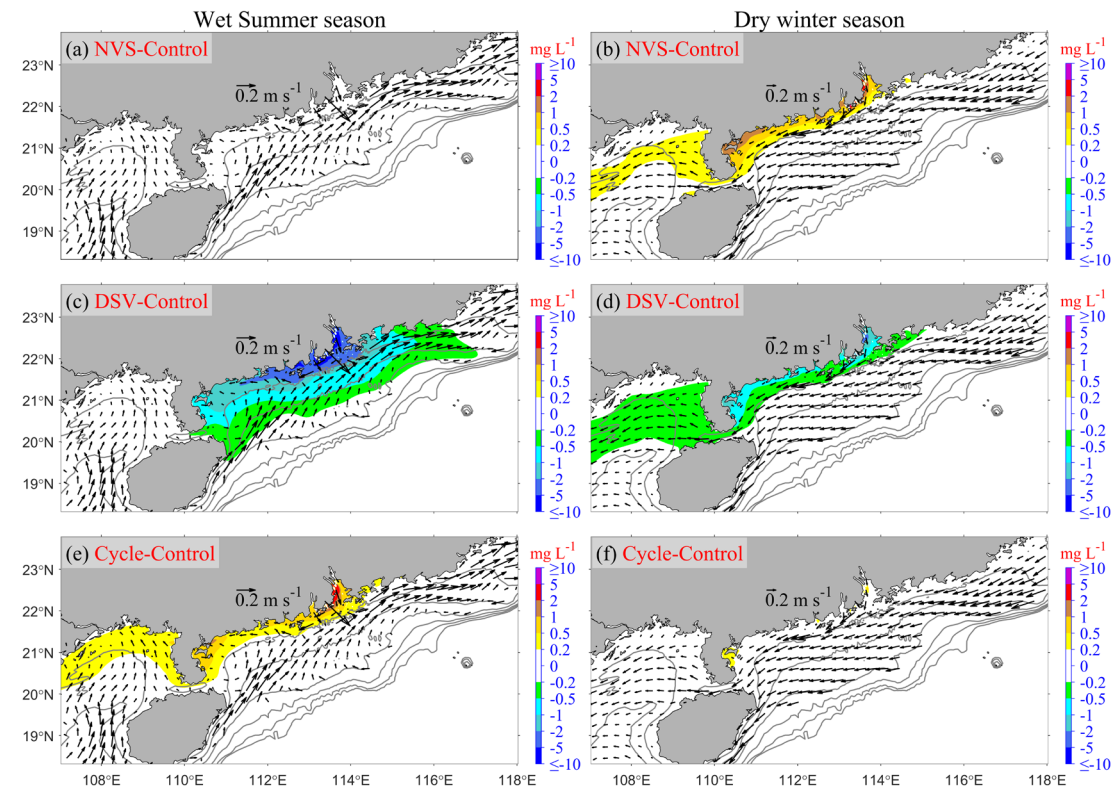


**Figure 10.** Same as Figure 9, but for the latter three experiments (NVS, DSV, Cycle). (a-b) NVS-Control, (c-d) DSV-Control, and (e-f) Cycle-Control.



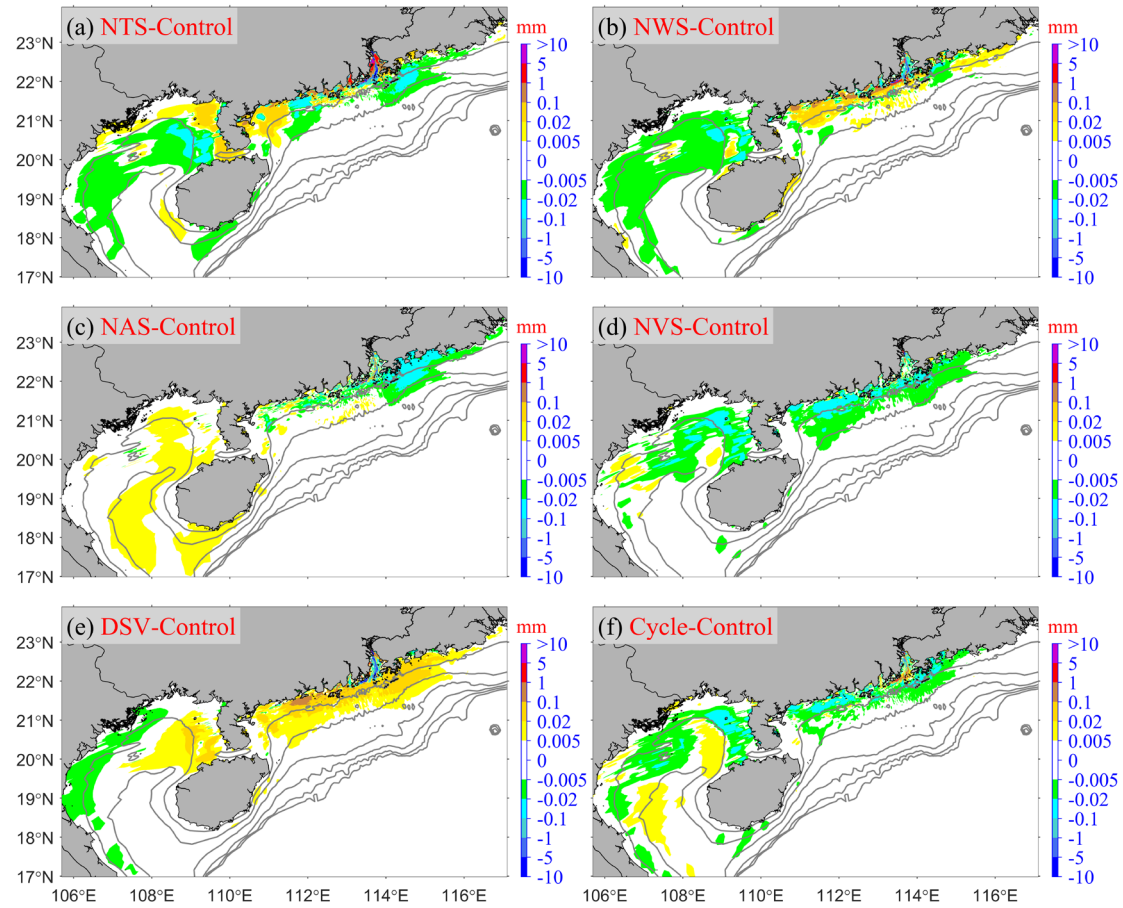


**Figure 11.** The differences in annual deposition between the Control run and the following cases: (a) NTS-Control, (b) NWS-Control, (c) NAS-Control, (d) NVS-Control, (e) DSV-Control, and (f) Cycle-Control.

Finally, we analyze the impact of various factors on the annual riverine sediment retention budget across different regions. Specifically, Figure 12 illustrates the annual riverine sediment retention budget in various regions under six sensitivity simulations, namely Exp 2-7 (including NTS, NWS, NAS, NVS, DSV, and Cycle). It should be noted that the retention percentages budget and their variations discussed hereinafter are all relative to the annual riverine sediment load.

As shown in Figure 12, tides and sediment settling velocity have the most significant impact on the retention in the "Proximal" region. In the NTS case and the DSV case, the retention in the "Proximal" region is 70.92% and 71.57%, respectively (Figures 12a and 12e), which is higher than 66.45% in the Control run (Figure 7c). This indicates that ignoring tides will cause the PRE to capture more riverine sediments, and a larger settling velocity will result in more riverine sediments being retained within the PRE. In these two cases, compared with the Control run, the retention in the "Gulf" and "Distal" regions decreases. Meanwhile, the DSV case causes the greatest increase in retention in the "Western" region, with an increase of +1.91%.

Furthermore, the NWS also leads to a 2.2% increase in retention in the "Proximal" region (Figure 12b), which is lower than that in the NTS case. This shows that tides dominate resuspension versus deposition in the estuary more than waves do. However, for the "Western" region on the shelf west of the PRE, compared with the NTS case, the NWS causes a greater increase in retention, indicating that waves dominate the resuspension of Pearl River-derived sediments in these nearshore areas more than tides do.

For the shelf east of the PRE (i.e., the "Eastern" and "Southeastern" regions), NAS brings about the most dramatic changes. In the absence of ambient shelf currents and residual water levels, the retention of Pearl River-derived sediments in these regions drops from 9.1% to 0.84% (Figure 12c). Meanwhile, ignoring these background circulations results in a substantial overestimation of the retention in the

"Distal" region, with an increase of 6.49%.

In the NVS case, where the winter and summer critical shear stress for erosion are set to be identical, ignoring the fact that the critical erosion stress in winter should be higher than that in summer leads to a decrease in the retention of Pearl River-derived sediments on the shelf east of the Leizhou Peninsula and Hainan Island. The reduction ranges from -0.05% to -0.85% (Figure 12d), which in turn causes the retention in the "Gulf" and "Distal" regions to increase by 0.7% and 1.47%, respectively. Overall, compared with scenarios that ignore physical processes and alter sediment settling velocity (NTS, NWS, NAS, and DSV), the NVS scenario, which does not take into account the seasonal variation of critical shear stress for erosion, has a relatively smaller impact on the retention of Pearl River-derived sediments.

Finally, in the Cycle case, the end state of the Control run is used as the initial conditions, and a second control simulation is performed. To isolate the pre-existing Pearl River-derived sediments, the initial retentions (the end conditions of the Control run on March 31, 2018) are subtracted before calculating the retention in the Cycle case (Figure 12f). In the Cycle case, the retention of Pearl River-derived sediments on the shelf east of the Leizhou Peninsula and Hainan Island shows little variation, with values ranging from -0.98% to +0.24% (Figure 12f). The most significant changes are the decreases and increases in retention in the "Gulf" and "Distal" regions, which are -2.17% and +3.54%, respectively, compared to the Control run. This demonstrates the long-term trend of southwestward transport of Pearl River-derived sediments on the shelf (relative to the Control run).

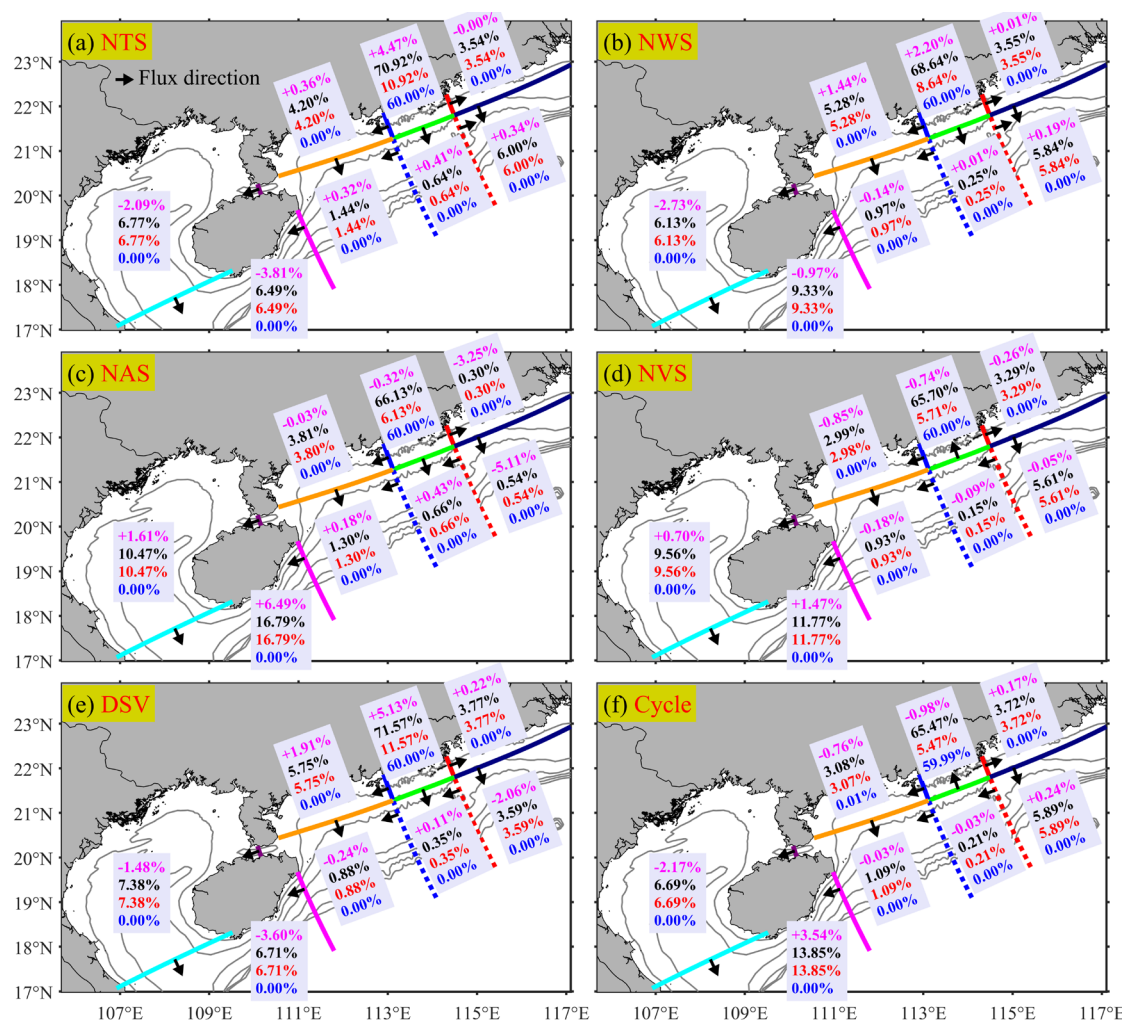


**Figure 12.** Same as Figure 7c, but for the other six cases: (a) NTS, (b) NWS, (c) NAS, (d) NVS, (e) DSV, and (f) Cycle, respectively. The magenta percentage values indicate the retention percentage budget differences between the Control run and the sensitivity cases.

In order to show the impact of winds and waves on the distribution of river plume and riverine sediment dispersal in a typical year, this section shows the results of two cases: Wind and wave (Figure 7) and No wind or wave (Figure 8).

In Wind and wave case, given the prevailing northeasterly wind stress throughout

the year (Figure 7b), a significant portion of the river plume expands westward (Figure 7a). Similar to the expansion pattern of the river plume, the distribution of riverine suspended sediment is more concentrated near the estuary, with higher concentrations observed on the west side outside the estuary compared to the east side (Figure 7b). Horizontal transport of riverine suspended sediment outside the estuary involves both eastward and westward transport, with westward transport dominating and exhibiting a structure similar to that of winter transport (Figure 7c vs Figure 6c). Meanwhile, eastward transport follows a path similar to the eastern branch of the PRE plume observed during summer (Figure 7c vs Figure 5c). Consequently, Pearl River sediments are predominantly deposited near the estuary and in shallower water areas (water depth <40 m) on the east and west sides of the estuary (Figure 7d). Additionally, some riverine sediments are deposited in the Beibu Gulf area.

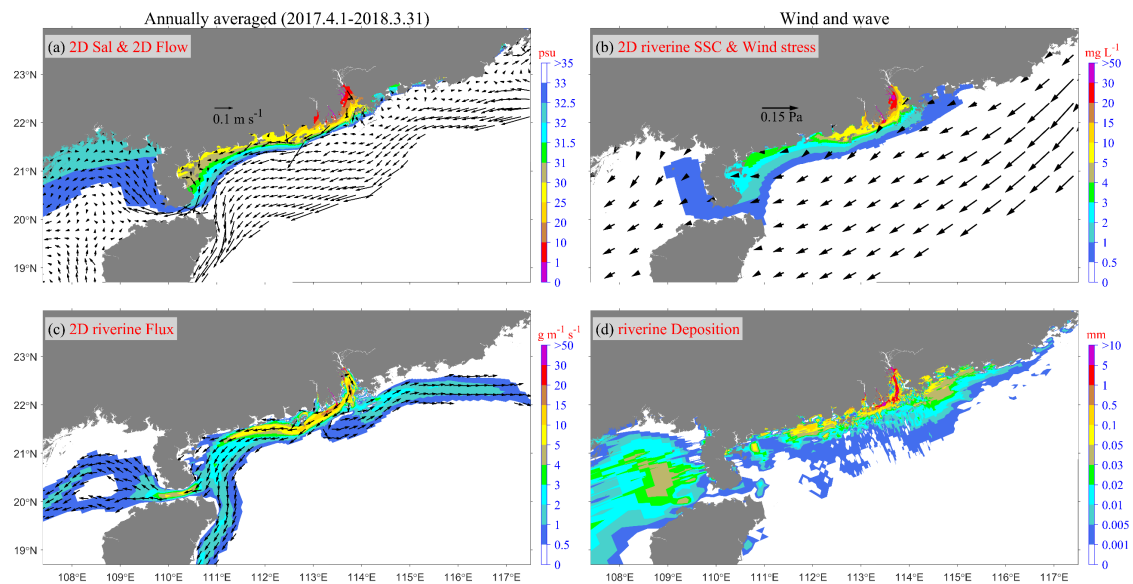


**Figure 7.** Same as Figure 5, but showcases the annual averaged patterns spanning from April 1st, 2017, to March 31st, 2018 in Wind and wave case.

In No wind or wave case, the river plume, characterized by a wider cross-shore width, primarily spreads toward the open sea due to the lack of wind and wave mixing (Figure 8a). This leads to pronounced stratification of the water column in the plume area. While riverine suspended sediment concentrations are higher near the estuary (Figure 8b), riverine sediment is transported from the estuary outward and towards both the east and west sides, with the magnitude of eastward transport exceeding that of westward transport (Figure 8c). Riverine sediment deposition thickness in the estuary and near the mouth bar is relatively higher (Figure 8d), and the majority of riverine sediment transported outside the estuary gets deposited on the shelf not far from the estuary (water depth  $< 60$  m).

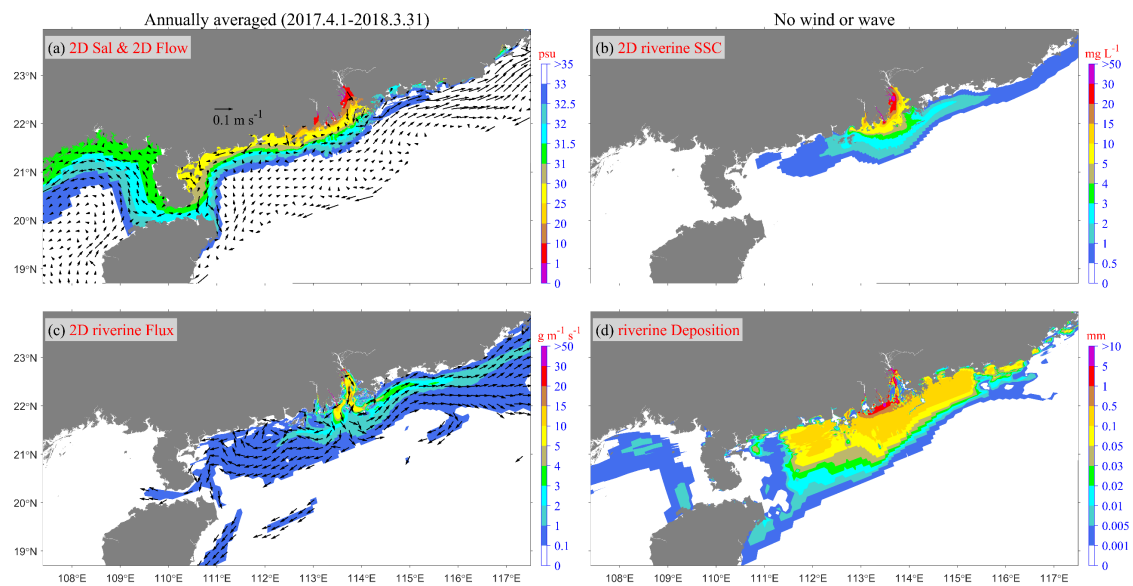


**Figure 8.** Same as Figure 7, but illustrates the annual averaged patterns under the condition of No wind or wave case.

In order to visually discern the vertical differences in hydrodynamics and sediment dynamics between the two scenarios, we examined the annually averaged

conditions along the solid line section of the West transect shown in Figure 1a (Figures. 9-10). This transect is located precisely in the vicinity of the western outer side of the estuary, where westward transport is a fundamental characteristic in realistic conditions (Wind and wave case). The situations of this transect under both cases (Case 1 and 2) can effectively reflect the differences in hydrodynamics and sediment suspension, transport, and deposition processes.

In No wind or wave case, the river plume mainly concentrates in the surface layer of the water column (Figure 9a-b). The area where the river plume occupies has a water level about 2 cm higher than offshore (Figure 9a). There is a significant difference between surface and bottom salinity (Figure 9b), reaching 15 psu, resulting in a high buoyancy frequency (Figure 9f). The eddy viscosity and turbulent kinetic energy (TKE) are relatively low, with slightly higher values at the bottom and near the outer edge of the river plume (Figure 9e, g). Suspension and westward transport flux of riverine sediment primarily occurs in the nearshore and recirculation areas of the river plume bulge (Figure 9a-d), with lower concentrations offshore (Figure 9d). Due to the bottom shear stress generally being less than 0.1 Pa, with an average of 0.04 Pa, a large amount of sediment deposits across the entire transect, with an average of 0.16 mm (Figure 9h).



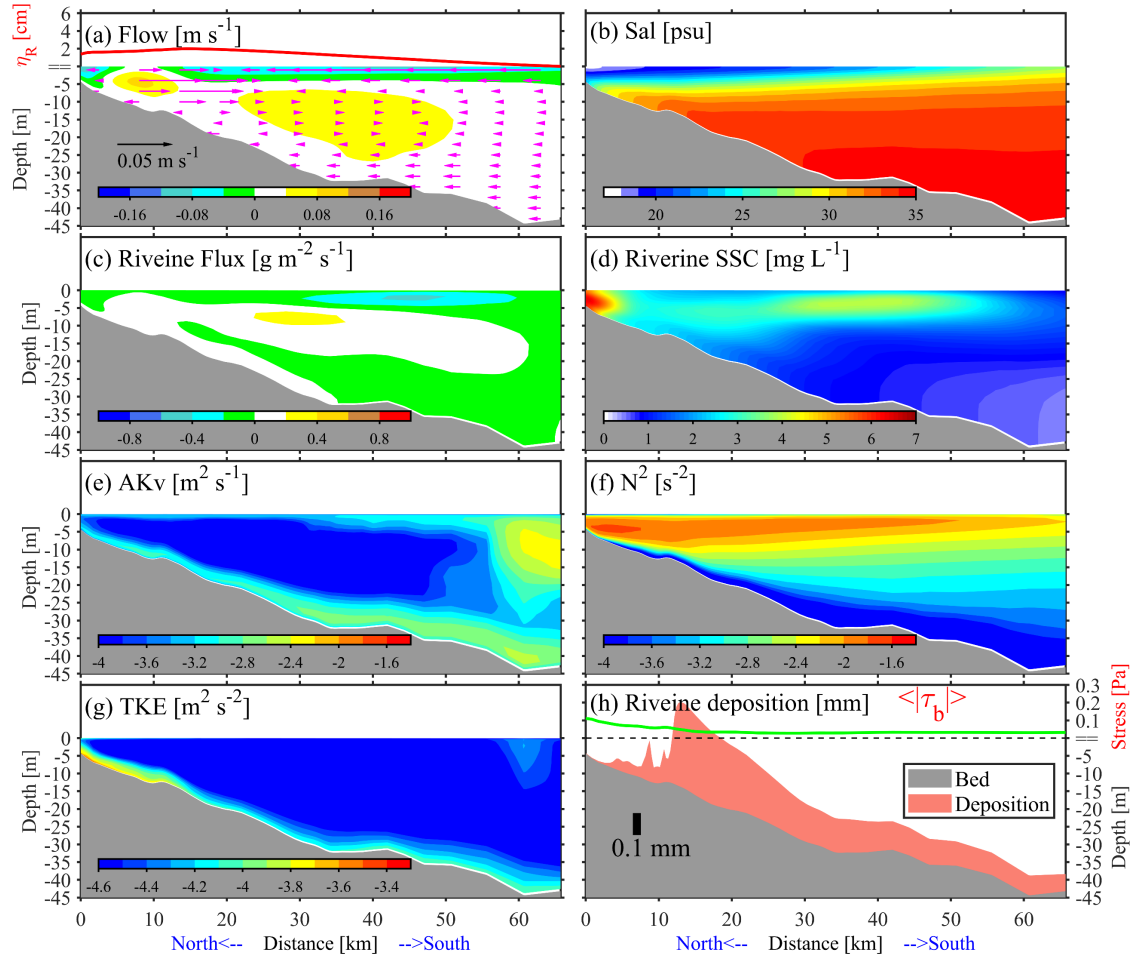


**Figure 9.** Annually averaged patterns at the solid part of the West transect in No wind or wave scenario. (a) alongshore (color), cross-shore (vector) direction velocity and relative sea level height (red solid line), (b) salinity, (c) axial riverine sediment flux, (d) riverine SSC, (e) logarithm of vertical viscosity coefficient ( $AK_v$ ), (f) logarithm of buoyancy frequency, (g) logarithm of turbulent kinetic energy (TKE), (h) riverine sediment deposition thickness and bottom stress magnitude (green solid line) at the seabed.

In Wind and wave case, the river plume extends offshore throughout the entire water column (Figure 10a-b). The wind causes the water level to elevate by 5 cm close to the coast compared to offshore areas, with a significant increase in westward



surface flow velocity, much greater than under No wind or wave case (Figure 10a). The difference between surface and bottom salinity decreases to 7 psu, reducing the buoyancy frequency but increasing the horizontal salinity gradient across the shore (Figure 10b, f). Eddy viscosity increases significantly, especially in areas with higher salinity (Figure 10e). TKE also increases substantially, particularly in the surface layer affected by winds and waves and nearshore bottom layers affected by waves (Figure 10g). Suspension of riverine sediment is more pronounced in nearshore areas, with increased concentration, while concentrations decrease offshore (Figure 10d). The flux of riverine sediment transport towards the west significantly increases, primarily occurring in areas where westward flow intensifies (Figure 10c, a). Due to the overall increase in bottom shear stress, with an average of 0.11 Pa, sediment deposition thickness decreases dramatically to one-tenth of that under No wind or wave case (Figure 10h).

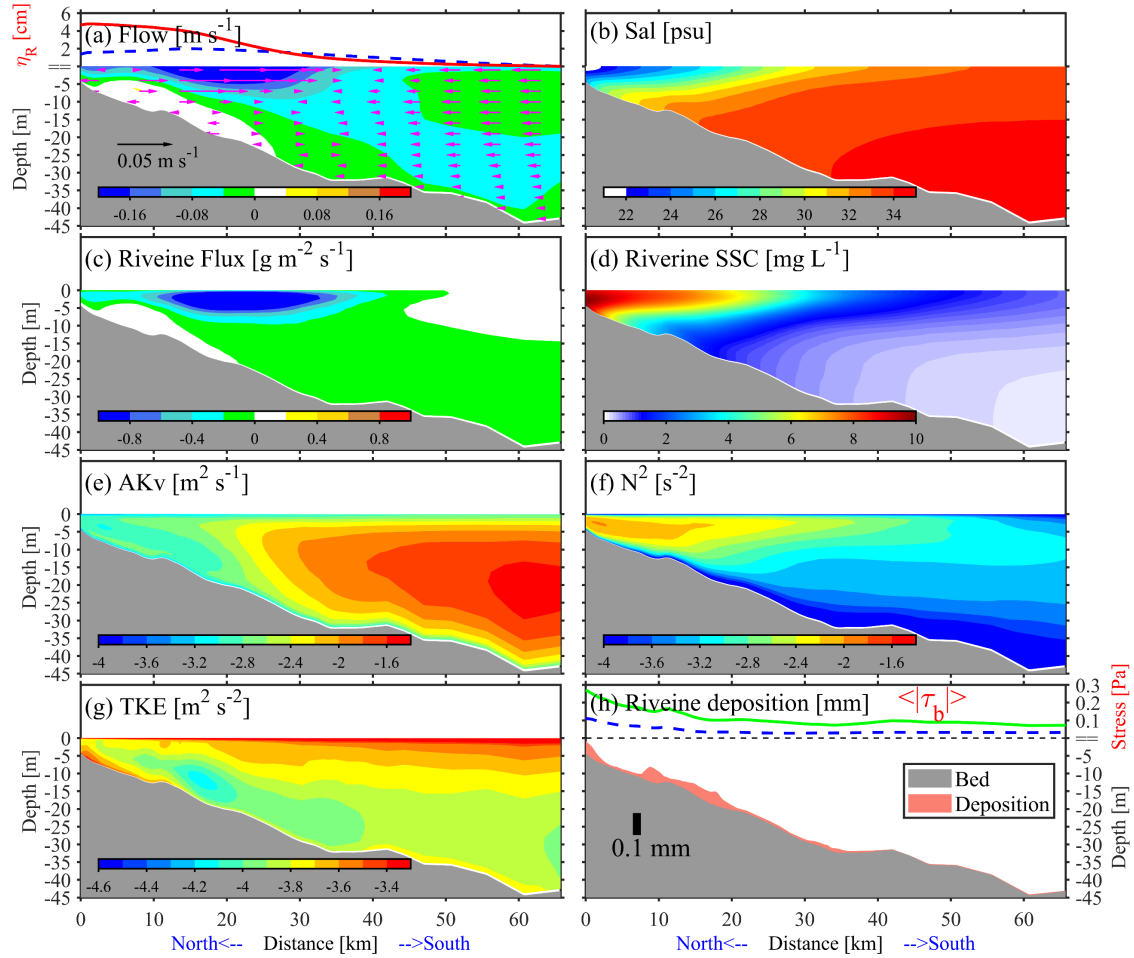


**Figure 10.** Same as Figure 9, but for the Wind and wave scenario. Note the blue dashed lines in (a) and (h) represent the relative sea level height and bottom stress magnitude in the No wind or wave scenario, respectively.

#### 4.4 Riverine sediment Budget over the shelf with/without wind and wave effects

To improve the understanding of the spatial-temporal differentiation of riverine sediment dispersal, and the estimation of the fate of the Pearl River sediment during the wet summer season and throughout the year, we partitioned the model domain into eight distinct regions delineated by various transects as illustrated in Figure 1a. The division criteria are mainly based on the distance from the estuary and the natural

separation by peninsulas and islands. These areas include:—

- ① Near region: Proximity to the estuary,—
- ② Eastern region: Eastern side of the estuary, closer to the shoreline,—
- ③ Southeastern region: Further offshore on the eastern side of the estuary,—
- ④ Southern region: Located deeper in the southern part of the estuary,—
- ⑤ Western region: Western side of the estuary, closer to the shoreline,—
- ⑥ Southwestern region: Offshore on the western side of the estuary,—
- ⑦ Gulf region: Mainly the Beibu Gulf,—
- ⑧ Far-off region: South of the Hainan Island.

By dividing the model domain into these delineated regions, we calculated the riverine sediment flux for each transect, thereby determining the total riverine sediment volume in each region. The riverine sediment flux data for different scenarios are presented in Table 3. Additionally, Figure 11 illustrates the proportion of riverine sediment retained within each region relative to the total river sediment input for the specific wet summer season or the whole year under two simulation cases.

1087

1088

1089

1090

~~Table 3. Time and depth-integrated riverine sediment flux at the transects during different periods in two cases. (Unit:  $\times 10^4$  tons). Riverine sediment refers to the combined total of 'Clay (river)' and 'Silt (river)' as presented in Table 1.~~

Transect ID	Case ID	Wet summer	Dry winter	Yearlong
West solid	WW	-648.94	-292.09	-941.02
	NWW	-131.49	-51.50	-182.99
West dashed	WW	58.79	-136.67	-77.88
	NWW	-41.66	-105.21	-146.86
East solid	WW	470.24	-114.42	355.81
	NWW	410.99	41.04	452.04
East dashed	WW	12.91	-95.89	-82.98
	NWW	58.57	-9.73	48.84
South	WW	1.61	-2.83	-1.23
	NWW	-186.89	-46.98	-233.87
Shore	WW	-237.45	4.44	-233.01
	NWW	22.18	-53.90	-31.73
Coast	WW	-318.02	-503.84	-821.86
	NWW	0.27	12.32	12.59
Southwest	WW	-64.02	-351.33	-415.34
	NWW	-1.52	-44.87	-46.39
Strait	WW	-28.94	-419.36	-448.30
	NWW	-5.95	-18.53	-24.48
Bay	WW	4.82	-66.36	-61.54
	NWW	0.02	1.47	1.49

1091

~~WW refers to Wind and wave, and NWW refers to No wind or wave.~~

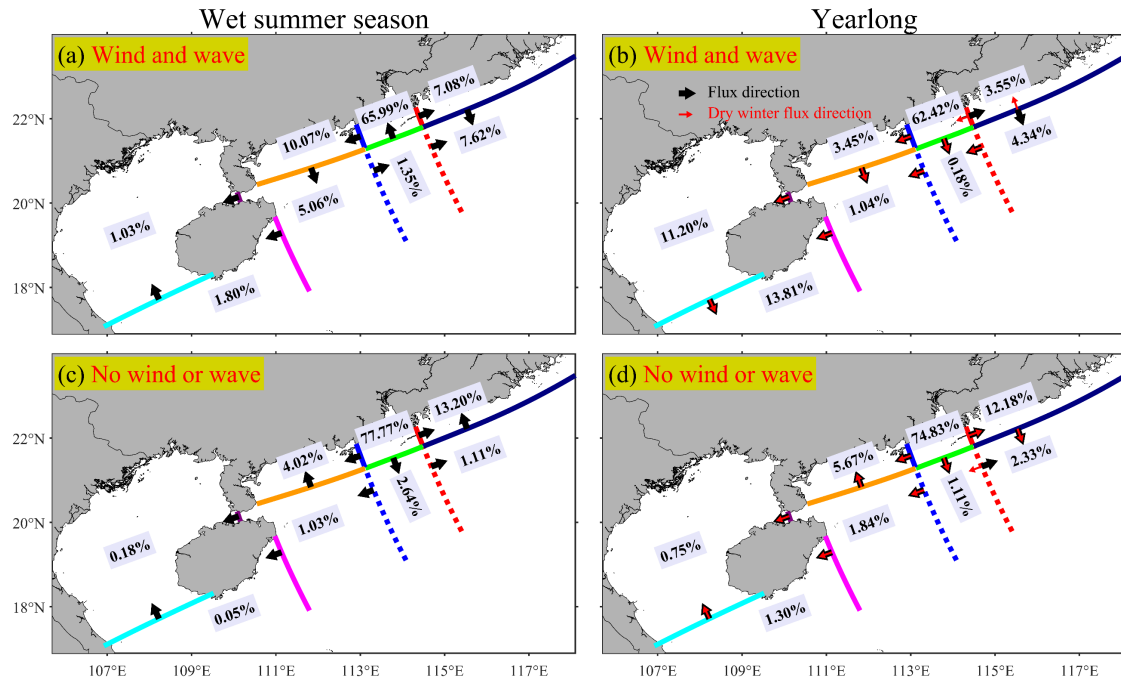


**Figure 11.** Riverine sediment retention at eight regions during the wet summer season (Column 1) and throughout the year (Column 2) across the Wind and wave case (Row 1) and No wind or wave case (Row 2). The arrows show the directions of riverine sediment flux at each transect during the specific period.

Combining the data from Table 3 with the results provided by Figure 11, it becomes apparent that the fate of Pearl River-derived sediment is intricately influenced by the presence or absence of winds and waves, as well as seasonal variations.

However, irrespective of Wind and wave conditions or seasonal changes, a predominant portion of riverine sediment is consistently retained within the "Near" region, proximal to the estuary, accounting for a substantial proportion ranging from 62.42% to 77.77% (Figure 11a-d).

~~In Wind and wave case, particularly in summer, the bulk of riverine sediment is transported onto the continental shelf east of the Qiongzhou Strait (Figure 11a). However, only a negligible fraction (2.83%) reaches the Beibu Gulf or the area south of Hainan Island. Interestingly, the quantity transported eastward (14.7%) is surpassed by the total amount transported westward (17.96%). Furthermore, the offshore area on the western side of the estuary retains a larger proportion (10.07%) of riverine sediment compared to the eastern side (7.08%).~~

~~A significant portion of the riverine sediment transported eastward is concentrated in the "Southeastern" region, attributable to the obstructive effect of the upwelling plume front near shoals in eastern Guangdong and Taiwan Island during summer months (Chen et al., 2017a; Chen et al., 2017b). The encounter between river plume and upwelling results in the formation of a highly intense density front, generating strong jets along the front due to the thermal wind effect (Chen et al., 2017b; Chen et al., 2019).~~

~~In contrast, the winter season features strong northeasterly winds and strong waves, which significantly impact sediment dynamics across all six regions east of the Qiongzhou Strait (Figure 11b). Consequently, there is a marked increase in sediment retention within the "Gulf" and "Far-off" regions. These regions receive a combined total of 25% of the annual sediment input over the course of the year.~~

~~Notably, despite the occurrence of significant resuspension of riverine sediment within the "Near" region, minimal overall loss is observed. This phenomenon is attributed to the complex network of islands and coastlines present in the area. The~~

intricate geography effectively traps the majority of the resuspended sediments behind islands or within the bay, preventing significant loss. Additionally, the "Near" region receives riverine sediment sourced from the adjacent "Eastern" region, further contributing to sediment retention within the area.

In No wind or wave case, water mixing is weakened, resulting in distinctive patterns of riverine sediment transport (Figure 11c-d). During the wet summer season, the substantial Pearl River freshwater discharge and riverine sediment load lead to a significant transport of riverine sediment, predominantly in a southward offshore direction (Figure 11c). Notably, the amount of riverine sediment transporting to the "Southern" region is doubled compared to the Wind and wave scenario, accounting for 2.64% of the total sediment load. Conversely, only 5.28% of sediment is transported westward of the estuary due to reduced bottom shear stress and westward currents in No wind or wave case.

Most of the riverine sediment tends to deposit near the estuary, with sediment deposited on the seabed exhibiting low susceptibility to resuspension. The exclusion of southeasterly winds during wet summer leads to a drastic decrease of more than two-thirds in westward sediment flux, with only a minimal fraction (0.23%) reaching the Beibu Gulf or the area south of Hainan Island. However, the eastward transport of riverine sediment experiences only a slight decrease to 14.31%, predominantly concentrated in the nearshore area due to reduced blocking effects caused by the exclusion of the summer monsoon and decreased upwelling.

Transitioning into the dry winter season, both the Pearl River freshwater

discharge and riverine sediment load decrease significantly, resulting in a reduction in the expansion range of the river plume. Furthermore, decreased shortwave radiation contributes to increased water mixing. Tidal effects in the "Near" region lead to the export of sediment to regions beyond its immediate vicinity, while strong tidal currents in the "Eastern" region facilitate the offshore transport of sediment to the "Southeastern" region (Figure 11d). Additionally, more riverine sediment is transported to the "Gulf" and "Far off" regions during this period compared to the wet summer season when the downwelling favorable winds are shut down.

## **4.5. Discussions**

### **5.1 Mechanisms of Wind and Wave Effects on Hydro- and Riverine Sediment Dynamics**

The suspension, transport, and deposition of the Pearl River sediment over the shelf are subject to changes associated with wind and wave effects (Figure 7-8), which have not been well addressed in previous research.

In No wind or wave case, the surface river plume can be swiftly transported outward from the estuary over long distances, but the riverine sediment primarily deposits in the nearby estuarine areas (Figure 8). When the wind and wave effects are present, the eastward transport of the plume diminishes, while the westward flow velocity increases (Figure 7). Correspondingly, riverine sediment transport towards the east decreases, while riverine sediment transport towards the west increases (Figure 7c vs Figure 8c). Riverine sediment deposition near the estuary decreases, while deposition in the Beibu Gulf significantly increases (Figure 7d vs Figure 8d).



This section analyzes the mechanisms of the riverine sediment dispersal from the perspectives of hydrodynamics and sediment dynamics (Figure 12 and 13).

It is evident that different paths of river plume movement correspond to Wind and wave and No wind or wave cases. Therefore, further momentum balance analysis of plume on these fast-moving paths is necessary, representing the force balance of movement under different scenarios. In the COAWST model, omitting the small vertical advection and horizontal viscosity, the momentum equation in the cross shore direction (the Y-axis direction as showed in Figure 1b) is given by (Warner et al., 2008),

$$\underbrace{\frac{\partial v}{\partial t}}_{\text{ACC}} = - \underbrace{\frac{1}{\rho} \frac{\partial p}{\partial y}}_{\text{PGF}} - \underbrace{fu}_{\text{COR}} - \underbrace{\left( u \frac{\partial v}{\partial x} + v \frac{\partial v}{\partial y} \right)}_{\text{HADV}} + \underbrace{\frac{\partial}{\partial z} \left( A k v \frac{\partial v}{\partial z} \right)}_{\text{VVSIC}} + \underbrace{WT}_{\text{wave-induced}} \quad (2)$$

where  $u$  and  $v$  are the velocities in the X-axis (alongshore) and Y-axis direction, respectively;  $\rho$  is the sea water density;  $f$  is the Coriolis parameter; and  $Akv$  is the vertical eddy viscosity. The terms from left to right denote the acceleration (ACC), pressure gradient (PGF), Coriolis force (COR), horizontal advection (HADV), vertical mixing (VVSIC, surface stress SSTR, and bottom stress BSTR terms when in two dimensions), and wave induced forces (i.e., wave breaking and roller force, horizontal vortex force and Coriolis Stokes force terms). The momentum terms are averaged in 365 days to see the yearlong mean pattern.

In No wind or wave case, the annually averaged currents on the eastern side of

the PRE primarily experience the COR and PGF in the cross-shore direction, with the remaining terms being minor and not shown (Figure 12a, c). The PGF is directed shoreward, while the COR is directed seaward, resulting in a geostrophic balance. Significant water level gradients at the surface correspond to a strong eastward geostrophic flow ( $u_g = -gf^{-1}\partial\eta/\partial y$ ), consistent with the annual average eastward flow field (Figure 12e and Supplement Figure S4o). The eastward flow is mainly driven by the thermal wind effect ( $\partial u/\partial z = g\rho_0^{-1}f^{-1}\partial\rho/\partial y$ , where  $g$ ,  $\rho$ , and  $\rho_0$  are the acceleration of gravity, the seawater density, and averaged seawater density, respectively), as river plume encounters upwelling, forming a strong density front with notable vertical velocity shear (Figure 12g). In the region south of the plume upwelling front, vertical velocity shear supports westward plume movement or dampens its eastward velocity.

In Wind and wave case, on one hand, the onshore Ekman transport ( $-\rho_0^{-1}f^{-1}\tau_x$ ,  $\tau_x$  is the wind stress in the alongshore direction) due to annually averaged northeasterly winds leads to an increase in nearshore water levels on the western side of PRE, causing the currents to tend towards the west, forming geostrophic currents (Figure 12f). On the other hand, northeast winds generate westward wind stress, resulting in westward wind-driven currents (Figure 7a). Additionally, density fronts south of the plume can create strong westward vertical velocity shear (Figure 12h). These factors contribute to the rapid westward movement of the plume. After the adjustment of water levels, the surface geostrophic currents approximate geostrophic balance in the cross-shore direction (Figure 12b and d).

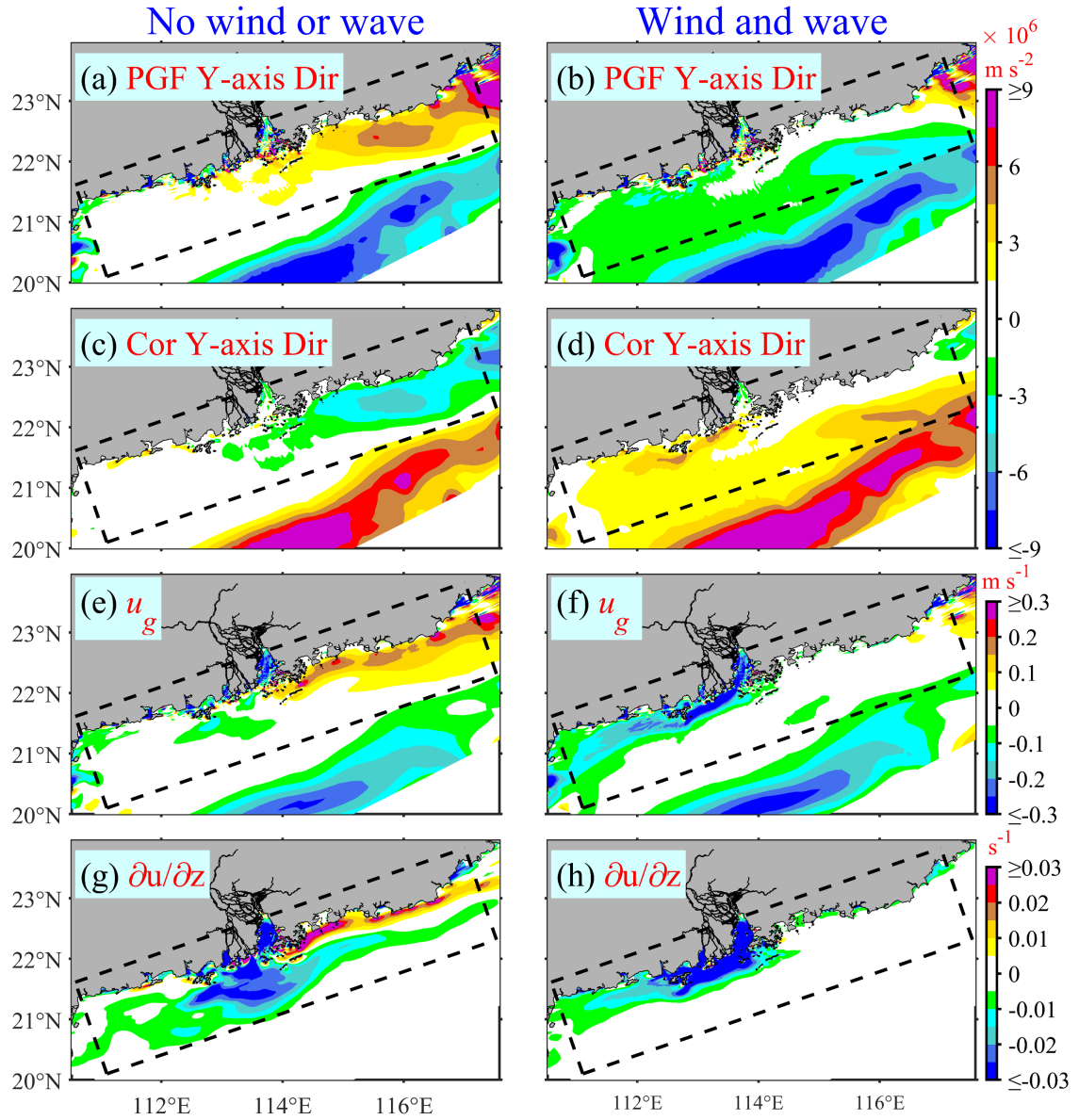


**Figure 12.** (a-b) Pressure gradient term in the Y-axis direction, (c-d) Coriolis force term in the Y-axis direction, (e-f) geostrophic velocity in the X-axis direction derived from the geostrophic balance equation, (g-h) vertical velocity shear at surface layer in the X-axis direction derived from the thermal wind equation. No Wind or wave (Column 1) and Wind and wave (Column 2) scenario, respectively.

The preceding analysis involves the dynamic mechanisms governing plume

spreading paths under both Wind and wave and No wind or wave cases. Now, we turn to analyze the riverine sediment transport mechanisms under varying dynamic conditions. To accomplish this, we examined the annual and depth-averaged sediment transport terms under two scenarios. By excluding minor vertical advection and diffusion factors, the sediment transport equation (Warner et al., 2008) can be represented as follows:

$$\underbrace{\frac{\partial C}{\partial t}}_{\text{Rate}} = \underbrace{-\frac{\partial uC}{\partial x} - \frac{\partial vC}{\partial y}}_{\text{HADV of SSC}} - \underbrace{\frac{\partial w_s C}{\partial z}}_{\text{Settling}} + \underbrace{E_0 (1 - \phi) \max\left(\frac{\tau_b - \tau_{ce}}{\tau_{ce}}, 0\right)}_{\text{Resuspension}} \quad (3)$$

where  $C$  represents the SSC;  $w_s$  is the settling velocity (positive upwards);  $E_0$  indicates a bed erodibility parameter ( $\text{kg m}^{-2} \text{s}^{-1}$ );  $\phi$  is the porosity (volume of voids/total volume) of the top bed layer;  $\tau_b$  and  $\tau_{ce}$  are the bottom shear stress and critical shear stress for erosion, respectively. The terms from left to right denote the rate of change in SSC (rate), the lateral sediment advection (HADV of SSC), vertical settling (Settling), and the bottom erosion (Resuspension), respectively.

In No wind or wave case, riverine sediment is transported horizontally to the outer region of the PRE and distributed to both the east and west sides of the PRE (Figure 8c and 13a), thereby increasing the riverine SSC outside the estuary (Figure 8b). These riverine sediments continuously deposit on the seabed during transportation (Figure 8d and 13b), while resuspension primarily occurs in areas with strong tidal currents and high bottom shear stress, such as the PRE, the north side of the Taiwan Bank, and near the Leizhou Peninsula (Figure 13c). Consequently, net

deposition (Settling + Resuspension) primarily occurs in shallow areas close to the PRE where bottom shear stress is low (Figure 8d, Supplement Figure S4m, and Figure 13d), while suspension dominates in areas with high shear stress.

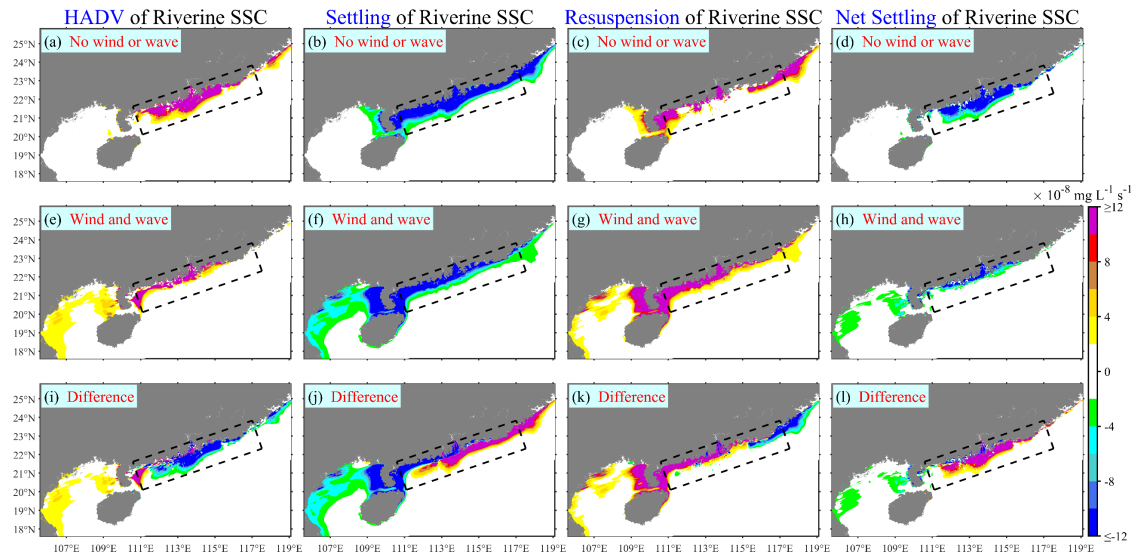


**Figure 13.** Annually averaged patterns of riverine SSC diagnostic term (a, e, i) horizontal total advection, (b, f, j) vertical settling, (b, f, j) resuspension, (b, f, j) net settling calculated by vertical settling in addition to resuspension. No Wind or wave (Row 1), Wind and wave (Row 2) scenario, and the difference between them (Wind and wave minus No Wind or wave, Row 3), respectively.

In Wind and wave case, riverine sediment mainly transports westward after exiting the PRE (Figure 7e and Figure 13e), with significantly reduced net transport fluxes towards the east and south. Meanwhile, the bottom shear stress increases on both the east and west sides adjacent to the PRE (Supplement Figure S4m-n), leading to increased resuspension. In regions further north of the Taiwan Bank, sediment deposition and resuspension decrease due to reduced transport of riverine sediment to these areas (Figure 13g, k). Eventually, resuspension significantly increases in most

1262 ~~areas east of the Leizhou Peninsula, accompanied by a substantial decrease in~~  
1263 ~~sediment deposition thickness (Figure 7d and Figure 13l). Most of the riverine~~  
1264 ~~sediment due to reduced retention is transported to the sides of the Leizhou Peninsula~~  
1265 ~~and the Beibu Gulf (Figure 7d and Figure 13l).~~

1266 ~~Overall, wind and wave dynamics are pivotal in shaping coastal hydrodynamics~~  
1267 ~~and riverine sediment dispersal patterns. Wind significantly influences flow, while~~  
1268 ~~waves notably affect resuspension. Together, they impact riverine sediment transport~~  
1269 ~~and deposition on the continental shelf of the northern South China Sea.~~

#### 1270 **4.1 Fidelity of our model results**

1271 We simulated the suspension, transport, and deposition of Pearl River-derived  
1272 sediment over the shelf from April 2017 to March 2018. Comparisons with multiple  
1273 types of observations demonstrated that the model simulation reasonably well  
1274 captured the regional patterns and temporal variability of water levels (Figures S2-S4),  
1275 surface waves (Figures S5-S6), estuarine and shelf currents (Figures S8a-b and  
1276 S9-S10), salinity and temperature (Figures S7a-b and S8c-d), and SSC (Figures S7c  
1277 and S8e-f). Even though we have made substantial efforts to collect observational data  
1278 and conduct calibration and validation, the large scope of the study area and the fact  
1279 that the study covers an entire year mean that there are some inherent challenges to  
1280 achieving a complete analysis. The real-world situation may be extremely complex,  
1281 and these validations may still not be sufficient to address all issues (such as the  
1282 accurate parameterization of sediment characteristics and their seasonal variations, as  
1283 well as the proportion of slow-settling fine grains and flocculated materials in riverine  
1284 sediments). Therefore, in this section, we intend to discuss the fidelity of our results.

1285 Firstly, according to previous observations, laboratory experiments, and  
1286 numerical sensitivity analyses, it has been demonstrated that the critical shear stress  
1287 for erosion of sediments in the PRE is higher in winter than in summer (Dong et al.,  
1288 2020;Cao et al., 2025). Therefore, we considered the seasonal variation of critical  
1289 shear stress for erosion in a suite of model experiments, that is, increasing the critical  
1290 shear stress for erosion in winter. This setting was also applied during the 15-month  
1291 spin-up before conducting the model experiments (the driving force of the spin-up is  
1292 realistic, i.e., the settings are consistent with those of the Control run). After realistic  
1293 reworking during the spin-up, the bed sediment grain size distribution (used as initial  
1294 conditions in the Control run and all Sensitivity cases except the Cycle case) is quite  
1295 close to the initial prototype (Figures 2d-f vs. 2g-i) compared to our previous spin-up  
1296 (not presented in this version; however, it can be referred to in our initially submitted  
1297 preprint and Supplement), which did not consider such temporal variability.

1298 When the seasonal variation of critical shear stress for erosion is not considered,  
1299 the results of the NVS case indicate that such a setting underestimates the retention of  
1300 Pearl River-derived sediments on the shelf east of the Leizhou Peninsula and Hainan  
1301 Island during winter, while overestimating the retention in the "Gulf" and "Distal"  
1302 regions. Even so, these estimation errors are relatively minor compared to the annual  
1303 load (Figure 12d). Consequently, the consideration of the seasonal variation of critical  
1304 shear stress for erosion has a relatively small impact on the annual retention. Instead,  
1305 it has a more significant effect on the bed sediment grain size distribution at the  
1306 bottom.

Furthermore, although the initial bed sediment grain size distribution we obtained by considering the seasonal variation of critical shear stress for erosion is quite close to the initial prototype, there are still some differences (Figures 2d-f vs. 2g-i). Additionally, the lack of in situ grain size distributions in part of the model domain (especially in the Beibu Gulf) may also introduce some uncertainties in sediment transport there. Does the variation in the proportion of bed sediment grain sizes have a significant impact on the model results? It should be noted that here we are not referring to the distribution proportion of riverine sediments on the bed. To address this question, we designed a new experiment (Cycle2). We used the end state of the Control run on March 31, 2018, as the initial conditions for Cycle2. However, different from the Cycle case, in Cycle2, we changed both Class 1 and Class 4 sediments in the bed and water column at the end state of the Control run to Class 1, and both Class 2 and Class 5 sediments to Class 2. That is, there were no pre-existing Pearl River-derived sediments in the model domain when Cycle2 started. The results of Cycle2 show that the retention in the "Proximal" and "Western" regions decreased by 0.13% and 0.03% of the annual riverine sediment load, respectively, while the retention in the "Eastern", "Southeastern", "Southern", "Southwestern", "Gulf", and "Distal" regions increased by 0.03%, 0.03%, 0.01%, 0.02%, 0.07%, and 0.01%, respectively. This indicates that the impact of this uncertainty in the proportion of bed sediment grain sizes is relatively small.

Choosing an appropriate settling velocity may be more important than the seasonal variation of critical shear stress for erosion. The results of the DSV case



show that a sediment settling velocity twice that of the Control run leads to the highest retention in the "Proximal" and "Western" regions across all experiments (Figure 12e), while reducing the retention in the "Distal" region. Although the settling velocity we adopted is based on previous studies (Xia et al., 2004; Ralston et al., 2012) and model calibrations (Figures S7c and S8e-f), with due consideration given to the presence of slow-settling single fine grains and high-settling flocs in riverine sediments, certain discrepancies might still exist in this setting. These discrepancies are contingent upon the actual magnitude of the low settling velocity of fine grains. In almost all cases, all flocs are retained in the "Proximal" region, and only in the Cycle case, flocs accounting for 0.01% of the annual load are retained in the "Western" region west of the "Proximal" region, indicating that high-settling flocs hardly leave the vicinity of the PRE. This finding shows close alignment with, yet exhibits minor distinctions from, the observed patterns in the Mekong Estuary (Xue et al., 2012). Xue et al. (2012) found that while the preponderance of flocs is deposited on the Mekong delta front precisely at the river mouth, a quantity equivalent to 1.6% of the annual riverine sediment load of flocs is deposited on the downdrift delta front further downstream from the river mouth. This is mainly because the estuary bay of the PRE is wider and there are numerous islands near the river mouth. The overwhelming majority of flocs are either deposited within the estuary bay or captured by the surrounding islands. In conclusion, our results are affected by the settling velocity of fine grains. More field observations and studies on model parameterization regarding the settling velocity of fine grains are urgently needed.

As previously noted, we classified riverine sediments into two categories based on established research: 40% slow-settling fine grains and 60% fast-settling flocs. This 40%/60% distribution is consistent with the setting from earlier studies (Zhang et al., 2019; Zhang et al., 2021), as summarized in Table 1. While such assumptions are necessary for modeling purposes, the actual composition of riverine sediments in natural environments remains uncertain. To evaluate the sensitivity of our results to this uncertainty, we conducted a conceptual analysis. If all riverine sediments were hypothetically composed entirely of fast-settling flocs, they would be completely retained near the source, with no transport to the Beibu Gulf. However, this scenario is inconsistent with the radionuclide measurements obtained from Beibu Gulf surface sediment samples (Lin et al., 2020). On the other hand, if all sediments were considered slow-settling fine grains, only 16.13% would be retained proximally under normal conditions (or 28.9% in the DSV case), a result that diverges significantly from established research. Chen et al. (2023) analyzed high-resolution seismic data and demonstrated that approximately 35% of the Pearl River-derived sediment has been transported to offshore shelf areas over the past 6,500 years, suggesting that 65% was deposited proximally. Our findings are in close agreement, indicating that 66.45% of the Pearl River sediments are retained in the proximal region, while 33.55% are transported elsewhere. This consistency with Chen et al. (2023) supports the validity of our approach. Taken together, these analyses confirm that the 40%/60% fraction assumption is a reasonable approximation for modeling purposes.

Furthermore, our model results demonstrate reasonable reliability in other aspects.

[Liu et al. \(2009\)](#) and [Ge et al. \(2014\)](#) using chirp sonar profiles from the inner shelf of the South China Sea combined with [Zong et al. \(2009\)](#)'s onshore borehole data, found that the thickness of Pearl River-derived sediments within the PRE since the Holocene is over 20 m, while the mud thickness in the shallow waters west of the Chuanshan Islands is approximately 5-10 m. Our calculated annual sediment thicknesses for these two regions are approximately 2 mm and 0.3 mm (Figure 7d), respectively. Given our model's annual riverine sediment load of 34.52 megatons—significantly reduced due to recent human activities ([Dai et al., 2008](#))—compared to the widely accepted Holocene average of around 90 megatons ([Liu et al., 2009](#)), we estimate the total sediment thickness over the past 7500 years to be roughly 39 meters and 6 meters for these depositional zones, consistent with previous studies ([Liu et al., 2009](#); [Zong et al., 2009](#)).

Furthermore, our results reveal that 8.86% of the riverine sediment derived from the Pearl River is transported to the Beibu Gulf (Figure 7c), primarily during the winter season (Figure 7b). This finding not only confirms the earlier speculation proposed by [Ge et al. \(2014\)](#) but also supplements the conclusions drawn by [Lin et al. \(2020\)](#). From a hydrodynamic perspective, [Shi et al. \(2002\)](#) found that the net flux of currents in the Qiongzhou Strait is westward throughout the year. Our results for both wet summer (Figures 5a-b) and dry winter currents (Figures 6a-b) in the Qiongzhou Strait are consistent with [Shi et al. \(2002\)](#). This westward flow contributes to the westward transport of Pearl River sediment to the Beibu Gulf.

## **~~5.2 Comparison with previous studies and implications for future~~**

## morphological evolution of the shelf

### 4.2 Implications of our model results

The fate of sediment dispersed from the river into the coastal ocean involves at least four processes: supply via plumes; initial deposition; resuspension and transport by marine processes; and long-term net accumulation ([Wright and Nittrouer, 1995](#)). In general, a significant proportion of river sediment tends to deposit in the estuary and its vicinity ([Walsh and Nittrouer, 2009](#); [Hanebuth et al., 2015](#)).

[Walsh and Nittrouer \(2009\)](#) present a hierarchical decision tree designed to predict the marine dispersal system at a river mouth based on fundamental oceanographic and morphological characteristics. Within this framework, the fate of riverine sediment deposition can be determined using key factors, ~~including such as~~ riverine sediment discharge ([greater or less than 2 megatons](#)), shelf width ([greater or less than 12 km](#)), and wave and tidal [range](#) conditions ([greater or less than 2 m](#)) ([Walsh and Nittrouer, 2009](#)).

We aim to analyze our PRE simulation results using the framework established by Walsh and Nittrouer (2009). Although the Pearl River's riverine sediment discharge ([Figure 2a](#)) exceeds [the Walsh and Nittrouer \(2009\)'s](#) 2 megatons per year [threshold](#), most of the sediment [still](#) remains deposited near the estuary ([Figure 7c](#)), indicating an estuarine accumulation-dominated [\(EAD\)](#) system, [unlike the hierarchical decision tree proposed by Walsh and Nittrouer \(2009\)](#). ~~This is likely due to a combination of factors, including the wide mouth of the estuary, large accommodation space of the estuary, the presence of numerous nearby islands, and~~

1417 ~~weak tidal forces. For the PRE, [Chen et al. \(2023\)](#) utilized high-resolution seismic data~~  
1418 ~~to discover that, since approximately 7.5 ka BP, only around 35% of the sediment~~  
1419 ~~derived from the Pearl River has dispersed to offshore shelf areas from the~~  
1420 ~~delta-estuary system. Our research indicates that the majority of Pearl River sediment~~  
1421 ~~deposits are near the PRE, with the remaining 38% being transported to other areas,~~  
1422 ~~which is consistent with the findings of [Chen et al. \(2023\)](#).~~ Outside the estuary, the  
1423 continental shelf, [spanning 200-220 km in width \(Liu et al., 2014\)](#), [significantly](#)  
1424 [exceeds](#) ~~extends well beyond the~~ [Walsh and Nittrouer \(2009\)'s](#) 12 km threshold ~~to~~  
1425 ~~over 100 km in width~~. As a result, most escaped riverine sediments tend to accumulate  
1426 on the shelf rather than being captured by submarine canyons [\(Figures 7c-d\)](#). This  
1427 wide, shallow shelf promotes sediment deposition and limits the direct transport of  
1428 fine sediments into deeper waters [\(Walsh and Nittrouer, 2009\)](#). [Subsequently, given](#)  
1429 [that the annual mean tidal range \(Chen et al., 2016; Gong et al., 2018b\) and Hsig](#)  
1430 [\(Figure 3d\) near the PRE are both below the 2 m threshold established by Walsh and](#)  
1431 [Nittrouer \(2009\), the majority of escaped riverine sediments are predominantly](#)  
1432 [deposited in the proximal depo-center.](#)

1433 [Our findings demonstrate that most of our outcomes are consistent with](#) ~~Unlike~~  
1434 the hierarchical decision tree proposed by [Walsh and Nittrouer \(2009\)](#), [except for the](#)  
1435 [application of the 2 megatons per year threshold for riverine sediment discharge. This](#)  
1436 [phenomenon can primarily be attributed to the unique geomorphological](#)  
1437 [characteristics of the PRE, including its broad mouth \(Figures 1 and S1\), extensive](#)  
1438 [accommodation space encompassing approximately 2385 km<sup>2</sup> of water area \(Wu et al.,](#)

2018), the presence and sheltering effect of numerous adjacent islands (Li et al., 2024b), and the division of fluvial sediment discharge through eight distinct outlets (Hu et al., 2011). ~~where sediment deposition can be categorized based on wave and tidal conditions, the PRE does not fit neatly into this framework. Whether deposition is dominated by proximal or distal processes cannot be fully determined by annually averaged waves and tides alone.~~

The monsoonal nature of the northern SCS (Figures 4a-b) induces pronounced seasonal variations in Pearl River-derived sediment transport and deposition (Figures 5 and 6). During the summer wet season, the Pearl River delivers approximately 95.17% of its annual sediment load to the PRE and the adjacent shelf (Figure 7a) under relatively calm wind and wave conditions (first column of Figure 4), leading to predominant proximal deposition (Figure 5f). In contrast, the winter dry season is characterized by strong northeasterly monsoon winds that generate high-energy waves (second column of Figure 4), significantly increasing bottom shear stress (Figures 4g-h). This process resuspends previously deposited sediments and facilitates their redistribution, particularly toward regions such as the Beibu Gulf (Figure 6f).

~~In the PRE, proximal deposition predominantly occurs during the wet summer, when winds and waves are relatively weak. In contrast, distal deposition is more prominent in the dry winter, driven by strong northeasterly winds and high waves.~~

~~Indeed, the PRE and adjacent shelf exhibits a fascinating seasonal dynamics where sediment delivery and sediment remobilization occur at different times of the year. During the summer wet season, the region experiences substantial sediment~~

1461 ~~delivery due to high river discharge from the Pearl River, bringing a large influx of~~  
1462 ~~riverine sediments to the shelf. Conversely, in winter, when strong waves driven by~~  
1463 ~~northeast monsoon winds dominate, riverine sediment remobilization becomes the~~  
1464 ~~key process. These high-energy waves increase bottom shear stress, resuspend~~  
1465 ~~previously deposited sediments and redistribute them across the shelf, especially in~~  
1466 ~~sheltered areas like the Beibu Gulf.~~

1467 The PRE exhibits distinctive geomorphological features, yet its fine-grained  
1468 sediment transport on the continental shelf conforms to general patterns observed in  
1469 other monsoon-influenced estuarine systems. ~~Other estuaries exhibit similar~~ Similar  
1470 multiple-stage ~~step~~ sediment delivery and dispersal mechanisms have been  
1471 documented in various major estuaries ~~patterns,~~ including such as the Yellow River  
1472 Estuary (Bian et al., 2013; Zeng et al., 2015), Changjiang River Estuary (Zeng et al.,  
1473 2015), and Mekong River Estuary (Xue et al., 2012; Eidam et al., 2017).  
1474 demonstrating comparable sedimentary processes under monsoon climatic influences.

1475 In these systems, sediment transport is not confined to a single process but rather  
1476 occurs in stages, influenced by seasonal variations in hydrodynamic conditions. Like  
1477 the PRE, the Mekong experiences distinct phases of sediment deposition, with fine  
1478 sediments being delivered during periods of high river discharge and then  
1479 redistributed by waves and tidal forces, particularly during monsoonal shifts (Xue et  
1480 al., 2012; Eidam et al., 2017). These complex patterns highlight the interplay between  
1481 riverine inputs, coastal morphology, and oceanographic processes in shaping sediment  
1482 dynamics.

1483        These sediment delivery patterns have implications beyond sediment fate,  
1484        particularly for carbon cycling. Sediment deposition in coastal and shelf areas plays a  
1485        significant role in trapping organic carbon, influencing long-term carbon burial rates  
1486        ([LaRowe et al., 2020](#)). Sediment dynamics directly influence the fate of organic  
1487        carbon (OC) in marine environments, where sediments function as both a sink and a  
1488        source of OC, playing a pivotal role in global carbon cycling ([Repasch et al., 2021](#)).  
1489        The multiple-step transport mechanisms can lead to varying carbon storage locations,  
1490        affecting the sequestration potential of these systems. Additionally, resuspension and  
1491        redistribution of sediments, especially during high-energy events, may expose  
1492        previously buried organic material, leading to carbon remineralization and influencing  
1493        coastal nutrient cycles and ecosystem health ([Ståhlberg et al., 2006](#); [Moriarty et al.,](#)  
1494        [2018](#)). Therefore, understanding these patterns is crucial for assessing the broader  
1495        impacts on carbon cycling and coastal biogeochemical processes.

1496        Furthermore, we evaluated the contributions of different physical processes by  
1497        comparing the Control run with sensitivity cases. Our analysis reveals distinct roles of  
1498        tidal forces, wave action, and background circulation in governing the transport and  
1499        deposition of Pearl River-derived sediments (Figures 8, 9, 11a-c, and 12a-c).

1500        Tidal dynamics predominantly influence sediment behavior within the PRE.  
1501        Neglecting tidal effects leads to an underestimation of bottom shear stress within the  
1502        estuary (Figures 8a-b), resulting in an overestimation of sediment deposition (Figure  
1503        11a) and consequently underestimating distal sediment retention (Figure 12a).

1504        Wave activity primarily controls sediment resuspension in three critical



1505 dimensions: (1) the river mouth, (2) the eastern and western nearshore regions outside  
1506 the estuary, and (3) periods characterized by high wave energy during winter (Figures  
1507 9c-d). The exclusion of wave effects results in overestimated sediment deposition in  
1508 these areas and periods (Figure 11b), ultimately leading to an underestimation of  
1509 sediment accumulation thickness in the Beibu Gulf (Figure 11b).

1510 Background circulation exerts its most significant influence during the summer  
1511 months (Figure 5a vs. Figure 9e). The strong northeastward background current in  
1512 summer serves as the primary driver for transporting Pearl River-derived sediments to  
1513 the continental shelf east of the PRE. When considering only the weak southerly  
1514 winds without the northeastward background current, merely 0.84% of Pearl River  
1515 sediments are transported to the eastern shelf, substantially overestimating distal  
1516 deposition (Figure 12c).

1517 ~~Our results indicate that during the wet summer period, 14.7% of river sediment~~  
1518 ~~can be transported to the southeast side of the PRE, with approximately half of it still~~  
1519 ~~retained on the eastern side of the PRE during the following dry winter, forming a~~  
1520 ~~proximal mud belt. However, due to winter winds and wave reshaping, the thickness~~  
1521 ~~of the riverine sediment deposition in the distal mud belt significantly decreases, with~~  
1522 ~~only one-third of the riverine sediment deposited in the wet summer period being~~  
1523 ~~retained during the ensuing dry winter. Our results indicate that 11.2% of the Pearl~~  
1524 ~~River's riverine sediment can be transported to the Beibu Gulf under the Wind and~~  
1525 ~~wave case, confirming the speculation by Ge et al. (2014) and validating the~~  
1526 ~~conclusions estimated by Lin et al. (2020). From a hydrodynamic perspective, Shi et~~

~~al. (2002) found that the net flux of currents in the Qiongzhou Strait is westward throughout the year. Our results for both wet summer and dry winter currents in the Qiongzhou Strait are consistent with Shi et al. (2002). This westward flow contributes to the westward transport of Pearl River sediment to the Beibu Gulf.~~

~~Our results highlight the wind and wave effects on the riverine sediment suspension, resuspension, transport, and net deposition during a typical year. We've developed a conceptual diagram illustrating the wind and wave effects on shelf hydrodynamics and riverine sediment dynamics based on our model results (Figure 14). When there is no wind or wave, strong stratification occurs, causing the plume to expand outward from the surface, with low TKE and bottom shear stress, resulting in weak resuspension (Figure 14a, c). Most of the riverine sediment deposits near the estuary, while the strong tidal-induced upwelling to the east of the estuary triggers the eastward expansion of the plume (Figure 14a). Under the wind and wave effects, TKE and eddy viscosity increase, stratification weakens, and during the summer southerly monsoon, the upwelling area to the east of the estuary expands (Figure 14b, d). This leads to some of the riverine sediment being transported southeastward along the edge of the upwelling plume interface (Figure 14b). Ekman transport causes an increase in the cross-shore gradients of water level, salinity, and density to the west of the estuary, triggering stronger geostrophic currents and vertical shear (Figure 14d). With increased bottom TKE and shear stress by wave, resuspension strengthens and net deposition decreases, resulting in higher riverine SSC and a significant increase in the westward riverine sediment flux, compounded by the intensified westward flow. As a~~

~~result, more Pearl River sediments are transported to the Beibu Gulf (Figure 14b). Due to the sheltering effect of the Leizhou Peninsula against the northeast winds and waves, these sediments are more likely to settle on the seafloor in the Beibu Gulf region compared to those on the continental shelf east of the Leizhou Peninsula.~~

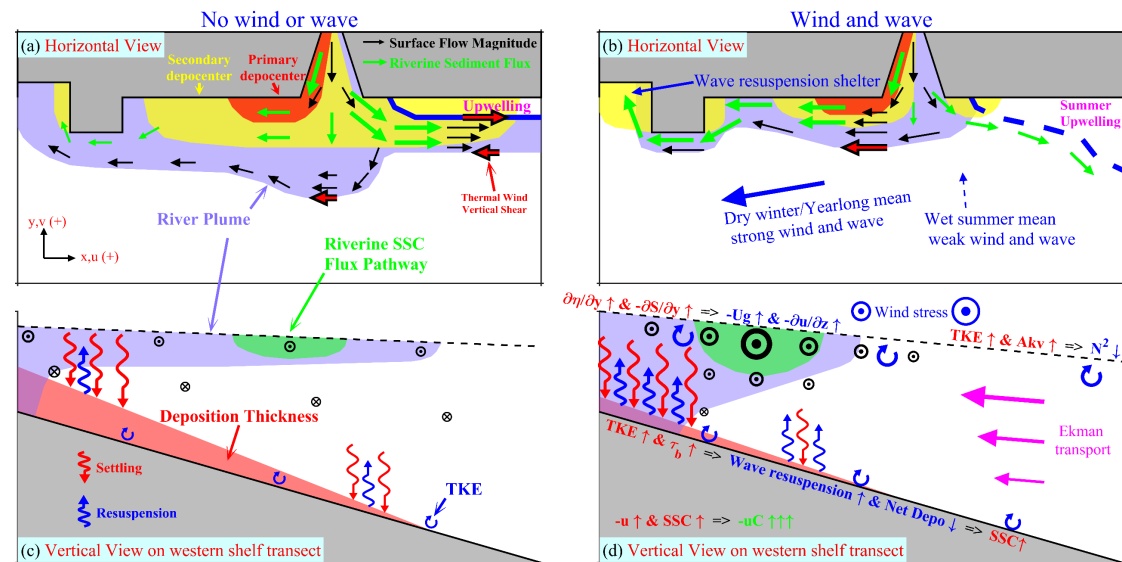


**Figure 14.** ~~Schematic of the wind and wave effects on river plume dynamics and riverine sediment dispersal dynamics over the shelf. The first column represents No wind or wave conditions, while the second column represents Wind and wave conditions. The first row denotes horizontal distribution, and the second row denotes vertical distribution of the cross-shore transect on the western shelf.~~

### 4.3 Limitations and Future Work

This study ~~has focused~~ focuses on analyzing simulation results from a typical year, encompassing both wet and dry seasons from 2017 to 2018, to understand the seasonal variations and annual patterns of suspension, transport, and deposition of sediment in the PRE and adjacent shelf. However, it's essential to recognize that the

long-term sediment transport and deposition dynamics in the Pearl River are influenced by numerous complex factors. These include changes in sea level and coastal line ([Church and White, 2006](#); [Harff et al., 2010](#); [Hong et al., 2020](#)), alterations in wind field and precipitation ([Ning and Qian, 2009](#); [Young et al., 2011](#)), natural sedimentation within the Pearl River Delta ([Wu et al., 2010](#)), modifications in sediment load and underwater volume of the estuary caused by anthropogenic impact ([Wu et al., 2014](#); [Wu et al., 2018](#); [Lin et al., 2022](#)). Therefore, while this study sheds light on seasonal and annual timescale patterns, it cannot fully represent the short or long-term transport and deposition trends of the Pearl River sediment. Yet for many shelf systems, a lot of the sediment transport happens during ~~short~~-[short](#)-lived events. Consideration of the episodicity of transport would be helpful for future studies.

Additionally, it's important to note that this article primarily focuses on the fate of the Pearl River sediment on the inner shelf. However, there are other smaller rivers within the Pearl River plume's expansion range, like the Han River, Rong River, Moyang River, Jian River, and Nandu River ([Liu et al., 2016](#)). Although these rivers contribute less freshwater and sediment compared to the Pearl River, they still impact seawater salinity, suspended sediment concentration, and seabed geomorphology ([Wang et al., 2023](#); [Zong et al., 2024](#)). Hence, there is a need for further systematic research to understand the processes and impacts of these smaller rivers comprehensively.

Lastly, while the model used in this study has shown good validation results, conducting ~~numerous~~-[more](#) sensitivity experiments on sediment parameters, such as

settling velocity and critical ~~shear erosion~~-stress for erosion, would be beneficial. Settling velocity can influence the location of sediment depocenters, with higher settling velocities leading to more ~~sediment-proximal~~ entrapment ~~and older sediment age in the estuary~~ and vice versa ([Ralston and Geyer, 2017](#)). Similarly, critical erosion stress can affect the resuspension of deposited sediment, with higher critical erosion stress resulting in less resuspension and more deposition especially during neap tides and weak wind wave events ([Dong et al., 2020](#); [Choi et al., 2023](#)). Conducting such sensitivity analyses would enhance our understanding of sediment dynamics in estuaries and shelves. Besides, the model does not account for cohesive processes, such as consolidation and flocculation, which can significantly impact sediment behavior ([Sherwood et al., 2018](#)). Our model does not incorporate wave and current-supported gravity flows, which are important factors influencing sediment transport in submarine canyon areas ([Harris et al., 2005](#); [Ma et al., 2010](#); [Zhang et al., 2020](#)). Since our study area primarily focuses on the continental shelf and the simulated results indicate that sediment transport occurs mainly in the shallow inner shelf, where canyons are relatively rare, this omission has a relatively minor impact on our results.

## **56. Conclusions**

This study utilizes the COAWST model to quantitatively analyze the seasonal suspension, transport, and ~~ultimate-annual~~ fate of Pearl River-derived sediment on the continental shelf over a typical year, capturing key marine variables such as water level, wave height, flow velocity, salinity, temperature, and SSC.

~~The study indicates that approximately 62% of riverine sediment remains near the estuary annually.~~ The monsoonal nature of the northern SCS (Figures 4a-b) induces pronounced seasonal variations in Pearl River-derived sediment transport and deposition (Figures 5 and 6). During the wet summer, calm conditions foster initial sediment deposition via the river plume (Figures 5 and 7a). Conversely, winter's stronger winds and waves resuspend and transport sediments into Beibu Gulf, primarily during this dry season (Figures 6 and 7b). Our quantitative assessment reveals distinct spatial patterns in the annual fate of riverine sediments: approximately 66.45% of the total sediment load is retained within the estuarine vicinity, while 9.2% is deposited on the continental shelf east of the PRE. Furthermore, 8.86% and 10.3% of the sediment is transported to and retained in the Beibu Gulf and the area south of Hainan Island, respectively (Figure 7c). ~~Overall, sediment predominantly follows a southwestward pathway, with wind and wave interactions diminishing proximal riverine sediment deposition levels to 83% of those in No wind or wave conditions, resulting in a remarkable fivefold increase in westward alongshore sediment flux.~~

Furthermore, we evaluated the contributions of different physical processes by comparing the Control run with the reduced-physics sensitivity experiments. Our analysis reveals distinct roles of tidal forces, wave action, and background circulation in governing the transport and deposition of Pearl River-derived sediments (Figures 8, 9, 11a-c, and 12a-c).

Tidal dynamics primarily govern sediment behavior in the PRE. Neglecting tides underestimates the bottom shear stress in the PRE (Figures 8a-b), overestimates

sediment deposition in the PRE (Figure 11a), and underestimates distal sediment retention (Figure 12a). Wave activity primarily controls sediment resuspension in three critical dimensions: (1) the river mouth, (2) the eastern and western nearshore regions outside the estuary, and (3) periods characterized by high wave energy during winter (Figures 9c-d). Excluding waves leads to overestimated sediment deposition in these areas and times (Figure 11b), underestimating accumulation in the Beibu Gulf (Figure 11b). Background circulation is most influential in summer (Figure 5a vs. Figure 9e), with a strong northeastward current transporting Pearl River-derived sediments to the eastern shelf. Without this current and under weak southerly winds, only 0.84% of sediments reach the eastern shelf, overestimating distal deposition (Figure 12c).

The sediment model solutions are also highly sensitive to the parameterization of sediment characteristics and initial conditions (Figures 10, 11d-f, and 12d-f). Neglecting the need for a higher critical shear stress for erosion in winter overestimates resuspension and erosion on the shelf east of the Leizhou Peninsula during this season (Figure 10b), leading to a greater distal retention (Figure 12d). Increasing the settling velocity reduces SSC (Figures 10c-d) while overestimating the proximal retention and underestimating the distal retention (Figure 12e). Additionally, the model solutions are influenced by sediment initial conditions. If the model domain initially includes a full year of Pearl River-derived sediment retention, re-running the simulation results in further transport of previously retained sediments from the Beibu Gulf to more distal areas. However, the model is relatively insensitive to the initial

[bed grain size distribution \(Experiment Cycle2; see Section 4.1\).](#)

~~The model indicates that wind dynamics significantly impact both surface and bottom boundary layers, enhancing vertical mixing and bottom shear stress, which raises nearshore SSC while decreasing offshore SSC and sediment deposition thickness. Enhanced cross-shore gradients of water level and density further promote westward geostrophic flow, facilitating sediment transport to more distant areas. This research offers novel insights into the complex interactions between wind, waves, and riverine sediment dynamics on continental shelves.~~

## Acknowledgments

This research was funded by the National Natural Science Foundation of China (grant numbers 42306015 and 42276169), the China Postdoctoral Science Foundation (grant number 2023M743988). Wenping Gong is supported by the Southern Marine Science and Engineering Guangdong Laboratory (Zhuhai) (SML2023SP238). The authors would like to thank the crew of the R/V Changhe Ocean for their valuable contribution during collection of the field-data. [We express our gratitude to the two anonymous reviewers for their valuable suggestions in enhancing and improving this article.](#)

## Data availability

The HYbrid Coordinate Ocean Model [\(HYCOM\)](#) outputs are from: <http://hycom.org/hycom>. The NCEP Climate Forecast System Version 2 (CFSv2) reanalysis data can be obtained at the following website: <https://rda.ucar.edu/datasets/ds094.1/dataaccess/>. The [NOAA](#) WAVEWATCH III



[global ocean](#) wave model output fields can be downloaded from:  
<ftp://polar.ncep.noaa.gov/pub/history/waves>. Hourly water-level data observed at  
Quarry Bay station are provided by the Hong Kong Observatory website:  
<https://www.hko.gov.hk/sc/tide/marine/realtide.htm?s=QUB&t=TABLE>. Hourly  
water-level data from Zhapo and Qinglan stations, provided by the Flanders Marine  
Institute (VLIZ), are part of the UNESCO/IOC Global Sea Level Observing System  
(GLOSS) and accessible at <http://www.ioc-sealevelmonitoring.org>. The mooring data  
for the ~~S1~~ [M1 and M2](#) stations are sourced from [Liu et al. \(2023\)](#) and [Li et al. \(2024a\)](#).  
The figure data and model configuration files used in this paper can be downloaded  
from: <https://doi.org/10.5281/zenodo.15013448>. ~~The field and numerical data used in  
this paper can be downloaded from: <https://doi.org/10.5281/zenodo.13740968>.~~

## Declaration of Competing interests

The authors declare that [they have](#) ~~there are~~ no [known](#) competing [financial](#)  
interests [or personal relationships that could have appeared to influence the work](#)  
[reported in this paper](#) ~~among any of the authors~~.

## CRediT authorship contribution statement

**Guang Zhang:** Conceptualization, Numerical modeling, Validation, Data  
visualization, Writing—original draft, and Funding acquisition. **Suan Hu:** Writing—  
review & editing, [Validation](#). **Xiaolong Yu:** Writing—review & editing. **Heng**  
**Zhang:** Writing—review & editing. **Wenping Gong:** Writing—review & editing,  
and Funding acquisition

## Supplement:

We have included the validation<sup>s</sup> and analysis of the model's water levels, Hsig, flow velocities, salinity, temperature, and SSC, ~~as well as the spatial results and analysis of annual averages for various oceanic elements from two cases used to support the discussion,~~ in the Supplement.

## References

- Bever, A. J., Harris, C. K., Sherwood, C. R., and Signell, R. P.: Deposition and flux of sediment from the Po River, Italy: An idealized and wintertime numerical modeling study, *Marine Geology*, 260, 69-80, 10.1016/j.margeo.2009.01.007, 2009.
- Bever, A. J., and MacWilliams, M. L.: Simulating sediment transport processes in San Pablo Bay using coupled hydrodynamic, wave, and sediment transport models, *Marine Geology*, 345, 235-253, 10.1016/j.margeo.2013.06.012, 2013.
- Bian, C., Jiang, W., and Greatbatch, R. J.: An exploratory model study of sediment transport sources and deposits in the Bohai Sea, Yellow Sea, and East China Sea, *Journal of Geophysical Research: Oceans*, 118, 5908-5923, <https://doi.org/10.1002/2013JC009116>, 2013.
- Booij, N., Ris, R. C., and Holthuijsen, L. H.: A third-generation wave model for coastal regions: 1. Model description and validation, *Journal of Geophysical Research: Oceans*, 104, 7649-7666, <https://doi.org/10.1029/98JC02622>, 1999.
- Brand, A., Lacy, J. R., Hsu, K., Hoover, D., Gladding, S., and Stacey, M. T.: Wind-enhanced resuspension in the shallow waters of South San Francisco Bay: Mechanisms and potential implications for cohesive sediment transport, *Journal of Geophysical Research*, 115,

10.1029/2010jc006172, 2010.

Burchard, H., Schuttelaars, H. M., and Ralston, D. K.: Sediment Trapping in Estuaries, *Annual Review of Marine Science*, 10, 371-395, 10.1146/annurev-marine-010816-060535, 2018.

Cao, L., Liu, J., Shi, X., He, W., and Chen, Z.: Source-to-sink processes of fluvial sediments in the northern South China Sea: Constraints from river sediments in the coastal region of South China, *Journal of Asian Earth Sciences*, 185, 104020, 10.1016/j.jseaes.2019.104020, 2019.

Cao, Z., Ren, J., Deng, Z., Ye, L., and Wu, J.: Small-scale spatial variability in erosion threshold and bedform for cohesive sediment measured by 3D Sonar, *Journal of Hydrology*, 650, 132513, 10.1016/j.jhydrol.2024.132513, 2025.

Chapman, D. C.: Numerical Treatment of Cross-Shelf Open Boundaries in a Barotropic Coastal Ocean Model, *Journal of Physical Oceanography*, 15, 1060-1075, 1985.

Charnock, H.: Wind stress on a water surface, *Quarterly Journal of the Royal Meteorological Society*, 81, 639-640, <https://doi.org/10.1002/qj.49708135027>, 1955.

Chassignet, E. P., Hurlburt, H. E., Smedstad, O. M., Halliwell, G. R., Hogan, P. J., Wallcraft, A. J., Baraille, R., and Bleck, R.: The HYCOM (HYbrid Coordinate Ocean Model) data assimilative system, *Journal of Marine Systems*, 65, 60-83, <https://doi.org/10.1016/j.jmarsys.2005.09.016>, 2007.

Chen, S.-N., Geyer, W. R., Sherwood, C. R., and Ralston, D. K.: Sediment transport and deposition on a river-dominated tidal flat: An idealized model study, *Journal of Geophysical Research*, 115, 10.1029/2010jc006248, 2010.

Chen, Y., Deng, B., Saito, Y., Wang, Z., Yang, X., and Wu, J.: Pearl River sediment dispersal over its associated delta–estuary–shelf system during the Holocene, *Sedimentology*, 70, 2331-2354,

10.1111/sed.13123, 2023.

Chen, Z., Pan, J., and Jiang, Y.: Role of pulsed winds on detachment of low salinity water from the Pearl River Plume Upwelling and mixing processes, *Journal of Geophysical Research: Oceans*, 121, 2769-2788, 10.1002/2015JC011337, 2016.

Chen, Z., Gong, W., Cai, H., Chen, Y., and Zhang, H.: Dispersal of the Pearl River plume over continental shelf in summer, *Estuarine, Coastal and Shelf Science*, 194, 252-262, 10.1016/j.ecss.2017.06.025, 2017a.

Chen, Z., Pan, J., Jiang, Y., and Lin, H.: Far-reaching transport of Pearl River plume water by upwelling jet in the northeastern South China Sea, *Journal of Marine Systems*, 173, 60-69, 10.1016/j.jmarsys.2017.04.008, 2017b.

Chen, Z., Jiang, Y., Wang, J., and Gong, W.: Influence of a River Plume on Coastal Upwelling Dynamics: Importance of Stratification, *Journal of Physical Oceanography*, 49, 2345-2363, 10.1175/jpo-d-18-0215.1, 2019.

Cheng, P., Li, M., and Li, Y.: Generation of an estuarine sediment plume by a tropical storm, *Journal of Geophysical Research: Oceans*, 118, 856-868, 10.1002/jgrc.20070, 2013.

Chi, Y., and Rong, Z.: Effects of Breaking and Non -Breaking Surface V

Changjiang River Plume Dynamics in Summer, *Journal of Geophysical Research: Oceans*, 128, 10.1029/2022jc019501, 2023.

Choi, S. M., Seo, J. Y., and Ha, H. K.: Contribution of local erosion enhanced by winds to sediment transport in intertidal flat, *Marine Geology*, 465, 107171, 10.1016/j.margeo.2023.107171, 2023.

Church, J. A., and White, N. J.: A 20th century acceleration in global sea-level rise, *Geophysical Research Letters*, 33, n/a-n/a, 10.1029/2005gl024826, 2006.

- 1763 Dai, S. B., Yang, S. L., and Cai, A. M.: Impacts of dams on the sediment flux of the Pearl River,  
1764 southern China, *Catena*, 76, 36-43, 10.1016/j.catena.2008.08.004, 2008.
- 1765 Dong, H., Jia, L., He, Z., Yu, M., and Shi, Y.: Application of parameters and paradigms of the erosion  
1766 and deposition for cohesive sediment transport modelling in the Lingdingyang Estuary, China,  
1767 *Applied Ocean Research*, 94, 101999, 10.1016/j.apor.2019.101999, 2020.
- 1768 Dong, L., Su, J., Wong, L., Cao, Z., and Chen, J.: Seasonal variation and dynamics of the Pearl River  
1769 plume, *Continental Shelf Research*, 24, 1761-1777, 10.1016/j.csr.2004.06.006, 2004.
- 1770 Drennan, W. M., Taylor, P. K., and Yelland, M. J.: Parameterizing the sea surface roughness, *Journal of*  
1771 *Physical Oceanography*, 35, 835-848, Doi 10.1175/Jpo2704.1, 2005.
- 1772 Dyer, K. R.: *Estuaries: A Physical Introduction*, 2nd Edition, John Wiley & Sons, Chichester, 195 pp.,  
1773 1997.
- 1774 Egbert, G. D., and Erofeeva, S. Y.: Efficient inverse Modeling of barotropic ocean tides, *Journal of*  
1775 *Atmospheric and Oceanic Technology*, 19, 183-204, Doi  
1776 10.1175/1520-0426(2002)019<0183:Eimobo>2.0.Co;2, 2002.
- 1777 Eidam, E. F., Nittrouer, C. A., Ogston, A. S., DeMaster, D. J., Liu, J. P., Nguyen, T. T., and Nguyen, T.  
1778 N.: Dynamic controls on shallow clinoform geometry: Mekong Delta, Vietnam, *Continental Shelf*  
1779 *Research*, 147, 165-181, 10.1016/j.csr.2017.06.001, 2017.
- 1780 Fairall, C. W., Bradley, E. F., Rogers, D. P., Edson, J. B., and Young, G. S.: Bulk parameterization of  
1781 air-sea fluxes for Tropical Ocean-Global Atmosphere Coupled-Ocean Atmosphere Response  
1782 Experiment, *Journal of Geophysical Research: Oceans*, 101, 3747-3764,  
1783 <https://doi.org/10.1029/95JC03205>, 1996.
- 1784 Flather, R. A.: A tidal model of the north-west European continental shelf, *Memoires Societe Royale*

1785 des Sciences de Liege, 10, 141-164, 1976.

1786 Gan, J., Cheung, A., Guo, X., and Li, L.: Intensified upwelling over a widened shelf in the northeastern  
 1787 South China Sea, *Journal of Geophysical Research*, 114, 10.1029/2007jc004660, 2009.

1788 Gan, J., San Ho, H., and Liang, L.: Dynamics of Intensified Downwelling Circulation over a Widened  
 1789 Shelf in the Northeastern South China Sea, *Journal of Physical Oceanography*, 43, 80-94,  
 1790 10.1175/jpo-d-12-02.1, 2013.

1791 Gao, S., and Collins, M. B.: Holocene sedimentary systems on continental shelves, *Marine Geology*,  
 1792 352, 268-294, 10.1016/j.margeo.2014.03.021, 2014.

1793 Gao, X., Chen, S., Xie, X., Long, A., and Ma, F.: Non-aromatic hydrocarbons in surface sediments near  
 1794 the Pearl River estuary in the South China Sea, *Environmental Pollution*, 148, 40-47,  
 1795 10.1016/j.envpol.2006.11.001, 2007.

1796 Gao, X., Arthur Chen, C.-T., Wang, G., Xue, Q., Tang, C., and Chen, S.: Environmental status of Daya  
 1797 Bay surface sediments inferred from a sequential extraction technique, *Estuarine, Coastal and  
 1798 Shelf Science*, 86, 369-378, 10.1016/j.ecss.2009.10.012, 2010.

1799 Ge, Q., Liu, J. P., Xue, Z., and Chu, F.: Dispersal of the Zhujiang River (Pearl River) derived sediment  
 1800 in the Holocene, *Acta Oceanologica Sinica*, 33, 1-9, 10.1007/s13131-014-0407-8, 2014.

1801 Ge, Q., Xue, Z., Yao, Z., Zang, Z., and Chu, F.: Anti-phase relationship between the East Asian winter  
 1802 monsoon and summer monsoon during the Holocene?, *Journal of Ocean University of China*, 16,  
 1803 175-183, 10.1007/s11802-017-3098-x, 2017.

1804 Ge, Q., Xu, D., Ye, L., Yang, K., and Yao, Z.: Linking Monsoon Activity with River-Derived Sediments  
 1805 Deposition in the Northern South China Sea, *Journal of Ocean University of China*, 18, 1098-1104,  
 1806 10.1007/s11802-019-4155-4, 2019.

1807 Geyer, W. R., Hill, P. S., and Kineke, G. C.: The transport, transformation and dispersal of sediment by  
1808 buoyant coastal flows, *Continental Shelf Research*, 24, 927-949, 10.1016/j.csr.2004.02.006, 2004.

1809 Gong, W., Chen, Y., Zhang, H., and Chen, Z.: Effects of Wave–Current Interaction on Salt Intrusion  
1810 During a Typhoon Event in a Highly Stratified Estuary, *Estuaries and Coasts*, 41, 1904-1923,  
1811 10.1007/s12237-018-0393-8, 2018a.

1812 Gong, W., Lin, Z., Chen, Y., Chen, Z., Shen, J., and Zhang, H.: Effect of waves on the dispersal of the  
1813 Pearl River plume in winter, *Journal of Marine Systems*, 186, 47-67,  
1814 10.1016/j.jmarsys.2018.05.003, 2018b.

1815 Haidvogel, D. B., Arango, H., Budgell, W. P., Cornuelle, B. D., Curchitser, E., Di, L. E., Fennel, K.,  
1816 Geyer, W. R., Hermann, A. J., Lanerolle, L., Levin, J., McWilliams, J. C., Miller, A. J., Moore, A.  
1817 M., Powell, T. M., Shchepetkin, A. F., Sherwood, C. R., Signell, R. P., Warner, J. C., and Wilkin, J.:  
1818 Ocean forecasting in terrain-following coordinates: Formulation and skill assessment of the  
1819 Regional Ocean Modeling System, *Journal of Computational Physics*, 227, 3595-3624,  
1820 10.1016/j.jcp.2007.06.016, 2008.

1821 Hanebuth, T. J. J., Lantzsch, H., and Nizou, J.: Mud depocenters on continental shelves—appearance,  
1822 initiation times, and growth dynamics, *Geo-Marine Letters*, 35, 487-503,  
1823 10.1007/s00367-015-0422-6, 2015.

1824 Harff, J., Leipe, T., and Zhou, D.: Pearl River Estuary related sediments as response to Holocene  
1825 climate change and anthropogenic impact (PECAI), *Journal of Marine Systems*, 82, S1-S2,  
1826 10.1016/j.jmarsys.2010.02.008, 2010.

1827 Harris, C. K., Traykovski, P. A., and Geyer, W. R.: Flood dispersal and deposition by near -bed  
1828 gravitational sediment flows and oceanographic transport: A numerical modeling study of the Eel

1829 River shelf, northern California, Journal of Geophysical Research: Oceans, 110,  
 1830 10.1029/2004jc002727, 2005.  
 1831 Harris, C. K., Sherwood, C. R., Signell, R. P., Bever, A. J., and Warner, J. C.: Sediment dispersal in the  
 1832 northwestern Adriatic Sea, Journal of Geophysical Research, 113, 10.1029/2006jc003868, 2008.  
 1833 Hong, B., Liu, Z., Shen, J., Wu, H., Gong, W., Xu, H., and Wang, D.: Potential physical impacts of  
 1834 sea-level rise on the Pearl River Estuary, China, Journal of Marine Systems, 201, 103245,  
 1835 10.1016/j.jmarsys.2019.103245, 2020.  
 1836 Horner-Devine, A. R., Hetland, R. D., and MacDonald, D. G.: Mixing and Transport in Coastal River  
 1837 Plumes, Annual Review of Fluid Mechanics, 47, 569-594, 10.1146/annurev-fluid-010313-141408,  
 1838 2015.  
 1839 Hu, J., Li, S., and Geng, B.: Modeling the mass flux budgets of water and suspended sediments for the  
 1840 river network and estuary in the Pearl River Delta, China, Journal of Marine Systems, 88, 252-266,  
 1841 10.1016/j.jmarsys.2011.05.002, 2011.  
 1842 Hu, S., Li, Y., Hu, P., Zhang, H., Zhang, G., and Gong, W.: The Impacts of Far -Field  
 1843 Typhoon -Generated Coastal T  
 1844 Sea: A Case Study of Typhoon In -Fa, Journal of Ge  
 1845 10.1029/2024jc021359, 2024.  
 1846 Huang, D., Du, J., Deng, B., and Zhang, J.: Distribution patterns of particle-reactive radionuclides in  
 1847 sediments off eastern Hainan Island, China: Implications for source and transport pathways,  
 1848 Continental Shelf Research, 57, 10-17, 10.1016/j.csr.2012.04.019, 2013.  
 1849 Jacob, R., Larson, J., and Ong, E.:  $M \times N$  Communication and Parallel Interpolation in Community  
 1850 Climate System Model Version 3 Using the Model Coupling Toolkit, IJHPCA, 19, 293-307,



1851 10.1177/1094342005056116, 2005.

1852 Kirby, M. F., Devoy, B., Law, R. J., Ward, A., and Aldridge, J.: The use of a bioassay based approach to

1853 the hazard/risk assessment of cargo derived toxicity during shipping accidents: a case study--the

1854 MSC Napoli, Marine Pollution Bulletin, 56, 781-786, 10.1016/j.marpolbul.2008.01.006, 2008.

1855 Krige, D. G.: A Statistical Approach to Some Basic Mine Valuation Problems on the Witwatersrand,

1856 Chemical, Metallurgical and Mining Society of South Africa, 1951.

1857 Kuehl, S. A., Alexander, C. R., Blair, N. E., Harris, C. K., Marsaglia, K. M., Ogston, A. S., Orpin, A. R.,

1858 Roering, J. J., Bever, A. J., Bilderback, E. L., Carter, L., Cerovski-Darriau, C., Childress, L. B.,

1859 Reide Corbett, D., Hale, R. P., Leithold, E. L., Litchfield, N., Moriarty, J. M., Page, M. J., Pierce,

1860 L. E. R., Upton, P., and Walsh, J. P.: A source-to-sink perspective of the Waipaoa River margin,

1861 Earth-Science Reviews, 153, 301-334, 10.1016/j.earscirev.2015.10.001, 2016.

1862 Kumar, N., Voulgaris, G., Warner, J. C., and Olabarrieta, M.: Implementation of the vortex force

1863 formalism in the coupled ocean-atmosphere-wave-sediment transport (COAWST) modeling

1864 system for inner shelf and surf zone applications, Ocean Modelling, 47, 65-95,

1865 10.1016/j.ocemod.2012.01.003, 2012.

1866 Lai, Z., Ma, R., Huang, M., Chen, C., Chen, Y., Xie, C., and Beardsley, R. C.: Downwelling wind, tides,

1867 and estuarine plume dynamics, Journal of Geophysical Research: Oceans, 121, 4245-4263,

1868 10.1002/2015jc011475, 2016.

1869 LaRowe, D. E., Arndt, S., Bradley, J. A., Estes, E. R., Hoarfrost, A., Lang, S. Q., Lloyd, K. G.,

1870 Mahmoudi, N., Orsi, W. D., Shah Walter, S. R., Steen, A. D., and Zhao, R.: The fate of organic

1871 carbon in marine sediments - New insights from recent data and analysis, Earth-Science Reviews,

1872 204, 103146, 10.1016/j.earscirev.2020.103146, 2020.

1873 Larson, J., Jacob, R., and Ong, E.: The Model Coupling Toolkit: A New Fortran90 Toolkit for Building  
 1874 Multiphysics Parallel Coupled Models, *IJHPCA*, 19, 277-292, 2005.

1875 Li, J., Li, M., and Xie, L.: Observations of near-inertial oscillations trapped at inclined front on  
 1876 continental shelf of the northwestern South China Sea, *EGUsphere*, 2024, 1-25,  
 1877 10.5194/egusphere-2024-3909, 2024a.

1878 Li, X., Chrysagi, E., Klingbeil, K., and Burchard, H.: Impact of Islands on Tidally Dominated River  
 1879 Plumes: A High-Resolution Modeling Study, *Journal of Geophysical Research: Oceans*, 129,  
 1880 e2023JC020272, <https://doi.org/10.1029/2023JC020272>, 2024b.

1881 Li, Y., and Li, M.: Effects of winds on stratification and circulation in a partially mixed estuary, *Journal*  
 1882 *of Geophysical Research*, 116, 10.1029/2010jc006893, 2011.

1883 Lin, S., Niu, J., Liu, G., Wei, X., and Cai, S.: Variations of suspended sediment transport caused by  
 1884 changes in shoreline and bathymetry in the Zhujiang (Pearl) River Estuary in the wet season, *Acta*  
 1885 *Oceanologica Sinica*, 41, 54-73, 10.1007/s13131-022-2017-1, 2022.

1886 Lin, W., Feng, Y., Yu, K., Lan, W., Wang, Y., Mo, Z., Ning, Q., Feng, L., He, X., and Huang, Y.:  
 1887 Long-lived radionuclides in marine sediments from the Beibu Gulf, South China Sea: Spatial  
 1888 distribution, controlling factors, and proxy for transport pathway, *Marine Geology*, 424, 106157,  
 1889 10.1016/j.margeo.2020.106157, 2020.

1890 Liu, G., and Cai, S.: Modeling of suspended sediment by coupled wave-current model in the Zhujiang  
 1891 (Pearl) River Estuary, *Acta Oceanologica Sinica*, 38, 22-35, 10.1007/s13131-019-1455-3, 2019.

1892 Liu, H., Ye, L., Zhou, W., and Wu, J.: Salt-wedge intrusion-retreat cycle induced sediment flocculation  
 1893 dynamics in bottom boundary layer (BBL) of a micro-tidal estuary, *Marine Geology*, 466, 107175,  
 1894 10.1016/j.margeo.2023.107175, 2023.

- 1895 Liu, J. P., Xue, Z., Ross, K., Yang, Z., and Gao, S.: Fate of Sediments Delivered to the Sea by Asian  
1896 Large Rivers: Long-Distance Transport and Formation of Remote Alongshore Clinothems,  
1897 Sediment. Rec., 7, 10.2110/sedred.2009.4.4, 2009.
- 1898 Liu, Y., Gao, S., Wang, Y. P., Yang, Y., Long, J., Zhang, Y., and Wu, X.: Distal mud deposits associated  
1899 with the Pearl River over the northwestern continental shelf of the South China Sea, Marine  
1900 Geology, 347, 43-57, 10.1016/j.margeo.2013.10.012, 2014.
- 1901 Liu, Z., Zhao, Y., Colin, C., Stattegger, K., Wiesner, M. G., Huh, C.-A., Zhang, Y., Li, X.,  
1902 Sompongchaiyakul, P., You, C.-F., Huang, C.-Y., Liu, J. T., Siringan, F. P., Le, K. P., Sathiamurthy,  
1903 E., Hantoro, W. S., Liu, J., Tuo, S., Zhao, S., Zhou, S., He, Z., Wang, Y., Bunsomboonsakul, S.,  
1904 and Li, Y.: Source-to-sink transport processes of fluvial sediments in the South China Sea,  
1905 Earth-Science Reviews, 153, 238-273, 10.1016/j.earscirev.2015.08.005, 2016.
- 1906 Lu, X., Wang, Z., Guo, X., Gu, Y., Liang, W., and Liu, L.: Impacts of metal contamination and  
1907 eutrophication on dinoflagellate cyst assemblages along the Guangdong coast of southern China,  
1908 Marine Pollution Bulletin, 120, 239-249, 10.1016/j.marpolbul.2017.05.032, 2017.
- 1909 Ma, Y., Friedrichs, C. T., Harris, C. K., and Wright, L. D.: Deposition by seasonal wave- and  
1910 current-supported sediment gravity flows interacting with spatially varying bathymetry: Waiapu  
1911 shelf, New Zealand, Marine Geology, 275, 199-211, <https://doi.org/10.1016/j.margeo.2010.06.001>,  
1912 2010.
- 1913 Madsen, O. S.: Spectral Wave-Current Bottom Boundary Layer Flows, Coastal Engineering 1, 384-398,  
1914 1994.
- 1915 Mao, Q., Shi, P., Yin, K., Gan, J., and Qi, Y.: Tides and tidal currents in the Pearl River Estuary,  
1916 Continental Shelf Research, 24, 1797-1808, 10.1016/j.csr.2004.06.008, 2004.

1917 McWilliams, J. C., Restrepo, J. M., and Lane, E. M.: An asymptotic theory for the interaction of waves  
 1918 and currents in coastal waters, *Journal of Fluid Mechanics*, 511, 135-178,  
 1919 10.1017/s0022112004009358, 2004.

1920 Meade, R. H.: Landward Transport of Bottom Sediments in Estuaries of the Atlantic Coastal Plain,  
 1921 *Journal of Sedimentary Petrology*, 39, 222-234, 1969.

1922 Moriarty, J. M., Harris, C. K., Friedrichs, M. A. M., Fennel, K., and Xu, K.: Impact of Seabed  
 1923 Resuspension on Oxygen and Nitrogen Dynamics in the Northern Gulf of Mexico: A Numerical  
 1924 Modeling Study, *Journal of Geophysical Research: Oceans*, 123, 7237-7263,  
 1925 <https://doi.org/10.1029/2018JC013950>, 2018.

1926 Ning, L., and Qian, Y.: Interdecadal change in extreme precipitation over South China and its  
 1927 mechanism, *Advances in Atmospheric Sciences*, 26, 109-118, 10.1007/s00376-009-0109-x, 2009.

1928 Nittrouer, C. A., and Wright, L. D.: Transport of particles across continental shelves, *Reviews of*  
 1929 *Geophysics*, 32, 85-113, <https://doi.org/10.1029/93RG02603>, 1994.

1930 Orlanski, I.: A simple boundary condition for unbounded hyperbolic flows, *Journal of Computational*  
 1931 *Physics*, 21, 251-269, 10.1016/0021-9991(76)90023-1, 1976.

1932 Ou, S., Zhang, H., and Wang, D.: Dynamics of the buoyant plume off the Pearl River Estuary in  
 1933 summer, *Environmental Fluid Mechanics*, 9, 471-492, 10.1007/s10652-009-9146-3, 2009.

1934 Ralston, D. K., Geyer, W. R., and Warner, J. C.: Bathymetric controls on sediment transport in the  
 1935 Hudson River estuary: Lateral asymmetry and frontal trapping, *Journal of Geophysical Research:*  
 1936 *Oceans*, 117, 10.1029/2012jc008124, 2012.

1937 Ralston, D. K., and Geyer, W. R.: Sediment Transport Time Scales and Trapping Efficiency in a Tidal  
 1938 River, *Journal of Geophysical Research: Earth Surface*, 122, 2042-2063, 10.1002/2017jf004337,

- 1939 2017.
- 1940 Raymond, W. H., and Kuo, H. L.: A radiation boundary condition for multi -dimensional flows,
- 1941 Quarterly Journal of the Royal Meteorological Society, 110, 535-551, 1984.
- 1942 Repasch, M., Scheingross, J. S., Hovius, N., Lupker, M., Wittmann, H., Haghipour, N., Gröcke, D. R.,
- 1943 Orfeo, O., Eglinton, T. I., and Sachse, D.: Fluvial organic carbon cycling regulated by sediment
- 1944 transit time and mineral protection, Nature Geoscience, 14, 842-848,
- 1945 10.1038/s41561-021-00845-7, 2021.
- 1946 Rong, Z., Hetland, R. D., Zhang, W., and Zhang, X.: Current-wave interaction in the
- 1947 Mississippi-Atchafalaya river plume on the Texas-Louisiana shelf, Ocean Modelling, 84, 67-83,
- 1948 10.1016/j.ocemod.2014.09.008, 2014.
- 1949 Saha, S., Moorthi, S., Wu, X., Wang, J., Nadiga, S., Tripp, P., Behringer, D., Hou, Y.-T., Chuang, H.-y.,
- 1950 Iredell, M., Ek, M., Meng, J., Yang, R., Mendez, M. P., van den Dool, H., Zhang, Q., Wang, W.,
- 1951 Chen, M., and Becker, E.: The NCEP Climate Forecast System Version 2, Journal of Climate, 27,
- 1952 2185-2208, <https://doi.org/10.1175/JCLI-D-12-00823.1>, 2014.
- 1953 Sanford, L. P.: Wave-forced resuspension of upper Chesapeake Bay muds, Estuaries, 17, 148-165,
- 1954 1994.
- 1955 Shchepetkin, A. F., and McWilliams, J. C.: The regional oceanic modeling system (ROMS): a
- 1956 split-explicit, free-surface, topography-following-coordinate oceanic model, Ocean Modelling, 9,
- 1957 347-404, <https://doi.org/10.1016/j.ocemod.2004.08.002>, 2005.
- 1958 Shepard, F. P.: Nomenclature Based on Sand-silt-clay Ratios, Journal of Sedimentary Research, 24,
- 1959 151-158, 1954.
- 1960 Sherwood, C. R., Aretxabaleta, A. L., Harris, C. K., Rinehimer, J. P., Verney, R., and Ferré, B.:

1961 Cohesive and mixed sediment in the Regional Ocean Modeling System (ROMS v3.6)

1962 implemented in the Coupled Ocean–Atmosphere–Wave–Sediment Transport Modeling System

1963 (COAWST r1234), Geoscientific Model Development, 11, 1849-1871,

1964 10.5194/gmd-11-1849-2018, 2018.

1965 Shi, M., Chen, C., Xu, Q., Lin, H., Liu, G., Wang, H., Wang, F., and Yan, J.: The Role of Qiongzhou

1966 Strait in the Seasonal Variation of the South China Sea Circulation, Journal of Physical

1967 Oceanography, 32, 103-121, 2002.

1968 Skamarock, W. C., Klemp, J. B., Dudhia, J., Gill, D. O., Barker, D. M., Wang, W., and Powers, J. G.: A

1969 Description of the Advanced Research WRF Version 2, 2005,

1970 Smagorinsky, J.: GENERAL CIRCULATION EXPERIMENTS WITH THE PRIMITIVE

1971 EQUATIONS, Monthly Weather Review, 91, 99-164,

1972 10.1175/1520-0493(1963)091<0099:gcewtp>2.3.co;2, 1963.

1973 Song, Y., and Haidvogel, D.: A Semi-implicit Ocean Circulation Model Using a Generalized

1974 Topography-Following Coordinate System, Journal of Computational Physics, 115, 228-244,

1975 <https://doi.org/10.1006/jcph.1994.1189>, 1994.

1976 Ståhlberg, C., Bastviken, D., Svensson, B. H., and Rahm, L.: Mineralisation of organic matter in

1977 coastal sediments at different frequency and duration of resuspension, Estuarine, Coastal and Shelf

1978 Science, 70, 317-325, <https://doi.org/10.1016/j.ecss.2006.06.022>, 2006.

1979 Su, J.: Overview of the South China Sea circulation and its influence on the coastal physical

1980 oceanography outside the Pearl River Estuary, Continental Shelf Research, 24, 1745-1760,

1981 10.1016/j.csr.2004.06.005, 2004.

1982 Tolman, H., Accensi, M., Alves, J.-H., Ardhuin, F., Barbariol, F., Benetazzo, A., Bennis, A.-C., Bidlot,

1983 J., Booij, N., Boutin, G., Campbell, T., Chalikov, D., Chawla, A., Cheng, S., Collins Iii, C., Filipot,  
1984 J.-F., Foreman, M., Janssen, P., Leckler, F., and Westhuysen, A.: User manual and system  
1985 documentation of WAVEWATCH III (R) version 5.16, 2016.

1986 Turner, A., and Millward, G. E.: Suspended Particles: Their Role in Estuarine Biogeochemical Cycles,  
1987 Estuarine, Coastal and Shelf Science, 55, 857-883, 10.1006/ecss.2002.1033, 2002.

1988 van der Wegen, M., Dastgheib, A., Jaffe, B. E., and Roelvink, D.: Bed composition generation for  
1989 morphodynamic modeling: case study of San Pablo Bay in California, USA, Ocean Dynamics, 61,  
1990 173-186, 10.1007/s10236-010-0314-2, 2010.

1991 Walsh, J. P., and Nittrouer, C. A.: Understanding fine-grained river-sediment dispersal on continental  
1992 margins, Marine Geology, 263, 34-45, 10.1016/j.margeo.2009.03.016, 2009.

1993 Wang, S., Zhang, N., Chen, H., Li, L., and Yan, W.: The surface sediment types and their rare earth  
1994 element characteristics from the continental shelf of the northern south China sea, Continental  
1995 Shelf Research, 88, 185-202, 10.1016/j.csr.2014.08.005, 2014.

1996 Wang, S., Wu, S., Yan, W., Huang, W., Miao, L., Lu, J., Chen, Z., and Liu, F.: Rare metal elements in  
1997 surface sediment from five bays on the northeastern coast of the South China Sea, Environmental  
1998 Earth Sciences, 74, 4961-4971, 10.1007/s12665-015-4504-6, 2015.

1999 Wang, S., Li, J., Wu, S., Yan, W., Huang, W., Miao, L., and Chen, Z.: The distribution characteristics of  
2000 rare metal elements in surface sediments from four coastal bays on the northwestern South China  
2001 Sea, Estuarine, Coastal and Shelf Science, 169, 106-118, 10.1016/j.ecss.2015.12.001, 2016.

2002 Wang, Y., Wang, Y., Wan, X., Huang, C., Wang, R., Liu, X., Yi, J., and Zhang, Y.: Influence of the  
2003 Hanjiang River's Inlet Sediment Decrease on Modern Sedimentation in the Underwater Delta,  
2004 Applied Sciences, 13, 8039, 10.3390/app13148039, 2023.

- 2005 Warner, J. C., Sherwood, C. R., Arango, H. G., and Signell, R. P.: Performance of four turbulence  
2006 closure models implemented using a generic length scale method, *Ocean Modelling*, 8, 81-113,  
2007 10.1016/j.ocemod.2003.12.003, 2005.
- 2008 Warner, J. C., Sherwood, C. R., Signell, R. P., Harris, C. K., and Arango, H. G.: Development of a  
2009 three-dimensional, regional, coupled wave, current, and sediment-transport model, *Computers &*  
2010 *Geosciences*, 34, 1284-1306, 10.1016/j.cageo.2008.02.012, 2008.
- 2011 Warner, J. C., Armstrong, B., He, R., and Zambon, J. B.: Development of a Coupled  
2012 Ocean–Atmosphere–Wave–Sediment Transport (COAWST) Modeling System, *Ocean Modelling*,  
2013 35, 230-244, 10.1016/j.ocemod.2010.07.010, 2010.
- 2014 Warner, J. C., Schwab, W. C., List, J. H., Safak, I., Liste, M., and Baldwin, W.: Inner-shelf ocean  
2015 dynamics and seafloor morphologic changes during Hurricane Sandy, *Continental Shelf Research*,  
2016 138, 1-18, 10.1016/j.csr.2017.02.003, 2017.
- 2017 Weatherall, P., Marks, K. M., Jakobsson, M., Schmitt, T., Tani, S., Arndt, J. E., Rovere, M., Chayes, D.,  
2018 Ferrini, V., and Wigley, R.: A new digital bathymetric model of the world's oceans, *Earth and*  
2019 *Space Science*, 2, 331-345, <https://doi.org/10.1002/2015EA000107>, 2015.
- 2020 Wright, L. D., and Coleman, J. M.: Variations in Morphology of Major River Deltas as Functions of  
2021 Ocean Wave and River Discharge Regimes, *AAPG Bulletin*, 57, 370-398, 1973.
- 2022 Wright, L. D., and Nittrouer, C. A.: Dispersal of river sediments in coastal seas: Six contrasting cases,  
2023 *Estuaries*, 18, 494-508, 10.2307/1352367, 1995.
- 2024 Wu, C., Xing, W., Jie, R., Yun, B., Zhigang, H., Yiaping, L., Heyin, S., and Wenyan, Z.:  
2025 Morphodynamics of the rock-bound outlets of the Pearl River estuary, South China — A  
2026 preliminary study, *Journal of Marine Systems*, 82, S17-S27, 10.1016/j.jmarsys.2010.02.002, 2010.



2027 Wu, Z., Milliman, J. D., Zhao, D., Zhou, J., and Yao, C.: Recent geomorphic change in LingDing Bay,  
 2028 China, in response to economic and urban growth on the Pearl River Delta, Southern China,  
 2029 Global and Planetary Change, 123, 1-12, 10.1016/j.gloplacha.2014.10.009, 2014.

2030 Wu, Z., Milliman, J. D., Zhao, D., Cao, Z., Zhou, J., and Zhou, C.: Geomorphologic changes in the  
 2031 lower Pearl River Delta, 1850–2015, largely due to human activity, Geomorphology, 314, 42-54,  
 2032 10.1016/j.geomorph.2018.05.001, 2018.

2033 Wu, Z. Y., Saito, Y., Zhao, D. N., Zhou, J. Q., Cao, Z. Y., Li, S. J., Shang, J. H., and Liang, Y. Y.:  
 2034 Impact of human activities on subaqueous topographic change in Lingding Bay of the Pearl River  
 2035 estuary, China, during 1955-2013, Scientific Reports, 6, 37742, 10.1038/srep37742, 2016.

2036 Xia, X. M., Li, Y., Yang, H., Wu, C. Y., Sing, T. H., and Pong, H. K.: Observations on the size and  
 2037 settling velocity distributions of suspended sediment in the Pearl River Estuary, China,  
 2038 Continental Shelf Research, 24, 1809-1826, 10.1016/j.csr.2004.06.009, 2004.

2039 Xue, Z., He, R., Liu, J. P., and Warner, J. C.: Modeling transport and deposition of the Mekong River  
 2040 sediment, Continental Shelf Research, 37, 66-78, 10.1016/j.csr.2012.02.010, 2012.

2041 Yang, B., Liu, S.-M., and Zhang, G.-L.: Geochemical characteristics of phosphorus in surface  
 2042 sediments from the continental shelf region of the northern South China Sea, Marine Chemistry,  
 2043 198, 44-55, 10.1016/j.marchem.2017.11.001, 2018.

2044 Yang, J., Wu, D., and Lin, X.: On the dynamics of the South China Sea Warm Current, Journal of  
 2045 Geophysical Research: Oceans, 113, <https://doi.org/10.1029/2007JC004427>, 2008.

2046 Yang, Y., Guan, W., Deleersnijder, E., and He, Z.: Hydrodynamic and sediment transport modelling in  
 2047 the Pearl River Estuary and adjacent Chinese coastal zone during Typhoon Mangkhut, Continental  
 2048 Shelf Research, 233, 104645, 10.1016/j.csr.2022.104645, 2022.

2049 Young, I. R., Zieger, S., and Babanin, A. V.: Global trends in wind speed and wave height, *Science*, 332,  
2050 451-455, 10.1126/science.1197219, 2011.

2051 Zeng, X., He, R., Xue, Z., Wang, H., Wang, Y., Yao, Z., Guan, W., and Warrillow, J.: River-derived  
2052 sediment suspension and transport in the Bohai, Yellow, and East China Seas: A preliminary  
2053 modeling study, *Continental Shelf Research*, 111, 112-125,  
2054 <https://doi.org/10.1016/j.csr.2015.08.015>, 2015.

2055 Zhang, G., Cheng, W., Chen, L., Zhang, H., and Gong, W.: Transport of riverine sediment from  
2056 different outlets in the Pearl River Estuary during the wet season, *Marine Geology*, 415, 105957,  
2057 10.1016/j.margeo.2019.06.002, 2019.

2058 Zhang, G., Chen, Y., Cheng, W., Zhang, H., and Gong, W.: Wave Effects on Sediment Transport and  
2059 Entrapment in a Channel -Shoal Estuary: The  
2060 *Journal of Geophysical Research: Oceans*, 126, 10.1029/2020jc016905, 2021.

2061 Zhang, J., Jiang, Q., Jeng, D., Zhang, C., Chen, X., and Wang, L.: Experimental Study on Mechanism  
2062 of Wave-Induced Liquefaction of Sand-Clay Seabed, *Journal of Marine Science and Engineering*,  
2063 8, 66, 10.3390/jmse8020066, 2020.

2064 Zhang, W., Wei, X., Zheng, J., Zhu, Y., and Zhang, Y.: Estimating suspended sediment loads in the  
2065 Pearl River Delta region using sediment rating curves, *Continental Shelf Research*, 38, 35-46,  
2066 10.1016/j.csr.2012.02.017, 2012.

2067 Zhang, W., Zheng, J., Ji, X., Hoitink, A. J. F., van der Vegt, M., and Zhu, Y.: Surficial sediment  
2068 distribution and the associated net sediment transport pattern retain-->in the Pearl River Estuary,  
2069 South China, *Continental Shelf Research*, 61-62, 41-51, 10.1016/j.csr.2013.04.011, 2013.

2070 Zhong, Y., Chen, Z., Li, L., Liu, J., Li, G., Zheng, X., Wang, S., and Mo, A.: Bottom water

2071 hydrodynamic provinces and transport patterns of the northern South China Sea: Evidence from  
 2072 grain size of the terrigenous sediments, *Continental Shelf Research*, 140, 11-26,  
 2073 10.1016/j.csr.2017.01.023, 2017.

2074 Zong, X., Cheng, X., Zhang, S., Lian, Q., Deng, F., and Chen, Z.: Tidal effects on dynamics and  
 2075 freshwater transport of a medium-scale river plume with multiple outlets, *Ocean Modelling*, 188,  
 2076 102338, <https://doi.org/10.1016/j.ocemod.2024.102338>, 2024.

2077 Zong, Y., Huang, K., Switzer, A., yu, F., and Yim, W.: An evolutionary model for the Holocene  
 2078 formation of the Pearl River delta, China, *The Holocene*, 19, 129-142,  
 2079 10.1177/0959683608098957, 2009.

2080